Research and Development Technical Report

ECOM- 74-0104-F

EVALUATION OF $Nd:YVO_4$ AND $Ho:Er:Tm:YVO_4$ AS
PULSE PUMPED Q-SWITCHED LASERS

M. Bass
L. G. DeShazer
P. P. Yaney
Center for Laser Studies
University of Southern California
Los Angeles, California 90007

January 1976

Final Report for Period 1 January 1974 - 1 April, 1975

Prepared for

ECOM

US ARMY ELECTRONICS COMMAND FORT MONMOUTH, NEW JERSEY 07703

NOTICES

Disclaimers

Disposition

REPORT DOCUMENTATION PAGE		READ INSTRUCTIONS BEFORE COMPLETING FORM
1. REPORT NUMBER ECOM-74-0104-F	2. GOVT ACCESSION NO.	3. RECIPIENT'S CATALOG NUMBER
4. TITLE *(and Subtitle)* EVALUATION OF Nd:YVO4 AND Ho:Er:Tm:YVO4 AS PULSE PUMPED Q-SWITCHED LASERS		5. TYPE OF REPORT & PERIOD COVERED Final Report 1 Jan 74 - 1 Apr 75
		6. PERFORMING ORG. REPORT NUMBER
7. AUTHOR(s) Michael Bass, Larry G. DeShazer, and Perry P. Yaney		8. CONTRACT OR GRANT NUMBER(s) DAAB07-74-C-0104
9. PERFORMING ORGANIZATION NAME AND ADDRESS Center for Laser Studies University of Southern California Los Angeles, CA 90007		10. PROGRAM ELEMENT, PROJECT, TASK AREA & WORK UNIT NUMBERS 1S7 62703 A186 06
11. CONTROLLING OFFICE NAME AND ADDRESS US Army Electronics Command ATTN: AMSEL-CT-L-D		12. REPORT DATE January 1976
		13. NUMBER OF PAGES
14. MONITORING AGENCY NAME & ADDRESS(*If different from Controlling Office*)		15. SECURITY CLASS. *(of this report)* Unclassified
		15a. DECLASSIFICATION/DOWNGRADING SCHEDULE

16. DISTRIBUTION STATEMENT *(of this Report)*

Approved for Public Release; Distribution of this document is Unlimited.

17. DISTRIBUTION STATEMENT *(of the abstract entered in Block 20, if different from Report)*

18. SUPPLEMENTARY NOTES

None

19. KEY WORDS *(Continue on reverse side if necessary and identify by block number)*

Yttrium orthovanadate (YVO4); Lasers; Neodymium (Nd); Holmium (Ho), Erbium (Er), Thulium (Tm); Absorption, Emission Spectra; Energy Levels, Stimulated Emission Cross Sections; Inclusions, Irridium; Crystal Growth

20. ABSTRACT *(Continue on reverse side if necessary and identify by block number)*

This program was designed to develop and exploit rare-earth doped yttrium orthovanadate (YVO_4) as a high efficiency laser material. The effort included crystal growth, spectroscopy and laser performance testing. Though emphasis was placed on the spectroscopic and laser properties of Nd^{3+} ions, the spectroscopy of Ho^{3+} ions with Er^{3+} and Tm^{3+} co-dopants was also studied. Measurements of the optical absorption and emission spectra, energy levels and stimulated emission cross-sections are reported

DD FORM 1473 EDITION OF 1 NOV 65 IS OBSOLETE
1 JAN 73
S/N 0102-014-6601

20. (Continued)

Details in the spectroscopy of Nd^{3+} in YVO_4 were measured and analyzed. The Cary 17 Spectrophotometer was used to measure the absorption spectrum of Nd^{3+}:YVO_4 from 0.38 to 2.0 μm. The most intense absorption line in the 0.81 μm absorption group, the group most appropriate for diode pumping, was the line at 0.8080 μm with $\alpha = 9$ cm^{-1}. The $^4F_{3/2} \rightarrow {}^4I_{9/2}$ spectrum is still somewhat of a puzzle. There seems to be more than one set of spectra for Nd^{3+} in YVO_4 suggestive of either a second site for the Nd^{3+} ions or else that there is significant Nd-Nd pair spectra present.

Laser emission in Ho^{3+} doped materials was analyzed theoretically. The oscillator strengths, transition rates and branching ratios associated with known and potential laser transitions in Ho^{3+} were calculated using a computer.

Since no Nd:YVO_4 laser rods suitable for testing were delivered by the subcontractor during the second part of this program no new laser testing was conducted. Several Ho, Er, Tm:YVO_4 laser rods were delivered but were not tested because our emphasis was concentrated on the Nd problem. Nevertheless, in the first six months of this program it was demonstrated that Nd:YVO_4 could outperform Nd:YAG in pulse pumped Q-switched operation. In addition, reliable, pre-pulse free, single pulse Q switching of Nd:YVO_4 was demonstrated with no intracavity polarizer.

SUMMARY

Yttrium orthovanadate (YVO_4) doped with rare earth ions was investigated for use as a pulse pumped Q switched laser material. The spectroscopy of two potential laser ions, Nd^{3+} and Ho^{3+}, was studied in detail. Measurements of the optical absorption and emission spectra, energy levels and stimulated emission cross-sections are reported. Q switched lasing of pulse pumped $Nd:YVO_4$ was demonstrated and found to be superior in output to that of Nd:YAG in the same pump cavity. The pump cavity was a small gold plated single ellipse and was designed for optimum Nd:YAG performance. In addition, the strong inherent birefringence of $Nd:YVO_4$ made possible pre-pulse free, single pulse Q switching with no-intracavity polarizer.

The crystal growth and materials evaluation effort of this program demonstrated that large boules (1.3 x 7 cm) of material grown along the crystalographic A axis could be prepared without visible color centers. It was found however that inclusions of irridium from the crucible were often present and were the cause of significant losses in several crystals. These inclusions are often present along the a-plane which is a cleavage plane of YVO_4. Their presence weakens the bonding and cleavage frequently occurs during the cool-down. This is a major and as yet unresolved problem. If cool-down was achieved without severe cleavage, the stresses of sawing, grinding and polishing often caused material failure during rod fabrication.

It is the conclusion of this project that when the growth and fabrication problems of $Nd:YVO_4$ are solved, this material will be a suitable replacement for Nd:YAG in laser systems where input power is limited.

PREFACE

This is the final report on the "Evaluation of Nd:YVO$_4$ and Ho, Er, Tm:YVO$_4$ as Pulse Pumped Q-Switched Lasers". The research was performed under U.S. Army Electronics Command Contract No. DAAB07-74-C-0104. The program monitor was Mr. John W. Strozyk, Fort Monmouth, New Jersey. The research covers the period 2 January 1974 to 30 March 1975 with the results of the work performed during the period from 2 January 1974 to 30 June 1974 reported in the first semiannual report of this program (Report # ECOM-74-0104-1) and the work performed during the period from 1 July 1974 to 30 March 1975 described herein.

The principal investigators during this project were Michael Bass, Associate Director of the Center for Laser Studies, Uri Ranon, Senior Research Scientist at the Center, and, following Dr. Ranon's leaving the Center, Dr. Larry G. DeShazer, Director of the Center, was substituted as co-principal investigator.

The following personnel participated in various phases of the study:

Laser Testing	M. Bass, U. Ranon
Spectroscopy, Nd	L.G. DeShazer, M. Bass, J.K. Guha, P.P. Yaney, K.M. Leung
Spectroscopy, Ho	E.D. Reed and U. Ranon
Spectroscopic Analysis	L.G. DeShazer, P.P. Yaney, J.A. Caird
Color Centers	J.K. Guha

Mr. L.R.Rothrock, R.E. Wilder and Dr. D. Brandle of the Crystal Products Department, Union Carbide Corporation, San Diego, California, supplied the spectroscopic samples and laser rods used in this program. They prepared the portion of this report concerning crystal growth and laser rod fabrication. Dr. A.B. Chase of the Aerospace Corporation, El Segundo, California, conducted an evaluation of material quality and the results of that work are also described in this report.

iv

During this report period, a paper describing some of the work sponsored by this contract was published. This paper was by J. A. Caird and L. G. DeShazer, "Analysis of Laser Emission in Ho^{3+}-Doped Materials," IEEE J. of Quantum Electronics QE-11, 97 (1975). Also, several meetings were held to discuss the status of the work:

8 Oct. 1974   M. Bass. L. R Rothrock, and D. Brandle visited J. Strozyk and E. Schiel at Fort Monmouth, NJ.

16 Jan. 1975   L.G. DeShazer visited A.B. Chase at Aerospace Corporation.

30 Jan. 1975   L. G. DeShazer visited J. Strozyk and E. Schiel at Fort Monmouth, NJ.

14 Feb. 1975   L.G. DeShazer visited L. R Rothrock at UCC.

TABLE OF CONTENTS

LIST OF ILLUSTRATIONS

LIST OF TABLES

I. INTRODUCTION

The object of this program is to investigate rare earth doped yttrium orthovanadate (YVO_4) for use as a low threshold, pulse pumped, Q-switched laser material. Detailed studies of $Nd:YVO_4$ laser material were made. This included spectroscopic measurements of interest for predicting and evaluating laser performance and demonstration of long pulse and pulse pumped, Q-switched operation. Because of the concentration on $Nd:YVO_4$ only spectroscopic measurements were made for the Ho, Er, $Tm:YVO_4$ laser material.

YVO_4 was proposed as a laser host crystal many years ago [1,2] but was dropped because of early crystal growth difficulties. Recent advances in the growth of this crystal [3] however show that these difficulties are not insurmountable. As part of this program large A axis boules (1.3 x 7 cm) and 3 x 30 mm $Nd:YVO_4$ laser rods have been prepared. These have been free of color centers and have had excellent optical quality. A laser rod fabrication problem was encountered causing the loss of several potential laser rods. However, with improved material (i.e., material free of included irridium) the fabrication problem should be correctable.

Table 1 summarizes the pertinent data for Nd in YVO_4. Included in Table 1 are data for Nd in YAG, GGG and $YAlO_3$. The peak cross section for the laser transition at 1.06 μm of Nd in YVO_4 is 30 x 10^{-19} cm^2 as compared to 6.5 x 10^{-19} cm^2 in YAG. The fluorescent lifetime for the upper laser level ($^4F_{3/2}$) in YVO_4 is accordingly smaller than in YAG, 92 μsec as compared to 240 μsec. In a small elliptical laser cavity, the threshold for long pulse operation of $Nd:YVO_4$ is less than half that for Nd:YAG. The table also includes the crystal growth rate (~ 3x higher for $Nd:YVO_4$ than Nd:YAG) and segregation coefficient (~ 2x larger in $Nd:YVO_4$ than in Nd:YAG).

Specifically, it is to be noted that this report summarizes a 15 month study of the laser properties and spectroscopy of $Nd:YVO_4$ and of the spectroscopy of Ho, Er, $Tm:YVO_4$. The materials preparation and quality evaluation

1

efforts are described in Section II. Spectroscopic measurements and their interpretation are discussed in Section III. Section IV presents a survey of the Nd:YVO$_4$ absorptions. The laser testing, while described in detail in the semiannual report, is discussed and Pockels cell Q switching of Nd:YVO$_4$ with no intracavity polarizer is analyzed in Section V. In Section VI, the major conclusions of this program are summarized and recommendations for further work are given. In Appendix A we present a discussion of laser emission in Ho^{3+} doped materials. In addition, for completeness we have included in Appendix B a description of work done at The Aerospace Corporation concerning argon laser pumped CW lasing of Nd:YVO$_4$ at 1.06 and 1.34 μm.

Table 1. Comparison of Neodymium Laser Hosts

	YVO$_4$:Nd A-axis	YAG:Nd	GGG:Nd	YAlO$_3$:Nd B-axis
λ, μm	1.0640	1.0642	1.0622	1.0645 1.0725 1.0795
τ, μs	92	240	255	175
$\Delta\nu$, cm^{-1}	7	6	6	10
σ, cm^2	30×10^{-19}	6.5×10^{-19}	3.4×10^{-19}	2.2×10^{-19} 3.9×10 " 4.4×10 "
Threshold, J	0.5	1.1	---	---
Polarization	π	No	No	partial
Crystal growth	core-free	core	core-free	core, twins, inclusions
Growth rate, in./hr.	0.06	0.020	0.090	0.060
Segregation coefficient	≈ 0.3	≈ 0.18	≈ 0.6	---
Comments	High gain, low threshold	Standard	λ matches glass, optical quality, size	Low gain, C-axis High gain, B-axis

II. MATERIALS GROWTH AND PREPARATION

A. Growth of YVO$_4$ Crystals at Union Carbide Corp.

1. Background

The growth of YVO$_4$ single crystals began at Union Carbide Crystals

Products in 1965 and small pure and doped crystals were grown by the

Czochralski process [4, 5]. The crystals were grown on a flame-heated

growth station from an iridium crucible. These crystals were supplied to

various laboratories including RCA and Bell Telephone Laboratory. More

recent work was funded by the U.S. Army Electronics Command at Ft.

Monmouth under Contract DAAB0772-C-0022. [3] This work included Bridgman

and Czochralski growth and was aimed at undoped YVO$_4$ for polarizing prisms.

The technique settled on was RF induction heated Czochralski and boules of

1/2" dia. x 4" long were eventually produced. High optical quality polarizing

prisms were cut from the material. Following this work, some in-house

effort was put forth to grow some YVO$_4$ crystals doped with Nd and with Er,

Tm, and H$_o$. These crystals were, in general, small and the work was con-

cerned with growth habits, inclusions and melt composition.

The work of this report was begun under sub-contract to the University

of Southern California and was directed toward supplying 3 x 30 mm laser rods

and spectrographic samples of rare earth doped YVO$_4$, ErVO$_4$ and TmVO$_4$.

2. Melt Effects

The phase diagram for Y$_2$O$_3$-V$_2$O$_5$ (Figure 1) shows that YVO$_4$ melts

congruently at 1810°C. It appears, however, that the melt is not stable under

normal furnace atmosphere conditions and that oxygen is lost from the melt.

At the growth temperature, the melt is very turbulent and complex dark con-

vection lines are observed. As the temperature is lowered, the melt forms

a crust of solid material on the surface. This crust can be removed by using

4
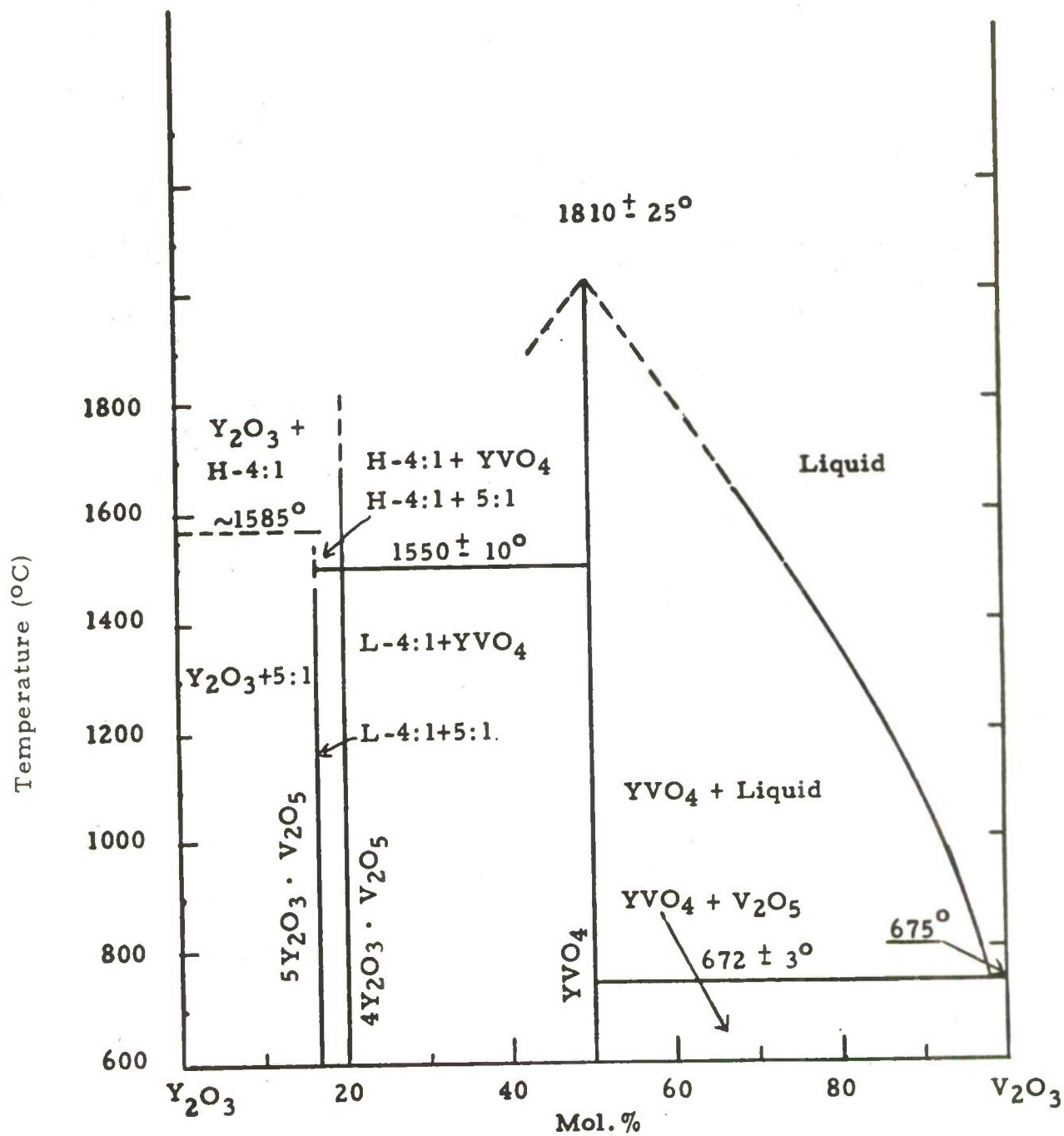
Figure 1. Phase Diagram-System Y_2O_3-V_2O_5. After E. M. Levin, J. Am. Cer. Soc. 50 [7] 381 (1967).

argon or nitrogen flow in the growth system. Liquid V_2O_5 slightly above the melting point dissociates according to

$$V_2O_5 \rightarrow V_2)_{5-x} + \frac{x}{2} O_2 \ .$$
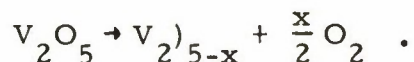
Where more and more suboxides appear with increasing temperature. It is believed that YVO_4 behaves in a similar manner. That is

$$YVO_4 \rightarrow YVO_{4-x} + \frac{x}{2} O_2 \ .$$

It has been shown that the concentration of V^{4+} can be controlled for certain practical oxygen partial pressures and that Czochralski growth can be effected from the solution. While control of crystal diameter and atmosphere is critical and difficult, high quality boules have on occasion been produced.

Invariably, melts which have been solidified after growth are dark indicating a reduced state and appear to have many phases present. Figure 2 shows remainders of melts from various growths.

3. Growth

During this research a total of 50 crystal-growth runs were made. Growth was performed in a standard Czochralski growth station using a 2" x 2" iridium crucible. Pull rates were as high as 3 mm/hr with 1.5mm/hr settled on as it appears that inclusions are reduced. Various starting materials were used and availability is sometimes a problem. A list of available materials is given in Table 2.

Initial growth runs on a new material were made with lower purity materials while runs for yield were made with high purity ones. No effect on crystal growth was seen as a result of purity. For production of samples and laser rods the preferred material is General Electric's YVO_4 powder of 99.99% purity.
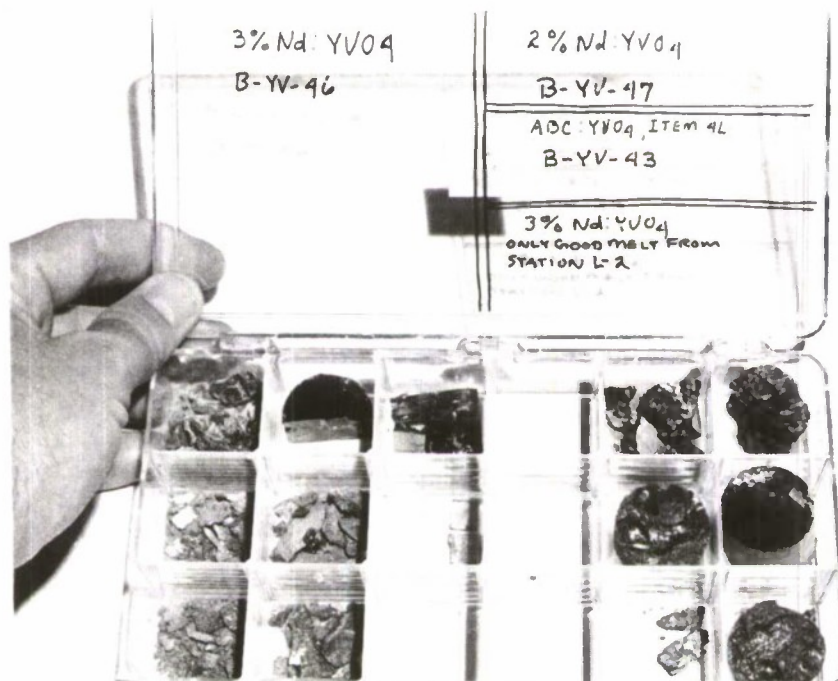
Figure 2. Remnants of YVO_4 Melts.

Table 2. Starting Materials Available for Crystal Growth

Material	Purity	Suppliers	Price
YVO_4	99.99%	General Electrics	\$101.60/lb
Tm_2O_3	99.99%	Research Chemicals	4.00/gm
Tm_2O_3	99.9 %	Research Chemicals	2.75/gm
Er_2O_3	99.999%	Research Chemicals	200.00/lb
Er_2O_3	99.9 %	Research Chemicals	45.00/lb
Ho_2O_3	99.9 %	Research Chemicals	0.35/gm
V_2O_3	99.99 %	Research Chemicals	14.50/lb

Growth was begun with stoichiometric melts at 60 standard cubic feet per hour, scf/h, n_2 flow with 1% O_2 atmosphere. A rotation rate of 28 rpm and a pull rate of 1.5 mm/hr were established. A seed of a-axis orientation was used for most growths. Several growths were made off axis due to an error in seed orientation. The Laue photographs used for orienting the seeds for a-axis were actually (110). Laue patterns for each one are shown in Figure 3.

The crystals exhibit a marked habit when grown along the a-axis. As shown in Figure 4, the boule cross-section is flattened with faceting on (100) and the long edge parallel to (001). The aspect ratio of the flattening can be affected by pull rate. C-axis material, on the other hand, grows with a nearly square cross-section.

Diameter control is very sensitive and difficult and frequent cross-section steps were encountered. Figure 5 shows several of the shapes observed. Some improvement in this condition was made by tuning control equipment as closely as possible during the contact. As these changes occur, the growth rate at the interface changes and inclusions of bubbles, second phase material and occasionally iridium are observed to form on the interface.
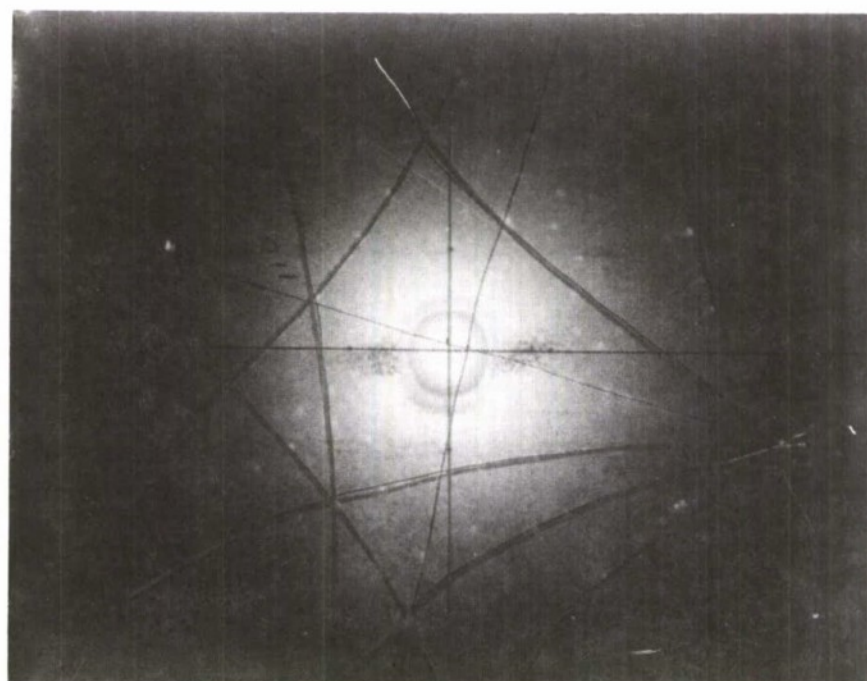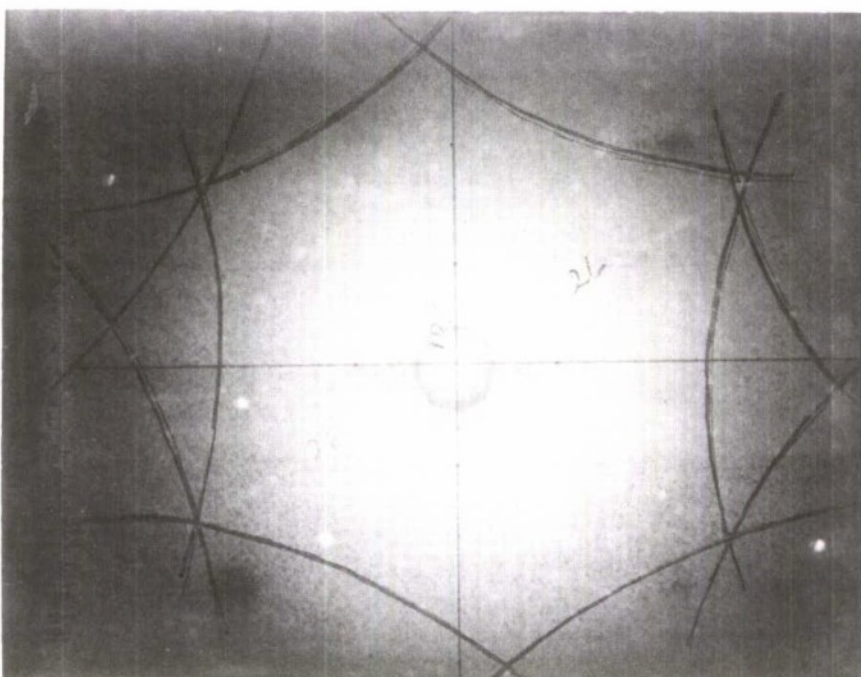
Figure 3. Laue patterns for (100) and (110) YVO$_4$.

9
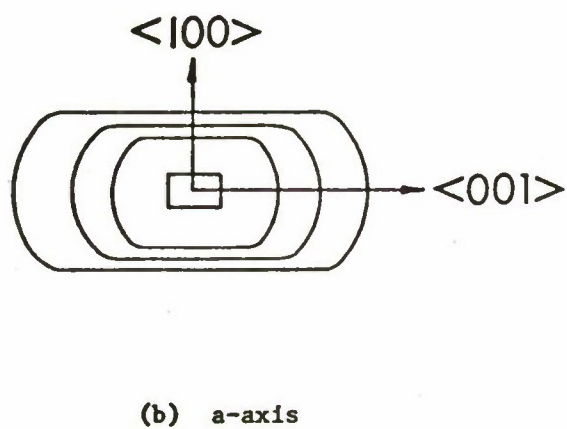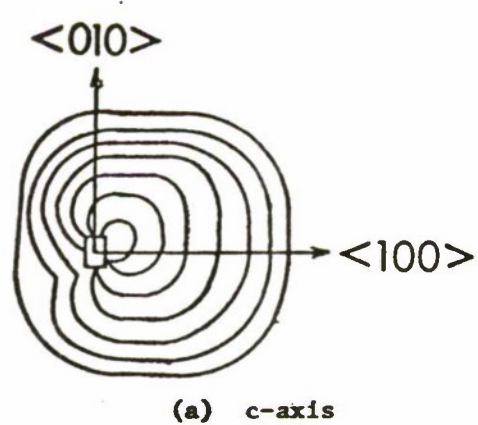
Figure 4. Cross-section Habits of C-axis and A-axis YVO$_4$.

10
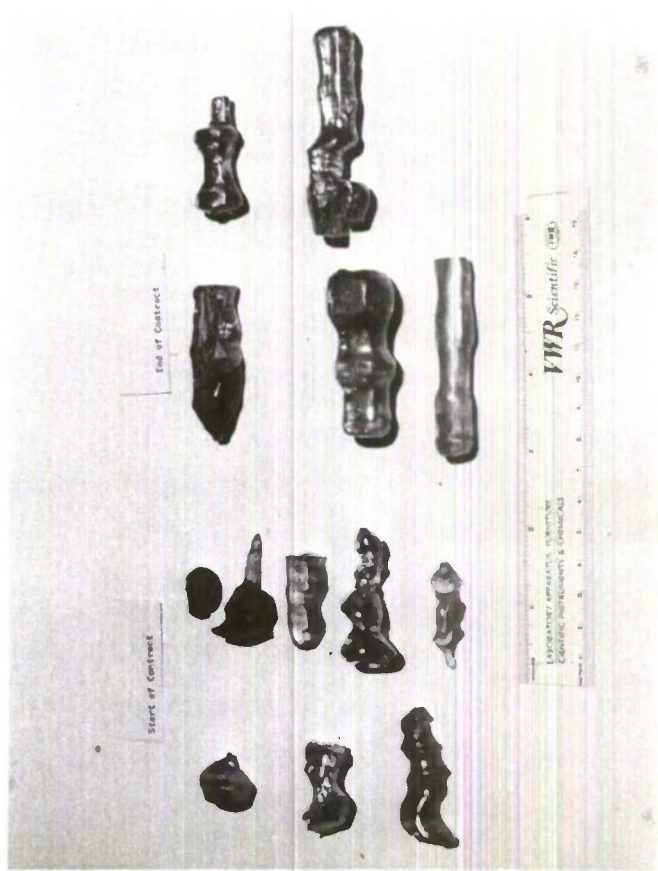
Figure 5. Some Boules Grown During Contract.

Since the interface is nearly flat in YVO_4, this means that inclusions occur nearly along the a-plane. The a-plane is a strong cleavage plane, but has sufficient strength to withstand normal fabrication stresses. However, when inclusions are present on the interface the bonding is weakened remarkably and cleavage frequently occurs in cool-down or in fabrication. This is a major problem which must be solved.

Grown boules are in a reduced state and are dark in color. Subsequent annealing in oxygen at 1400°C for 24 hours serves to return them to transparency. No color changes were observed in the boules in normal storage and handling.

Crystals grown were:

Material	Growth Runs	Yield of 4cm Boules
$Nd:YVO_4$	26	5
"ABC":YVO_4	21	13
$ErVO_4$	2	1
$Tm:YVO_4$	1	0

A list of actual compositions appears in Table 3.

4. Fabrication

YVO_4 has a hardness of 480 KHN which is the range of many glasses and as such polishes, saws, and grinds well. The major problem is that of cleavage along the a-plane. It is felt that the problem may be due largely to the presence of growth imperfections on the interface (a-plane) as already discussed. Credence is given this hypothesis by the fact that laser rods do not cleave into an infinite number of platelets. When a rod does cleave, it usually withstands all subsequent grinding and processes without further cleaving.

Because of high losses in grinding laser rod cylinders, core drilling was investigated. Although core drilling provides a more gentle technique, losses continued at the same rate. The problems in fabrication are

12

Table 3. List of Boules Grown

Boule #	Composition	Boule Size	Quality	Usable Length	Final FAB Yield
B-YV-1	YVO$_4$	None	------	------	------
-2	"	"			
-3	"	"			
-4	1% NdYVO$_4$	2 cm	Good, No Cracks or Bubbles	1 cm	2 ea 5 mm x 5 mm Cubes
-5	"	2 cm	Good	None	1 ea 5 mm x 5 mm Cube (Shipped)
-6	"	1.5 cm	Poor	None	
-7	"	None			
-8	"	"			
-9	"	4 cm	Cracked Throughout	None	None
-10	"	4 cm	"		
-11	"	3 cm	Heavy Bubbles	2 cm	
-12	"	1.5 cm	Poor	None	
-13	"	1.5 cm		"	
-14	"	2.5 cm	Poor, Heavy Bubbles	"	
-15	"	3.5 cm	Poor, Heavy Bubbles, Cracked	"	
-16	"	None			
-17	$(Y_{0.42}Er_{0.50}Tm_{0.07}Ho_{0.01})VO_4$	2.2 cm	Poor	"	
-18	1% NdYVO$_4$	4.3 cm		3.5 cm	1 ea 3 mm x 30 mm Laser Rod
-19	"	3.6 cm	Many Micro Bubbles	3 cm	1 ea 3 mm x 30 mm Laser Rod
-20	"	None			
-21	"	6.2 cm	Poor, Corkscrew, Cracked	1 cm	Made Seeds
-22	"	4.0 cm	Many Micro Bubbles	3 cm	1 ea 3 mm x 30 mm Laser Rod
-23	$(Y_{0.42}Er_{0.50}Tm_{0.07}Ho_{0.01})VO_4$	5.0 cm	Corkscrewed and Cracked	None	
-24	"	4.5 cm	Lots of Inclusions		
-25	"	6.0 cm	Lots of Inclusions	2 cm	1 ea 3 mm x 20 mm Laser Rod
-26	"	5.5 cm	Lots of Inclusions	2.7 cm	2 ea 3 mm x 27 mm Laser Rod
-27	"	5.5 cm	Corkscrewed	None	
-28	$(Er_{0.42}Tm_{0.07}Ho_{0.01})VO_4$	None			
-29	$(Y_{0.17}Er_{0.73}Tm_{0.07}Ho_{0.01})VO_4$	7.5 cm	Cracked Throughout	None	
-30	$(Y_{0.17}Er_{0.75}Tm_{0.07}Ho_{0.01})VO_4$	6 cm	Inclusions, Cracked	3 cm	3 mm x 30 mm Laser Rod, 3 mm x 13 mm cylinder
-31	$(Y_{0.67}Er_{0.25}Tm_{0.07}Ho_{0.01})VO_4$	8 cm	Inclusions, Cracked	3 cm	Spec Sample
-32	$(Y_{0.42}Er_{0.50}Tm_{0.07}Ho_{0.01})VO_4$	None			
-33	"	5 cm	Inclusions, Cracked	3 cm	3 mm x 26 mm Laser Rod, 3 mm x 20 mm cylinder

13

Table 3. List of Boules Grown (continued)

Boule #	Composition	Boule Size	Quality	Usable Length	Final FAB Yield
B-YV-34	$(Y_{0.42}Er_{0.50}Tm_{0.07}Ho_{0.01})VO_4$	None			
-35	"	"			
-36	"	4 cm	Cracked Throughout	None	
-37	$(Er_{0.92}Tm_{0.07}Ho_{0.01})VO_4$	9 cm	Cracked	3 cm	3 mm x 25 mm Cylinder
-38	"	None			
-39	"	None			
-40	$(Y_{0.17}Er_{0.75}Tm_{0.07}Ho_{0.01})VO_4$	4.5 cm	Polycrystalline, Cracked	None	
-41	1.5% $NdYVO_4$	None			
-42	3% $NdYVO_4$	5.5 cm	Cracked	None	
-43	$(Y_{0.42}Er_{0.50}Tm_{0.07}Ho_{0.01})VO_4$	6 cm	Cracked	3 mm	5 mm x 12 mm Cylinder
-44	"	None			
-45	"	None			
-46	3% $NdYVO_4$	7 cm	Good, No cracks	3 cm	3 mm x 10 mm Cylinders
-47	2% $NdYVO_4$	4.4 cm		3 cm	5 mm x 10 mm Cylinder
-48	1% $TmYVO_4$	.5 cm		.5 cm	Spec Sample
-49	.5% $NdYVO_4$	None			
-50	"	None			

illustrated by the fact that crystals were submitted for thirteen 3 x 30 mm laser rods and ten 3 x 20-30 mm while no rods were fabricated without breakage and at least some loss of lengths.

5. Analysis

A cleaved sample of $(Y_{0.17}Er_{0.75}Tm_{0.07}Ho_{0.01})VO_4$ was sent to Seal Laboratories for analysis with particular attention to inclusions. Analysis was done using scanning electron microprobe and electron microprobe. Energy dispersive x-ray analysis (DXA) was used for the electron microprobe. This technique is useful from the surface to a depth of one micron.

A general area of the surface of the crystal, Figure 6, shows an included particle (A), the general crystal matrix (B), and several loose contaminant particles. EDXA was performed on the particle at A, Figure 7 and indicated the presence of major amounts of vanadium and erbium, a minor amount of yttrium, and traces of thulium and silicon. The EDXA of the matrix (B) indicated the presence of the same composition, except that no silicon was present, Figure 8.

Included particles along a cleavage step is shown in Figure 9. EDXA of the particle at "C" showed major amounts of erbium, vanadium and calcium, minor amounts of silicon, yttrium and potassium and trace amounts of sulfur, chlorine, and thulium (Figure 10). The EDXA of the adjacent matrix (Figure 11) showed the same composition as the previous matrix.

A large inclusion, Figure 12, was also EDXA, the inclusion contained major amounts of vanadium, erbium, silicon, chlorine, sulfur, potassium and calcium, a minor amount of yttrium, and a trace of thulium (Figure 13).

Samples of the pure powders used to make the crystals were also analyzed using EDXA (Figures 14-16). Using the peak heights and calculating the number of X-ray peak counts per atom percent, the atom ratios of the vanadate crystal were calculated: V:Er (plus Ho and Tm):Y were 2.6:2.7:0.13.

15

Figure 6. Included Particle (A) and General Crystal
Matrix in $(Y_{0.17}Er_{0.75}Tm_{0.07}Ho_{0.01})VO_4$.

16
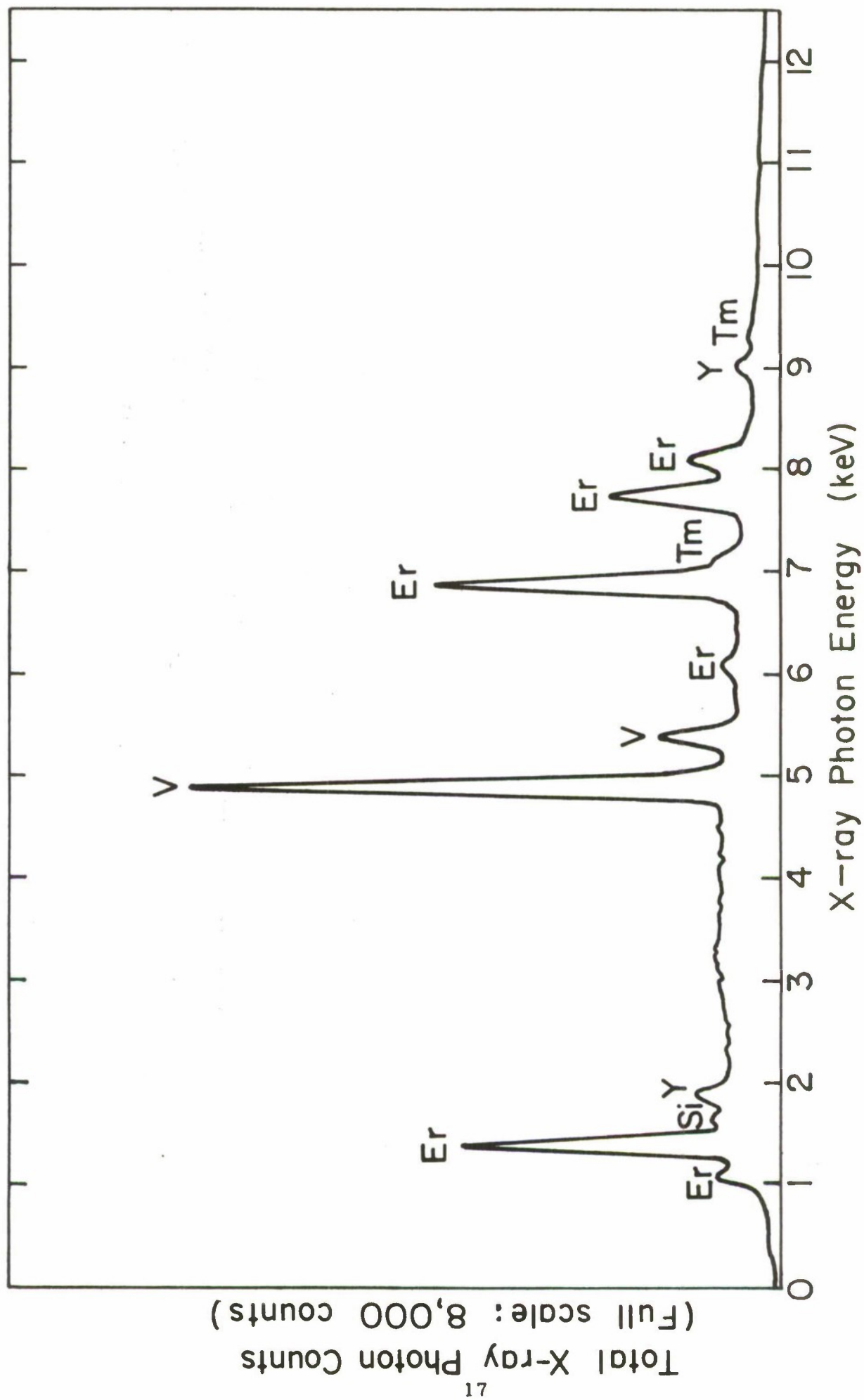
Figure 7. E.D.X.A. of area "A" in Figure 6.

17
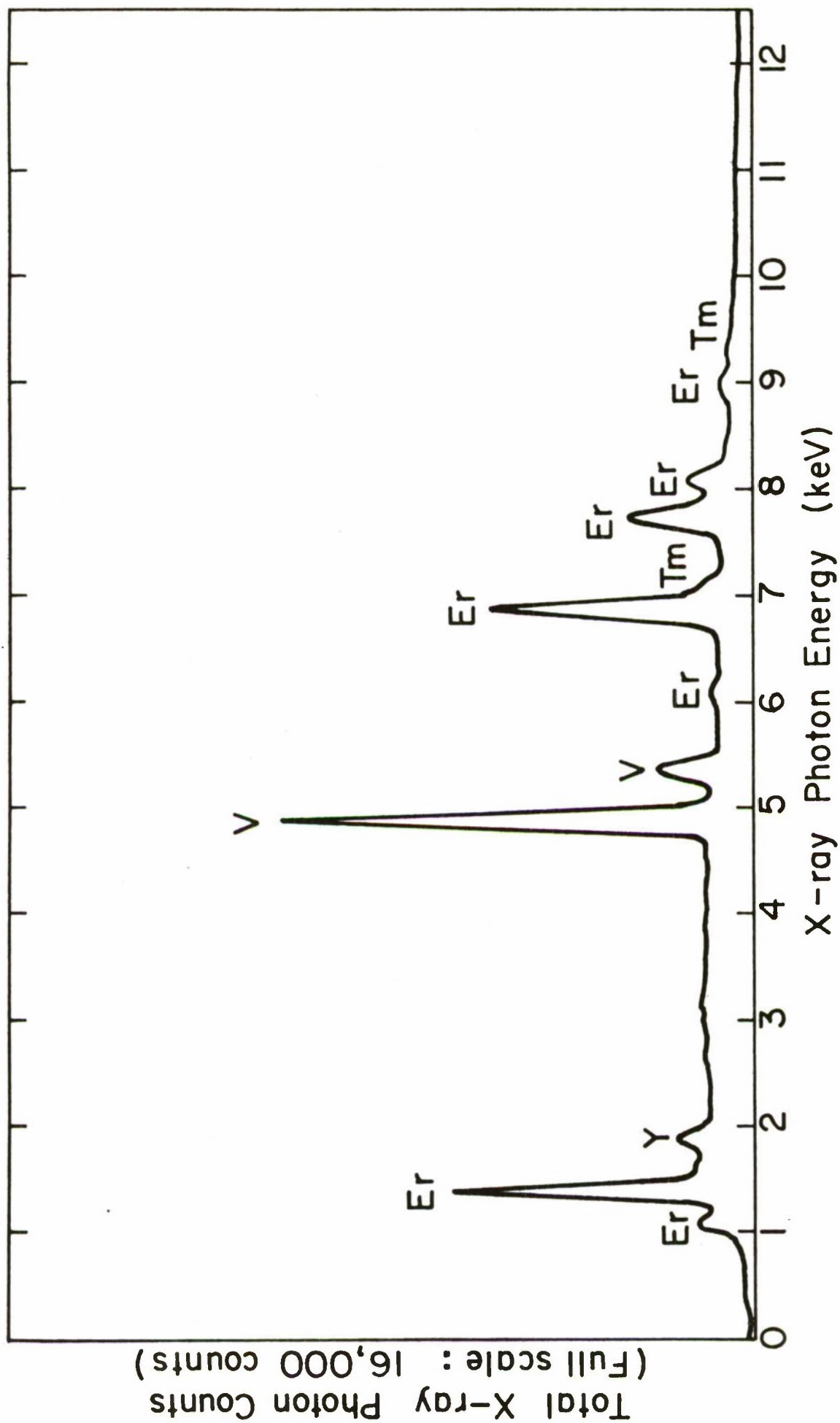
Figure 8.   E.D.X.A. of area "B" in Figure 6.

Figure 9.   Included Particles Along a Cleavage
            Step in $(Y_{0.17}Er_{0.75}Tm_{0.07}Ho_{0.01})VO_4$

19
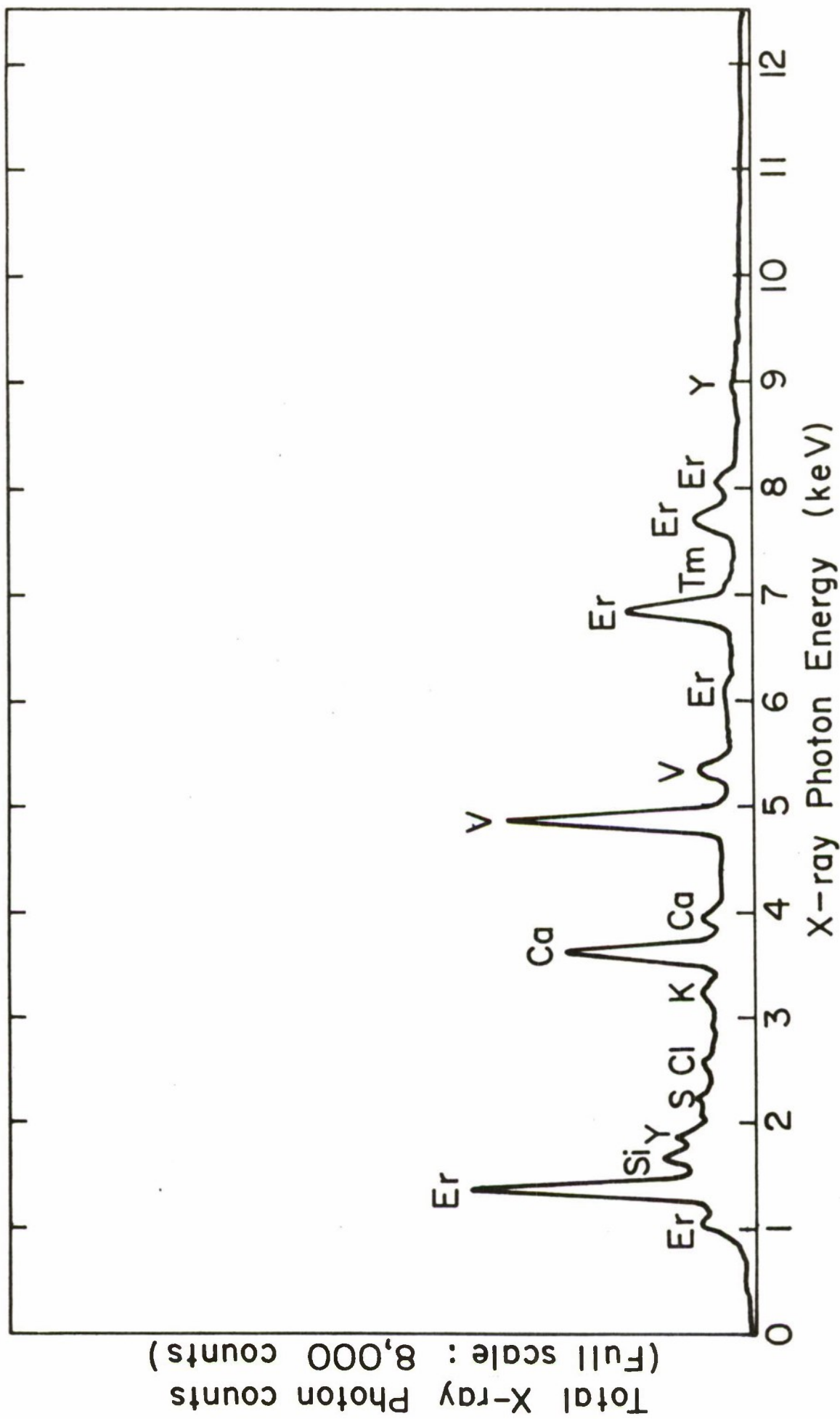
Figure 10. E.D.X.A. of area "C" in Figure 9.
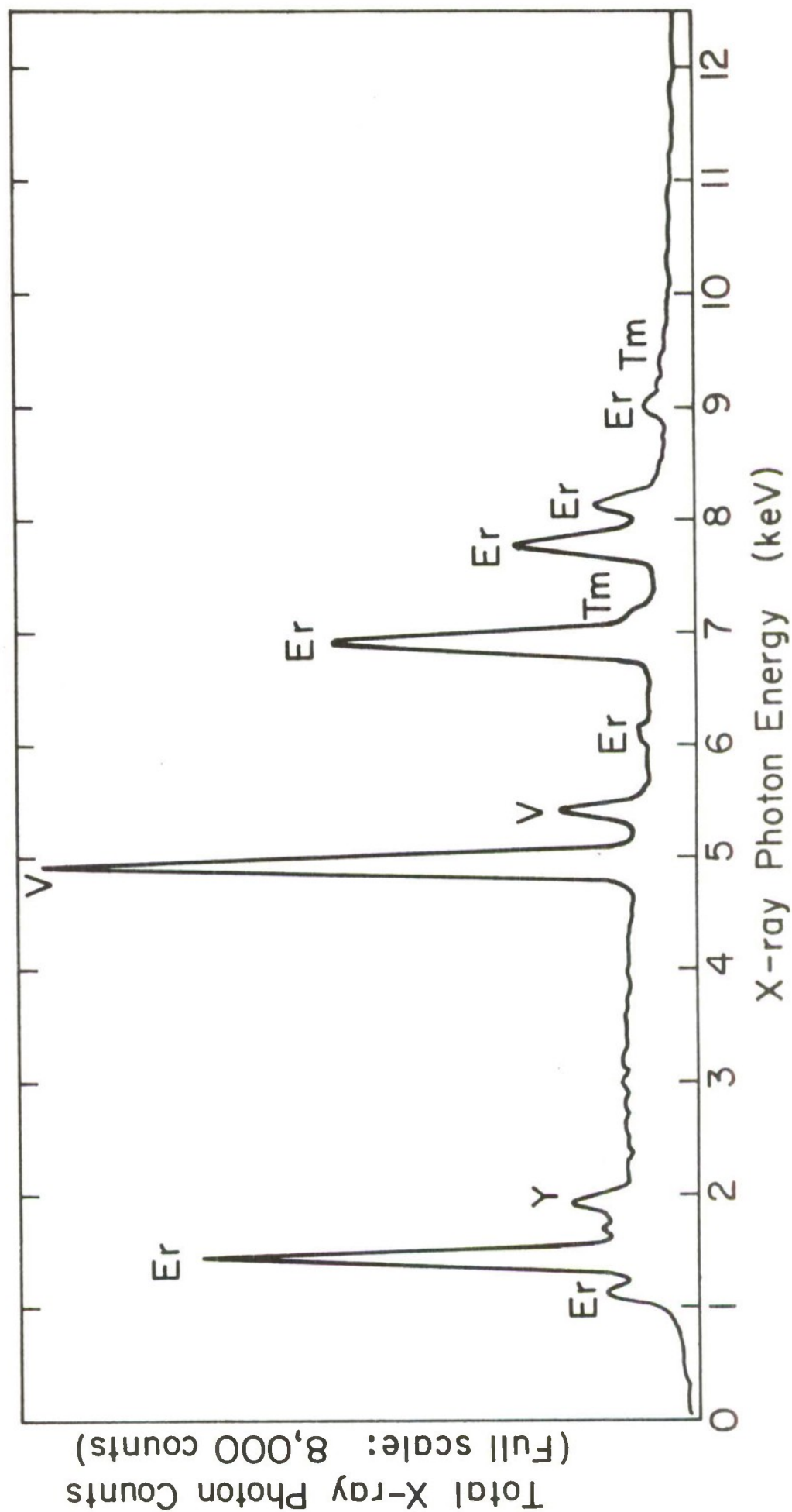
Figure 11. E.D.X.A. of area "D" in Figure 9.

21

Figure 12.   A Large Inclusion in $(Y_{0.17}Er_{0.75}Tm_{0.07}Ho_{0.01})VO_4$.
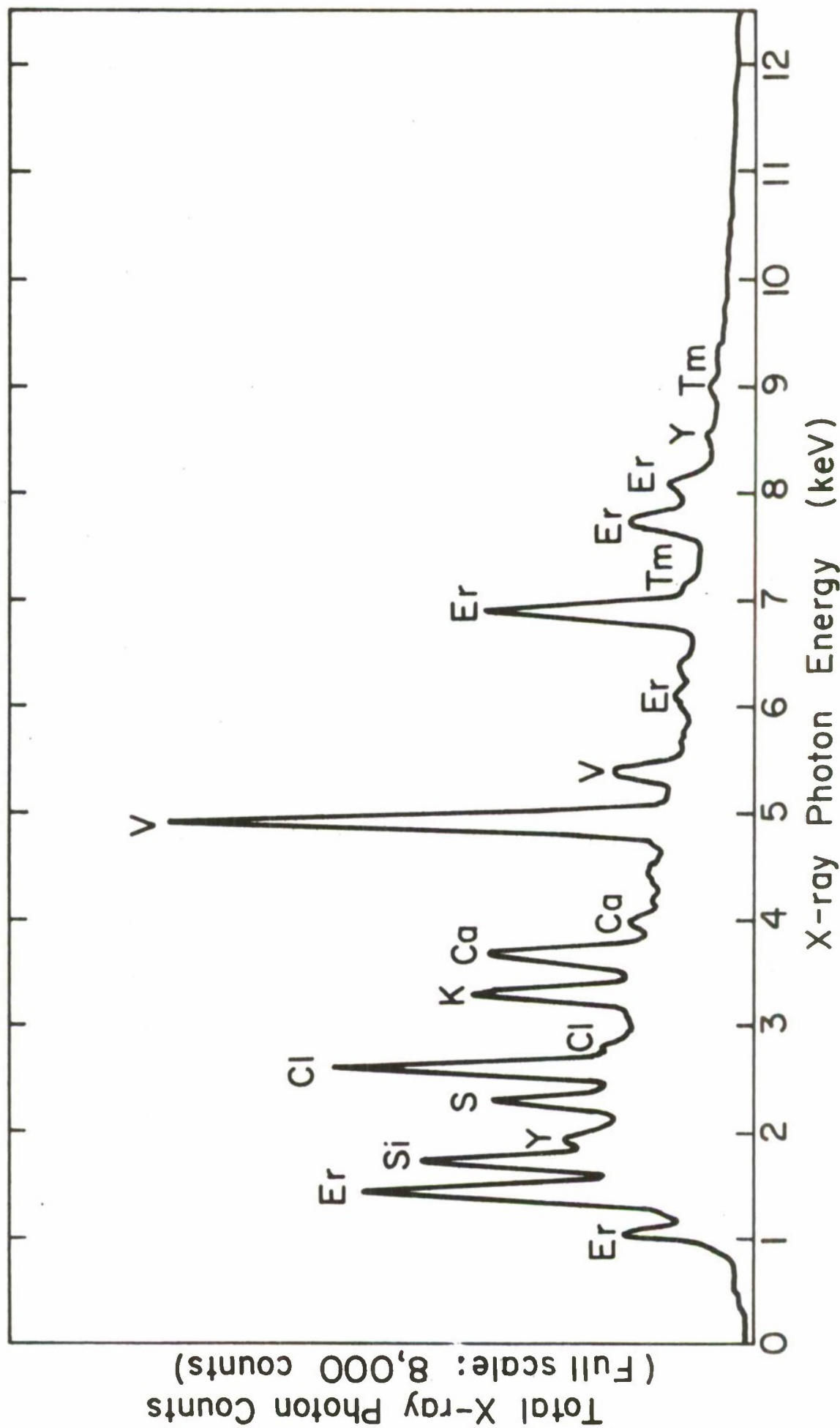
Figure 13. E.D.X.A. of area "E" in Figure 12.
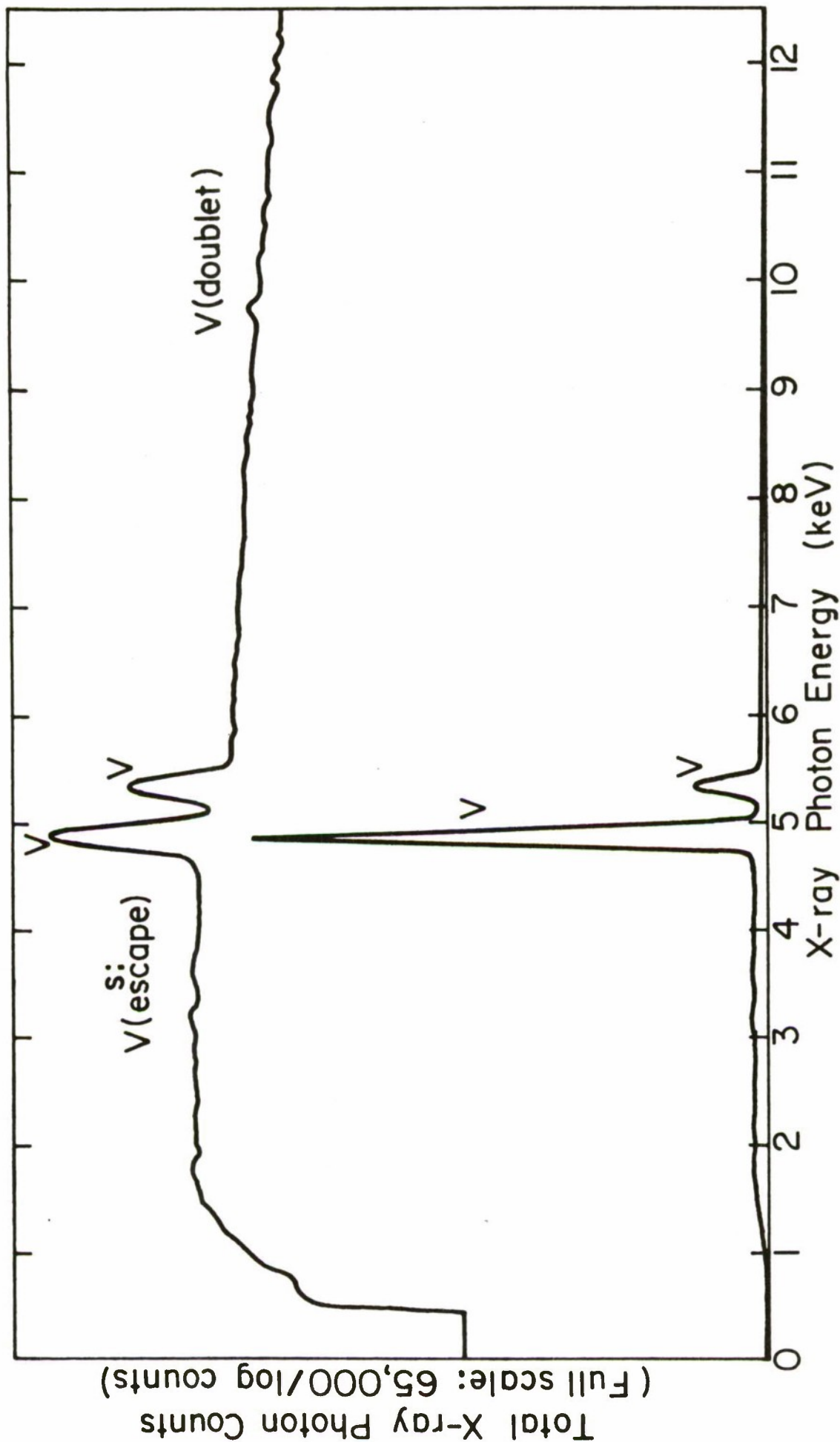
Figure 14.   E.D.X.A. of pure V_2O_5 powder.
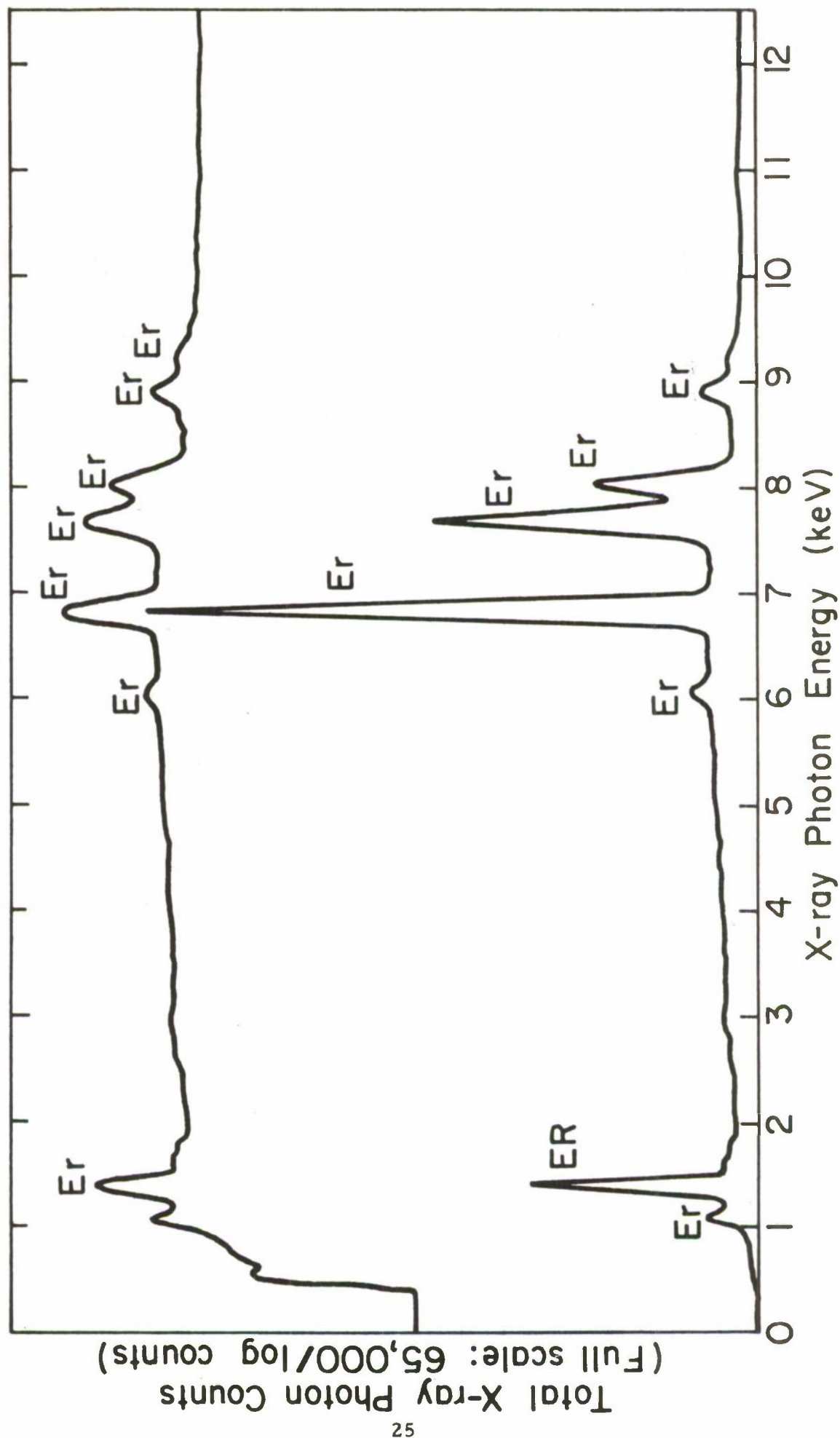
Figure 15. E.D.X.A. of pure Er_2O_3 powder.

25
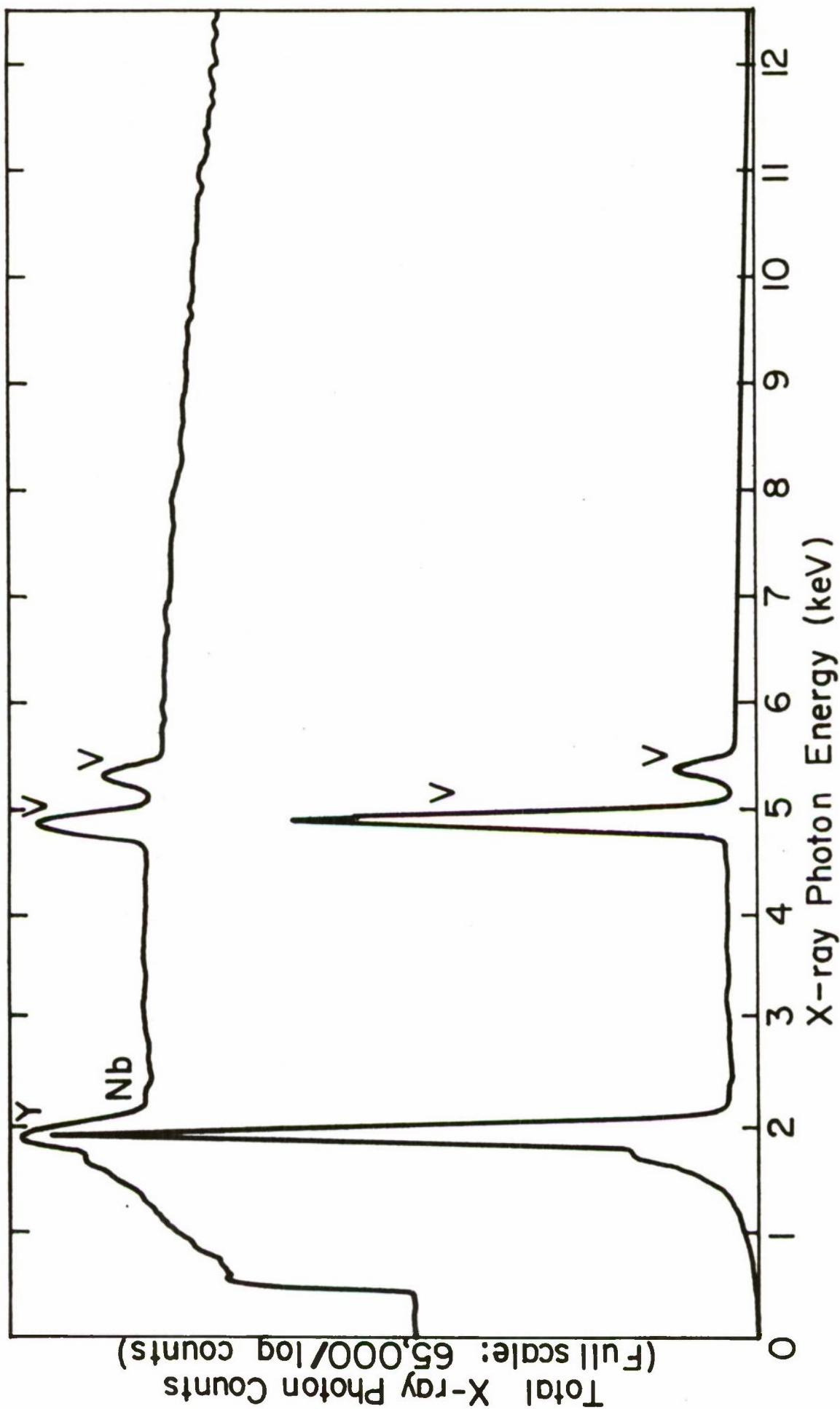
Figure 16. E.D.X.A. of pure YVO$_4$ powder.

Total X-ray Photon Counts
(Full scale: 65,000/log counts)

X-ray Photon Energy (keV)

B. Evaluation of Scattering Centers in Czochralski Grown YVO_4

Two single crystals of YVO_4 grown by Union Carbide Corp. were examined at Aerospace Corp. with a polarizing microscope to see if the centers responsible for laser scattiring could be identified. The crystals were both Nd_2O_3 doped and were delibered from Union Carbide to USC at different times.

One of the crystals was in the form of an "a" axis laser rod. Preliminary examination showed several zones of intense light scattering alont the length of the crystal. Since this crystal was a reject due to the scattering, it was decided to examine it more closely bo optical microscope techniques. Two polished sections ere prepared, one parallel and the other perpendicular to the rod axis. Each section was chosen such that it contained a volume of the original rod that scattered light. Optical examination showed a high volume of scattering centers such as those shown in Figure 17.

High magnification of these scattering centers showed them to have two characteristics as shown in Figure 18a, b. The photomicrographs are taken of the "a" axis slice of the rod. The difference of Figure 18a, b is that each was taken with the polarizer parallel to each of the polarization directions of the (100) plane. For one of the polarization directions the scattering centers appear to be round black dots approximately 4 or 5 microns in diameter. For the other polarization the scattering center appears to be more comples. The rod shaped sharp index change appears around the dot and is aligned in random directions in the crystal. Normally one would assign apparent index changes to diffraction effects around the scattering center. In this case there appears to be a sharp-irregular index change associated with most but not all of the scattering centers. Due to the small size of the scattering centers, one cannot clearly state whether the black dot represents a solid phase or a void in the crystal. However, at this time a best guess would be that it is a void and the endex change represents a rod shaped unknown phase associated with the void. In-as-much as their distribution was not uniform along the length of the laser rod, one can state that the crystal growth was not sufficiently controlled.

27
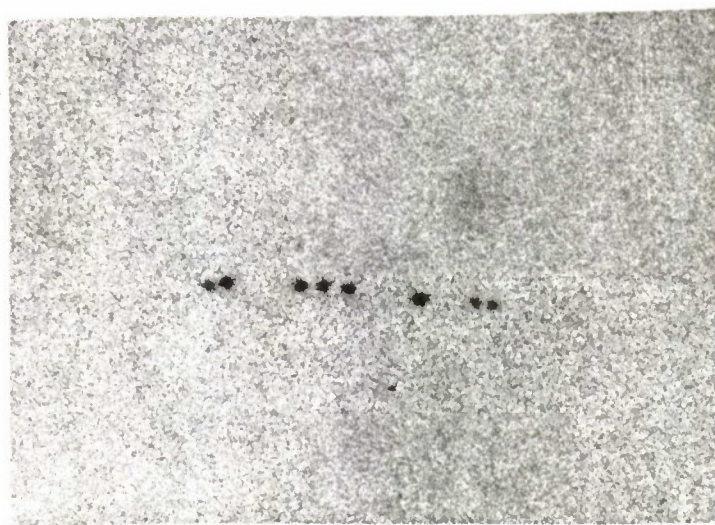
Figure 17. Scattering centers in Nd:YVO$_4$.
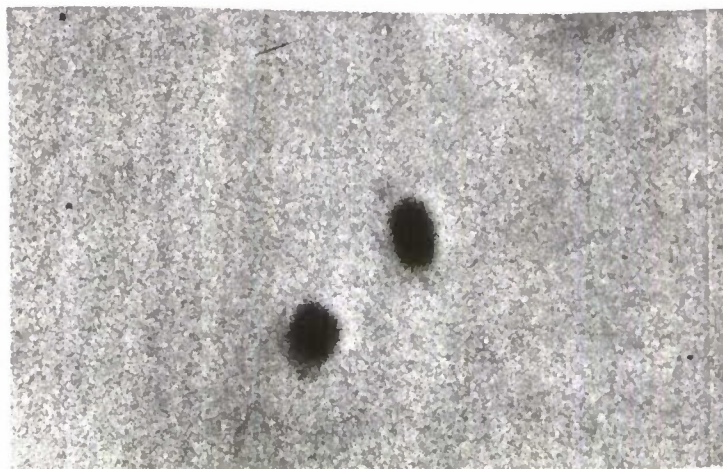
(a)

(b)

Figure 18.   Scattering centers in Nd:YVO$_4$.

The polarization of the illuminating light was
parallel to one of the polarization directions of
(100) plane in (a) and to the other in plane (b).

The other crystal was in the form of a quarter inch polished cube. Microscopic examination revealed that the extinctions in the "a" axis direction were nearly complete and fairly sharp while that in the "c" axis direction was incomplete and poor. The extinction in the "c" direction was light grey for all orientations indicating a "c" axis wander or a constant random strain that varied throughout the length of the crystal. Two types of randomly distributed scattering centers were observed in this crystal. One is of the type shown in Figure 19. The black triangular solid is very thin, absorbs all light, and reflects metalic with incident light. Without either chemical or crystallographic analysis one can only suggest its nature. Generally, it fits the description of a metal such as Ir or Pt. This type of included solid has been found in a number of high melting temperature oxides grown from either Ir or Pt crucibles. Presumably the metal is soluable in the melt, precipitates in the melt and is trapped by the growing crystal. The size varies from 5 to ≈15 microns. The other scattering center observed was an extremely small black dot such as those shown in the photomicrograph The size is 1 to 2 microns and as such is at the resolving limit of the microscope. Both of these defects are randomly distributed over the crystal in zones again indicating a lack of control during the crystal growth process.
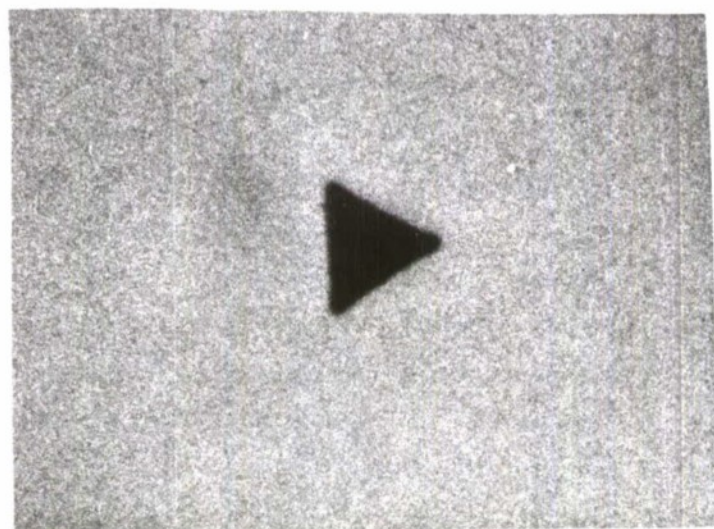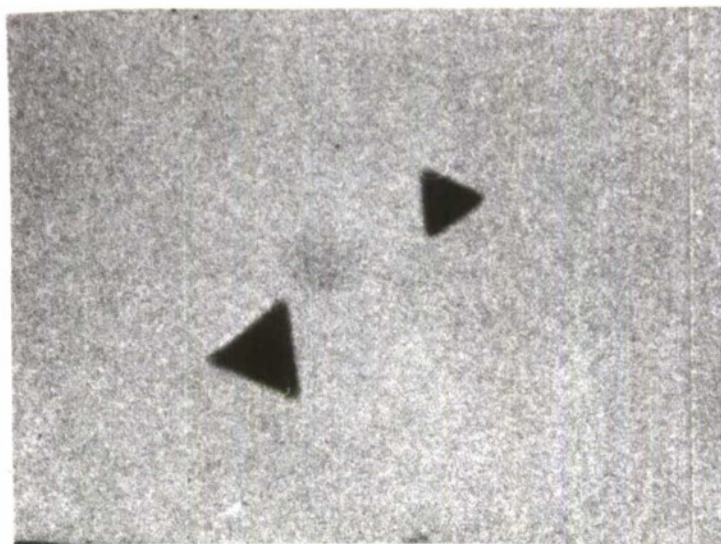
Figure 19. Triangular scattering center in
Nd:YVO$_4$. Possibly Ir or Pt.

C. Flux Growth of YVO_4 at Aerospace Corporation

Single crystals of YVO_4 and $(Er, Y)VO_4$ were grown by standard flux growth techniques in order to compare the defect properties of the crystals grown at low temperatures with those grown by Union Carbide by melt techniques. A small number of crystal growth runs were required in order to produce the necessary crystals. The crystals were checked with a polarizing microscope to determine the structure. They are optically uniaxial with the same optical properties as tetragonal YVO_4.

The crystals of YVO_4 and Rare Earth doped YVO_4 were grown from a V_2O_5 flux by standard flux growth techniques. They were grown from a solution supersaturated by both slow cooling and flux evaporation. The chemicals used for the growth of YVO_4 were American Potash code 116 Y_2O_3, and J. T. Baker Co. Reagent Grade V_2O_5.

Standard form 50 mil platinum crucibles were filled with the appropriate powder mixtures, their lids tightly crimped, and placed in a Super-Kanthal heated muffler furnace. They were heated to $1250°C$ soaked 4-8 hours, programed cooled at a rate of approximately $4°C/hr$, then removed from the furnace and allowed to cool to room temperature. The crystals were removed from the crucibles by soaking in hot dilute HNO_3 or HCl. The melt compositions used varied from 4 to 10 mole % Y_2O_3 with remainder being V_2O_5. The crystals nucleated throughout the melt and varied in size from 0.5 - 3 mm. They were of two diverse habits (plate-like and equidimensional) with the largest being of the plate type. The dimensions of the plate-like crystals were approximately 3 by 4 mm with a thickness that varied from 0.1 to 0.5 mm. The equidimensional crystals were generally ≈ 0.5 mm with a few as large as 2 mm. No significant change in habit was detected with up to 10% of the Y_2O_3 being replaced by rare earth ions.

The crystals varied from colorless to pale yellow from run to run with no indication of any direct cause. It is felt that this was due to impurities in the melt as little care was taken to insure high purity growth materials or to eliminate introduction of impurities into the melt. Some of the larger plate-like crystals had ordered trapped flux inclusions parallel to the major growth

planes. This type of defect can generally be minimized by judicious choice of the growth parameters. Other than these defects, the crystals appear to be high quality with no visible index changes or strain birefringence.

The basic habit of the crystals is that of {100} prism faces modified by {101} pyramid faces (see Figures 20 and 21). The small equidimensional crystals show a good tetragonal symmetry with all of the faces being approximately equal in size. The plate-like crystals, on the other hand, show a decided lowering of symmetry to that of a orthorhombic crystal. The gross variation of habit, i.e., from equidimensional to plate-like, can be related either to the growth temperature or to some significant change in the growth mechanisms of the crystal. The small equidimensional crystals clearly grew throughout the melt when the crucibles were removed from the furnaces and as such grew rapidly. The plate-like crystals grew at higher temperatures throughout the program cycle of the furnace and consequently at a much slower growth rate. Such changes in habit are generally assigned to some major changes in the crystal growth kinetics such as growth mechanisms, super-saturation, etc. In addition, changes of this type normally involve the introduction of new faces or a major reordering of growth rates the existing faces. This particular case is somewhat unusual in that all the faces are of the same type and the change of morphologic symmetry primarily related to a surface energy change of the (100) and (010) planes. This is unexpected for tetragonal crystals where one would anticipate variations only in the c/a lengths of the crystals dependent on some kinetic change of the growth system. In the absence of twinning or some recognizable growth feature as being responsible for such a change in habit one must look elsewhere for its cause. It is unlikely that impurities could affect the habit in this way for the (100) and (010) planes in the tetragonal crystal system are equivalent planes and should not be affected differently. About the only remaining cause is a structural one. If so, and the full morphologic symmetry is applied then the crystal must have existed at the growth temperature with a lower symmetry than tetragonal. The full morphological description by faces type being $(100) \gg (010)$ with the $(\bar{1}00) > (100)$ and the $(011) = (0\bar{1}1)$ with $(101) \gg (\bar{1}01)$. One striking feature of

{100}, CLEAVAGE

(011)

(010)

<001>

{100}

c

(101)

(100)

(011)

(01̄1)

(101)

(010)

End view of crystal
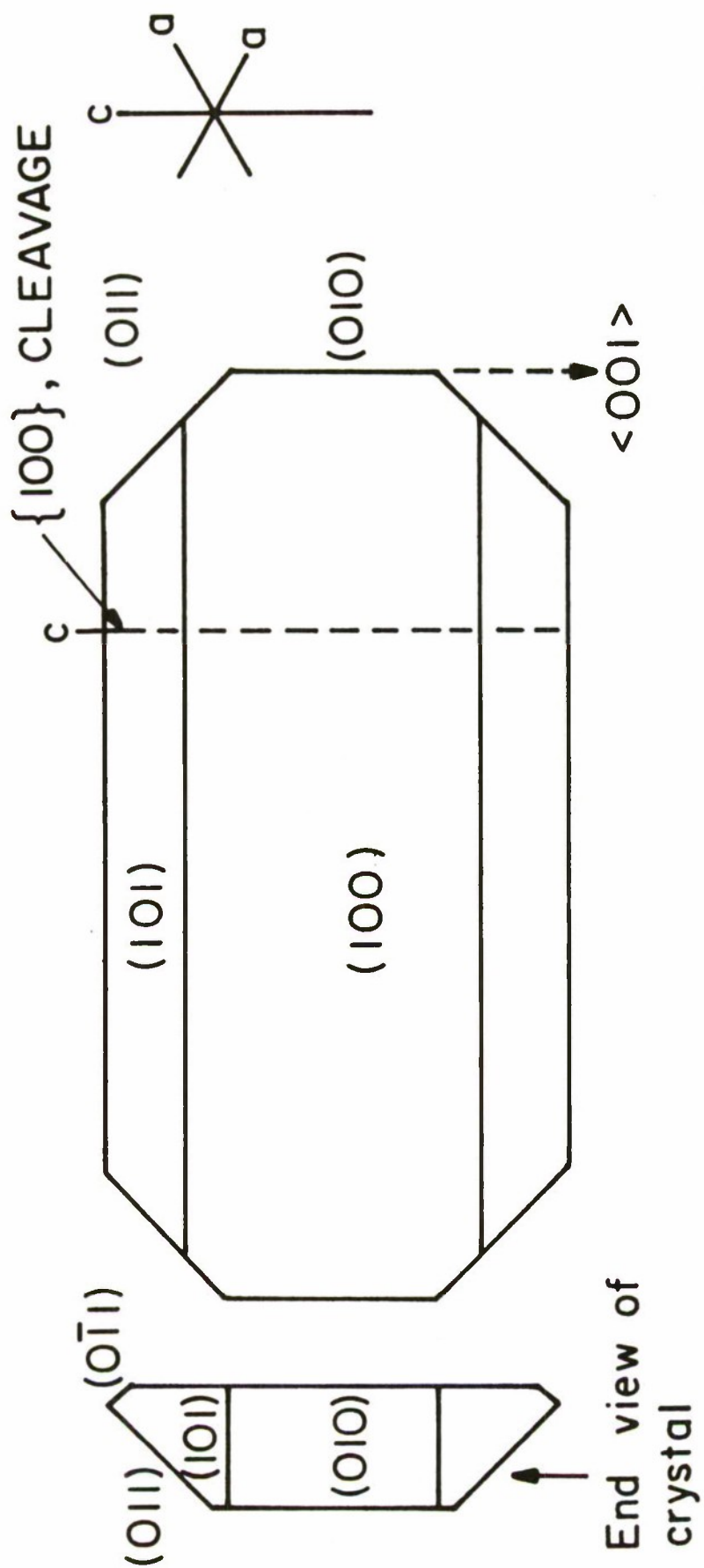
Figure 20. Plate habit of YVO$_4$.
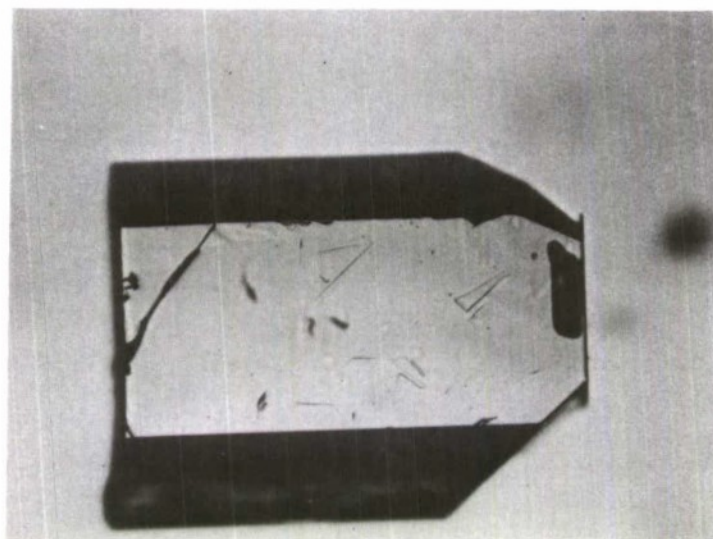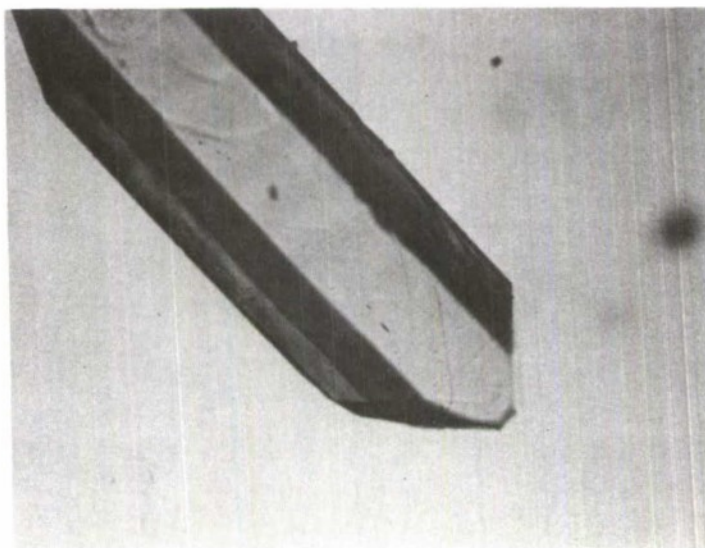
Figure 21. Flux Grown YVO$_4$ Crystals

35

the crystals is that the ($\bar{1}01$) is consistently much smaller than the (101) or is absent. This implies that the crystal had an orthorhombic distortion with $a_1 \neq a_2$ and a loss of symmetry along with a axis with a result that the (100) and ($\bar{1}00$) as well as the (101) and ($\bar{1}01$) planes becoming unequivalent. Optically, the crystal appears to be uniaxial as in the case for zircon.

III. SPECTROSCOPY OF RARE EARTH IONS IN YVO_4

A. Introduction

The present interest in rare-earth-doped yttrium orthovanadate (YVO_4) stems from recent studies [6, 7] which showed that an experimental laser rod of $Nd:YVO_4$ in a pulsed-lamp laser configuration had a threshold at 1.06 μm about a factor of two lower than a standard quality Nd:YAG laser rod in the same configuration. Furthermore, the performance of the vanadate material in a CW laser configuration was comparable to the garnet even though the vanadate sample had larger scattering losses [8]. These observations arise out of the fact that thw 1.06 μm laser cross section in YVO_4 is 4.6 times greater than that of Nd:YAG. In addition, the 1.34 μm operation of the $Nd:YVO_4$ laser completely outperformed that of Nd:YAG at 1.32 μm because of an 18 times larger laser cross section of the vanadate relative to the garnet [8].

The first study of a laser using $Nd:YVO_4$ was made in 1966 by O'Connor [1] who reported a pulsed-laser threshold at 1.06 μm of ~1 J. Difficulties in crystal growth prevented this work from progressing. However, recent advances in the growth of this crystal [3] have shown that YVO_4 is now a promising laser material. This is especially so because of its very desirable mechanical, optical, and physical properties. For example, it has excellent optical finishing properties because of its glass-like hardness, it has only a slight tendency to cleave, and it has a high laser-induced damage threshold. Since it is a strongly birefringent uniaxial crystal, the dopant transitions are polarized; the lasing transitions are strongly polarized parallel (π-polarized) to the optic axis (c-axis). The strong birefringence makes possible electrooptic Q-switching without an intracavity polarizer [6, 7].

Further studies of $Nd:YVO_4$ were described in 1968 by Bagdasarov

et al. [9] and in 1969 by Kaminskii et al. [10]. These papers reported not only a low threshold for lasing (~2 J) using this material, but they also gave spectroscopic data for transitions of Nd^{3+} at 4.2, 77, and 300°K. The work of DeShazer et al. [6] and of Bass et al. [7] presented energy levels, line-widths, and peak cross-sections for the $^4F_{3/2} \rightarrow {}^4I_{11/2}$ fluorescence transitions and energy levels of the $^4F_{3/2} \leftrightarrow {}^4I_{9/2}$ transitions all at room temperature as well as laser performance data. In addition, unpublished spectroscopic studies by Pressley et al. [11] and by Karayianis et al. [12] have been circulated wherein attempts were made to identify the energy level scheme, particularly of the above mentioned manifolds. Among the studies of these four groups, there is (1) only partial agreement as to the positions of the Stark levels in the $^4I_{9/2}$ ground level, (2) no agreement on the group theoretical identity of the levels, and (3) no explanation of the absence of certain lines from the $^4F_{3/2} \leftrightarrow {}^4I_{9/2}$ transition group. For example, Bagdasarov et al. [9] and Kaminskii et al. [10] did not report on polarized spectra or any level identities. On the other hand, Karayianis et al. [12] and Bass et al. [7] both report polarized spectra, but their level identities do not agree.

In the work described here, the $^4I_{9/2} \rightarrow {}^4F_{3/2}$ and $^2P_{1/2}$ polarized absorption spectra and the $^4F_{3/2} \rightarrow {}^4I_{9/2}$ and $^4I_{11/2}$ polarized fluorescence spectra, recorded at ~85°K and room temperature, are presented and analyzed. We show that the spectra provides for unambiguous level assignments. By examining the details of crystal field theory and the Judd-Ofelt [13] theory of induced electric-dipole transitions as applied to $Nd:YVO_4$, we offer some possible explanations for the observed relative line strengths.

B. Experiment

The samples of $Nd:YVO_4$ studied were obtained from two batches of crystals grown by Crystal Products Department, Union Carbide Corporation,

38

San Diego, California. The first batch was produced by Dess and Bolin [5] in 1967-68, and the second batch by Rothrock and Wilder [14] in 1973-74. Although the crystal from the first batch had a greenish tint added to the usual sky blue color, the spectra were essentially the same. This green tint was produced by color centers in the crystal. The Nd^{3+} concentration was nominally 1 atomic percent.

The absorption measurements were made usually by illuminating the crystal transversely to the c-axis with parallel light from a quartz-iodine tungsten lamp. This allowed the Glan-Thompson polarizer to be set either parallel (π-polarization) or perpendicular (σ-polarization) to the c-axis. The experiment is shown schematically in Figure 22.

The spectrograph used was a 1-meter Czerny-Turner mounting fitted with an uncooled 7102 photomultiplier which was connected to a lock-in amplifier and a log-converter (the latter being used only with absorption spectra). The linear reciprocal dispersion of the spectrograph was about 16 Å/mm in first order. Corning glass filters were employed as needed to remove unwanted orders and to avoid excitation of fluorescence transitions during the absorption measurements.

The fluorescence experiments were performed by focusing the beam from an argon-laser-pumped Spectra-Physics dye laser along the direction orthogonal to both the c-axis and the observation axis. The dye laser polarization was parallel to the c-axis and the maximum fluorescence output was obtained with the excitation set at about 583 nm. The dye laser power was about 60 mW incident in the crystal.

The spectrograph was made insensitive to the incoming polarization by inserting a calcite wedge in front of the slit with the optic axis set at 45° to the slit. With the quartz-iodine lamp. we observed about a 2% change in the recorded signal for a 180° rotation of the polarizer with respect to the polarization requires that the illumination of the slit be reasonably uniform along the height of the slit and that the image on the slit cover at least a
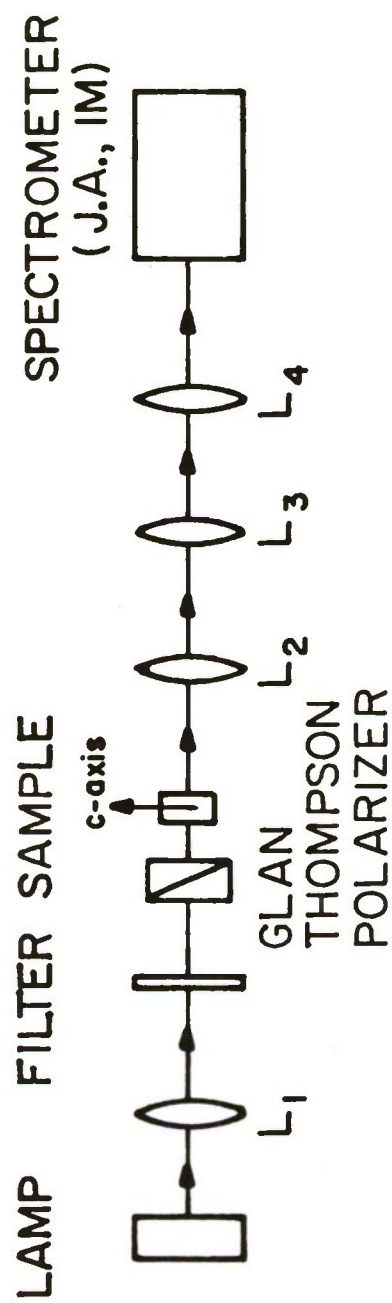
Figure 22. Experimental arrangements for absorption spectroscopy.

few millimeters of the slit height.

Wavelength calibration was accomplished by using Osram mercury or neon gas discharge lamps and superimposing the spectra from these lamps on the experimental spectra by a partially reflecting mirror on the optical axis of the spectrograph entrance slit.

C. Spectra

Since out primary objective was to clarify the positions and identities of the levels of the $^4I_{9/2}$ ground state and of the $^4I_{11/2}$ and $^4F_{3/2}$ states of interest in laser applications, we emphasize the better resolved spectra taken at ~85°K; however, for completeness we also present data taken at room temperature.

The absorption and fluorescence spectra used in the analysis is shown in Figures 23 through 26. All these spectra shown were taken using a sample 7.8 mm thick taken from Boule 3L of Rothrock and Wilder. Absorption spectra taken at both temperatures with boule 3L samples and the Bolin-Dess samples in longitudinal illumination (i.e., along the c-axis and with no polarizer) showed excellent agreement with the corresponding σ spectra shown in the figures, both in line positions and relative strengths. The strengths of these longitudinal σ-spectra were a factor of two larger than their corresponding transverse σ-spectra as is expected from the simple theory of the radiation pattern of a σ transition. On the other hand, as can be seen in the figures, the π-to-σ strength ratios do not follow any simple relationship. These ratios can be understood only after a careful examination of the J_z composition of the crystal field levels as it influences the transition matrix elements obtained from the Judd-Ofelt theory [13].

41
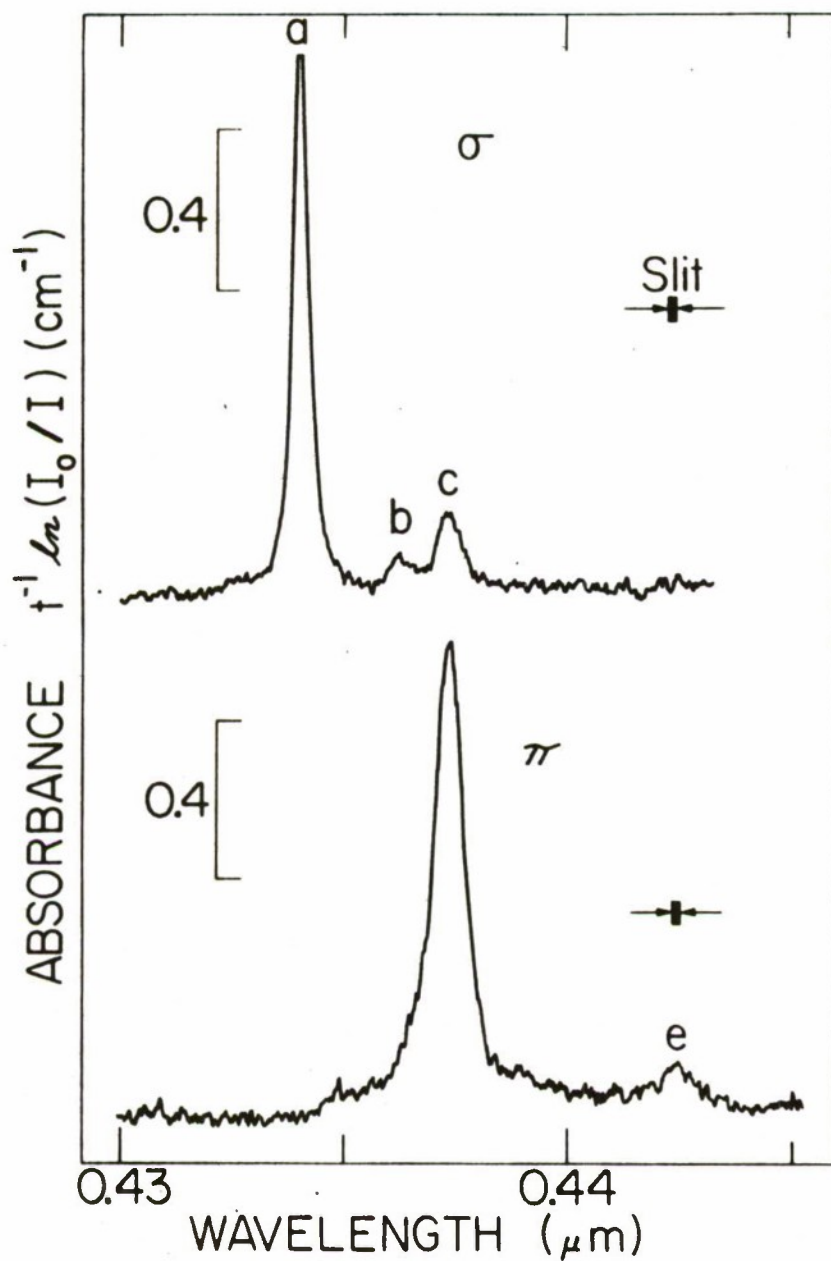
Figure 23. Polarized absorption spectra of the $^4I_{9/2} \rightarrow {}^2P_{1/2}$ transitions of Nd:YVO$_4$ at ~300°K. The letters a, b, c, and e denote the crystal field levels of the $^4I_{9/2}$ state. The c-axis was transverse to the observation axis.
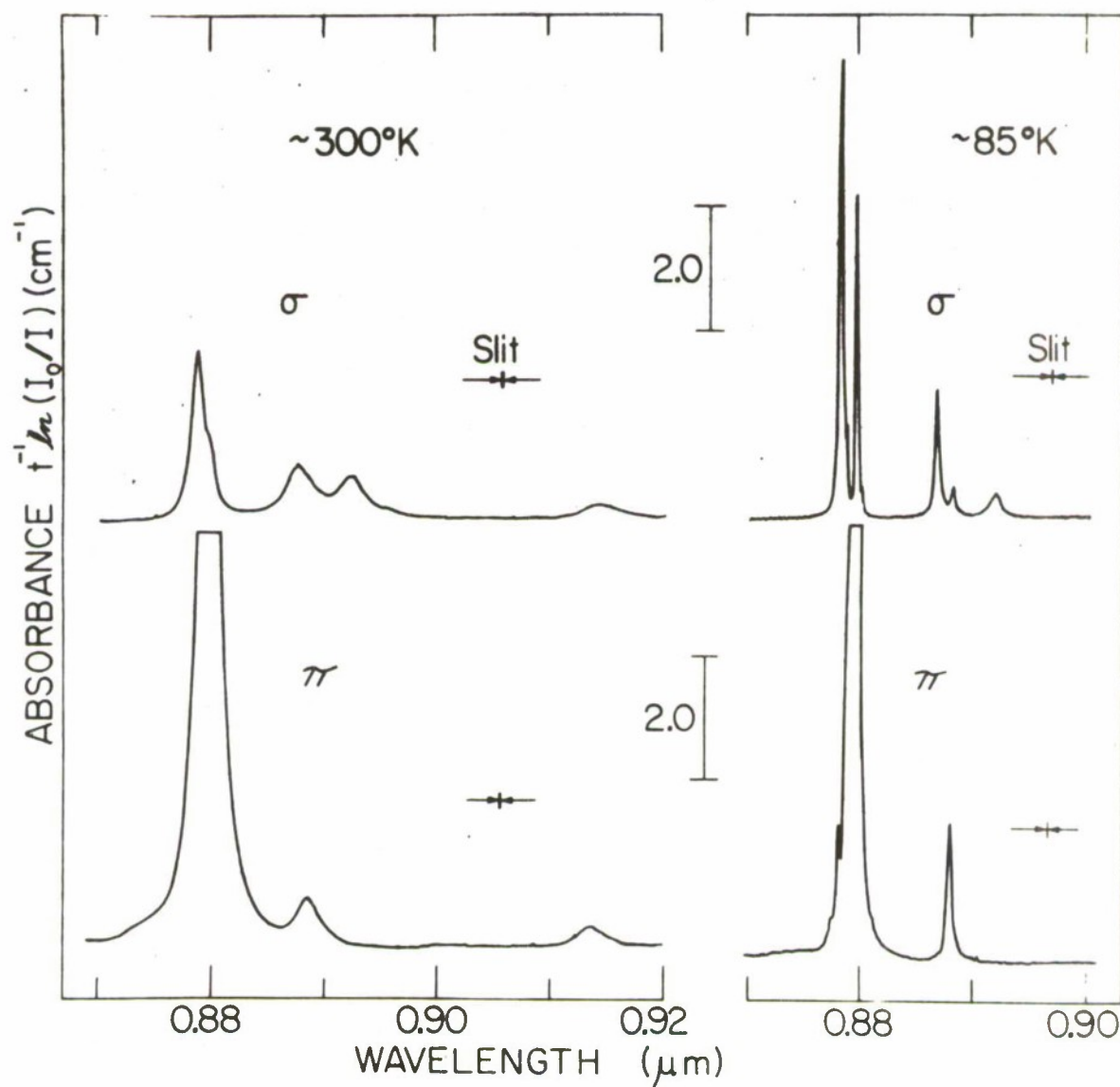
Figure 24. Polarized absorption spectra of the $^4I_{9/2} \rightarrow {}^4F_{3/2}$ transitions of Nd:YVO$_4$ at two temperatures. The peak of the flat-topped π-line at ~300°K was determined to be at 18.5 cm^{-1}. Crystal oriented as in Figure 23.

43
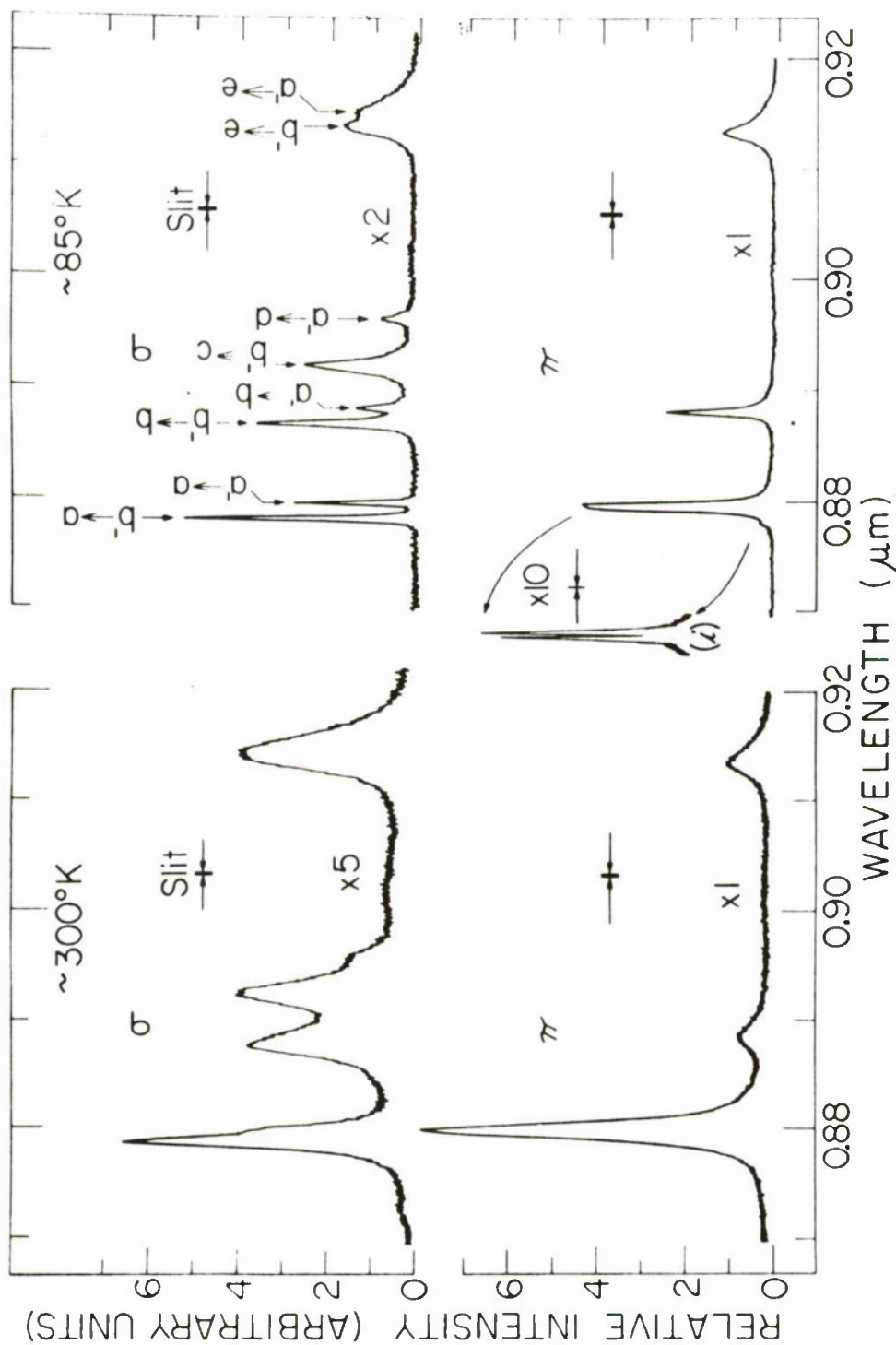
Figure 25. The dye-laser-excited, polarized fluorescence spectra of the $^4F_{3/2} \rightarrow {}^4I_{9/2}$ transitions of Nd:YVO$_4$ at two temperatures. The gain factors ×1, etc., apply only within the given temperature. The letters a' and b' denote the crystal-field levels of the $^4F_{3/2}$ state while the unprimed letters identify the levels belonging to the $^4I_{9/2}$ state. The inset (i) shows the self-absorption which occurs when the dye laser beam is moved back from the observed surface. Crystal oriented as in Figure 23.

44
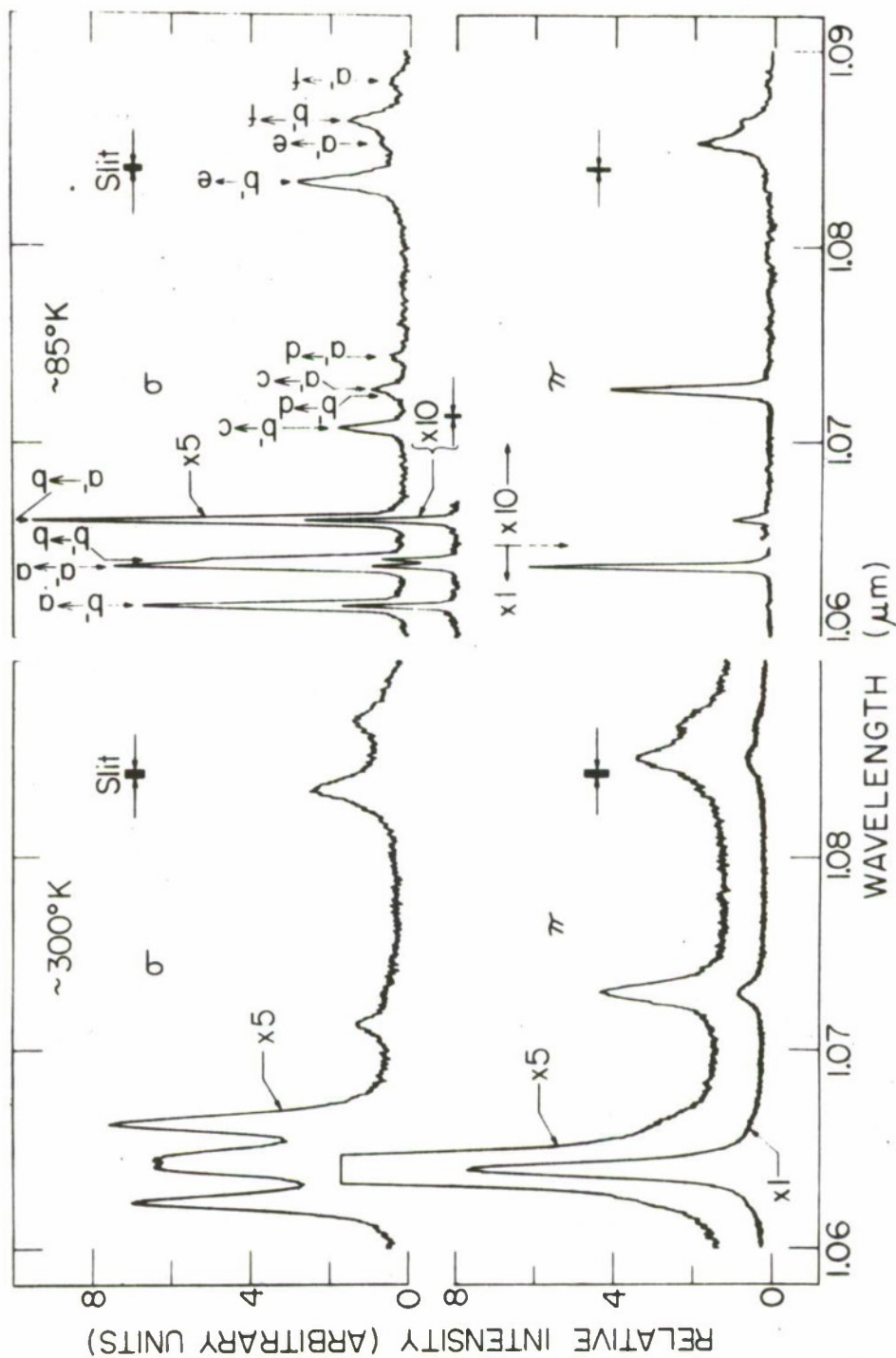
Figure 26. The dye-laser-excited, polarized fluorescence spectra of the $^4F_{3/2} \rightarrow {}^4I_{11/2}$ transitions of Nd:YVO$_4$ at two temperatures. The gain factors ×1, etc., apply only within the given temperature. The letters a' and b' denote the crystal-field levels of the $^4F_{3/2}$ state while the unprimed letters identify the levels belonging to the $^4I_{11/2}$ state. Crystal oriented as in Figure 23.
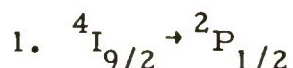
1. $^4I_{9/2} \rightarrow {}^2P_{1/2}$

The spectra (taken in third order) for the $^4I_{9/2} \rightarrow {}^2P_{1/2}$ transitions in Figure 23 are given only for room temperature since they show the transition originating from the highest level of the $^4I_{9/2}$ manifold. This transition is frozen out (i.e., the initial level is thermally depopulated) at ~85°K. The spectral region of these transitions was carefully searched at both temperatures and polarizations for additional lines corresponding to transitions to the ground state levels other than the five shown in Figure 23. None were found.

We do see in the π-polarization spectrum in Figure 23 a weak and very broad band under the strong line. Similar bands are found in nearly all spectra; yet, they were too weak, too broad, insufficient in number, and not consistent in their observed pattern to be considered part of the electronic transitions associated with the primary site population of the Nd^{3+} ions.
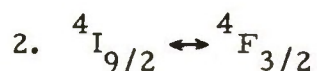
2. $^4I_{9/2} \leftrightarrow {}^4F_{3/2}$

Figures 24 and 25 show the absorption and fluorescence spectra for the $^4I_{9/2} \leftrightarrow {}^4F_{3/2}$ transitions at the two temperatures. Because of the large thickness of the sample used to obtain these spectra, the high-cross-section transitions completely absorb the incident light thereby causing these lines to become flat-topped. The large thickness was used to insure that all pertinent electronic transitions were found.

In fluorescence, the strong π transition was observed to be quickly self-absorbed as the excitation beam was moved back from the sample surface. Self-absorption means that, since these transitions terminate on the ground manifold, the fluorescence is subject to absorption during passage out of the sample. As seen in Figure 25, some residual self-absorption remains at ~85°K even though some effort was made to place the beam to within a tenth of a millimeter of the sample surface. An inset in the figure

shows how strong self-absorption occurs when the beam is about 1-2 mm back from the surface.

In absorption, we note that the lowest wavelength line which appears in σ spectrum at ~85°K also appears in the corresponding π spectrum as well as in the ~85°K π-fluorescence spectrum. This behavior is also observed in the $^4F_{3/2} \rightarrow {}^4I_{11/2}$ π-fluorescence spectra shown in Figure 26 wherein two σ lines appear on either side of the strong π line in the low temperature spectrum. These lines are not apparent in the corresponding room temperature spectra because of interference from the neighboring strong π line. These observations may have been caused by polarizer or sample misalignment. However, the lines appeared in independent experiments on different samples. Thus, we are led to the possibility that the selection rules are broken which could mean that the Nd^{3+} site symmetry is lower (i.e., C_{2v}) than the normal symmetry at that site.

The situation is complicated by the fact that all of our samples showed strong and complicated strain patterns when viewed along the c-axis between cross polarizers. These patterns would completely change with only slight changes in the sample orientation. When viewed perpendicular to the c-axis, comparatively few patterns were observed with good extinction being achievable at the appropriate orientations. Thus, it is possible that the anomoly described above is produced by crystal imperfections such as would produce wandering of the c-axis through the crystal.

Bagdasarov [9] reported two sites which they designed I and II. Our results are in good agreement with their Stark level positions for type I sites. We do not observe any lines which we can identify with type II sites. In addition, they reported weak lines on the long wavelength wings of the strong σ lines in the $^4F_{3/2} \rightarrow {}^4I_{11/2}$ fluorescence spectrum at 77°K which they called "companions." We see similar lines on the strong σ lines in the absorption spectrum for ~85°K shown in Figure 24. These lines are spaced about 1 cm^{-1} less than their strong neighbors. The

sharpness of these weak lines suggests that they are from a well defined Nd^{3+} site, and their smaller spacing indicates a slightly weaker crystal field. Examining the crystallographic data given by Wyckoff [15] for crystals having the zircon structure illustrated in Figure 27, we calculate a yttrium-oxygen nearest-neighbor spacing in YVO_4 to be 2.296 Å. Using the following radii, Nd^{3+}-1.08Å, Y^{3+}- 0.93Å, and O^{2-}-1.40Å, we find the Y-O nearest-neighbor spacing of the Y^{3+} site to be 0.184Å smaller than the radius of the Nd^{3+} ion as compared to a 0.034Å mismatch for the Y^{3+} ion. The mismatch of Nd^{3+} is certainly sufficient to introduce the possibility of a site arising from a slight well-defined distortion of the basic D_{2d} symmetry normally present at the Y^{3+} site
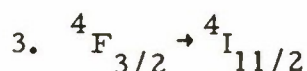
$$3. \quad {}^4F_{3/2} \rightarrow {}^4I_{11/2}$$

The fluorescence spectra at room temperature and ~85°K for the ${}^4F_{3/2} \rightarrow {}^4I_{11/2}$ transitions are given in Figure 26. After group theory there should be 12 σ and 6 π lines. Only the low temperature σ spectrum shows the required 12 lines. In the π spectrum, neglecting the 2 anomolous σ lines discussed above, we have only 4 lines. We propose that these two anomalous σ lines are not the two missing π lines. In support of this claim is the fact that in all the other spectra, a π line is never significantly increased in strength by changing to σ polarization contrary to the behavior of the anomolous σ lines. The strong π line appears in σ polarization as the second of the four strong lines, counting from the short wavelength end. We shall identify the third line of this group as being one of the missing π lines. This line can be seen on the long-wavelength side of the strong π line only as an asymmetry in the lower half of the strong π line.

The spectra given in Figure 26 for ~85°K was not taken with sufficient gain to reveal the "companion" lines discussed in the previous subsection. With higher sensitivity, we observe the companion lines reported by Bagdasarov [9] for the ${}^4F_{3/2} \rightarrow {}^4I_{11/2}$ transitions.

D. Analysis

1. Site Symmetry

The structure of YVO_4 is that of zircon which is tetragonal and belongs to the space group D_{4h} [15]. The Y^{3+} site symmetry in which the Nd^{3+} ions are found is D_{2d}. Referring to Figure 27, the Y^{3+} ion is at the center of a tetrahedron formed by four nn O^{2-} ions. The reduction to D_{2d} symmetry arises from the fact that this tetrahedron is shorter along the c-axis than the corresponding dimensions perpendicular to the c-axis. In addition, this irregular tetrahedron is surrounded by four nn Y^{3+} ions and their O^{2-} tetrahedra which are located below, left and right, and above, front and back, of the site in question. These four Y-O tetrahedra form a larger irregular tetrahedron at the center of which is the site in question. This large tetrahedron is oriented 90° from the orientation of the Y-O tetrahetron at its center. The V^{5+} ions are not seen by the Y^{3+} ions in the first approximation since each V^{5+} ion, due to its small size $(0.59Å)$ is completely shielded by a tetrahedron of O^{2-} ions.

This intermingling of tetrahedra produces two kinds of equivalent Y (hereafter the superscript for charge is suppressed) sites related to each other by a 90° rotation about the c-axis. It is possible that the mismatch between Nd and the Y site described in the previous section could remove the equivalence of a fraction of these two sets of sites thereby giving rise to another set of sharp lines.

We also note that neodymium ions located in nn Y sites would be expected to see a significantly lower symmetry and larger crystal fields. It is possible that the lines identified as site II by Bagdasarov [9] are from Nd ions in double clusters since their spectra were taken with samples having about twice the Nd concentrations as our samples which makes the concentration of double clusters four times larger in their samples compared to ours.
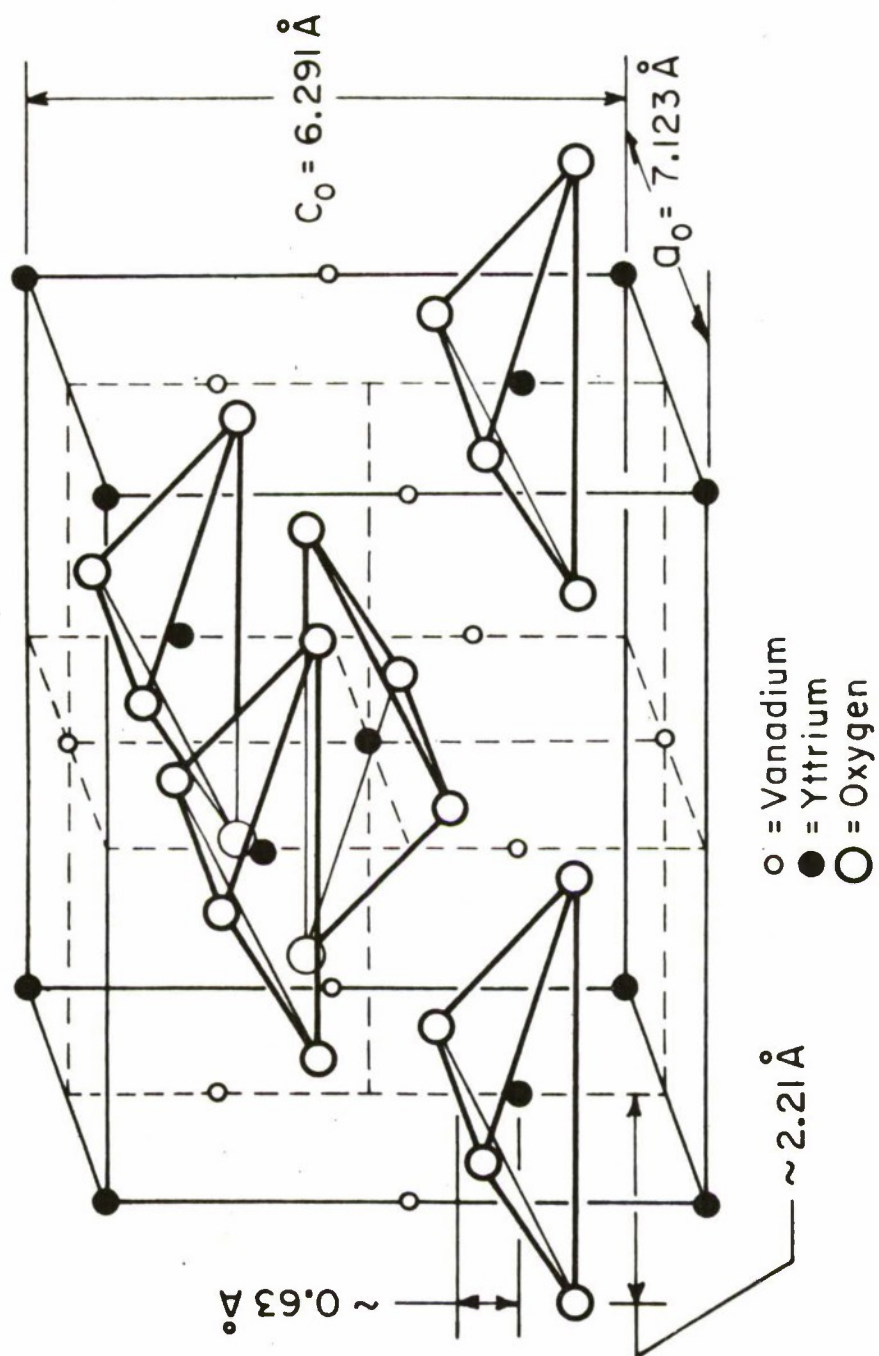
Figure 27. The tetragonal unit cell (D_{4h}^{19}) of yttrium vanadate after Wyckoff (Ref. 15). The cell contains four YVO_4 molecules. Eight face-oxygen ions associated with four vanadium-oxygen tetrahedra that are located at the four off-center face positions of vanadium have been omitted from the cell to enhance clarity.

o = Vanadium
● = Yttrium
O = Oxygen

$C_0 = 6.291$ Å

$a_0 = 7.123$ Å

~2.21 Å

~0.63 Å

2. Electric Dipole Transitions Between Crystal-Field Levels

The importance of $Nd:YVO_4$ is in the larger cross section and the corresponding higher gain of the laser transition compared to the laser transition in Nd:YAG [6, 7]. An understanding of this difference can be obtained by analyzing how the crystal fields of the two hosts influence the dipole oscillator strengths of transitions between the $^{2S+1}L_J$ manifolds of rare earth ions in crystals can be expressed as

$$f_{J \rightarrow J'} = \sum_{t=2,4,6} \nu \, T_t \, (2J+1)^{-1} \, |\langle [\tau SL]J \| U^{(t)} \| [\tau'SL']J' \rangle|^2 \qquad (1)$$

where ν is the center-of-gravity frequency of the transition group, the parameters T_t includes quantities which characterize the opposite-parity configurations and the strength and symmetry of the crystal field, the reduced matrix elements are of the unit tensor calculated in the intermediate coupling scheme, and the remaining symbols have the usual meanings. The usual procedure is to fit the T_t parameters using experimental oscillator strengths. Unfortunately, this approach does not predict the oscillator strengths of transitions between specific crystal field levels. In fact, the parameters T_t cannot be used to determine these strengths since the scheme by which the available oscillator strength is portioned out to the symmetry-allowed transitions is directly determined by the specific distribution and the type of ions surrounding the rare-earth ion and the J_z content of the crystal-field levels (which is also directly related to the surrounding environment of ions), while both of these details are removed from T_t parameters by summations over all possible values. As it will be shown, it is these details of the crystal field interaction with Nd that make the YVO_4 host of special interest. To make this evident, we shall draw on comparisons with YAG and $CaWO_4$.

Equation (1) is obtained from a more general expression of the Judd-Ofelt [13] theory which includes an accounting of the details of the crystal field and the J_z mixing. A useful form of this expression for the oscillator strength of a transition between two crystal field levels α and β for polarization orientation $\vec{\epsilon}$ is given by

$$f_{\alpha \to \beta \vec{\epsilon}} = \nu_{\alpha\beta} \left| \sum_t (2t+1) \langle U^{(t)} \rangle \sum_k \Xi'(k,t) \sum_{q,\rho} (-1)^{q+\rho} \epsilon_\rho^{(1)*} A^k_q \right.$$

$$\left. \times \, \mathcal{T}^{(t)}_{q+\rho} \begin{pmatrix} 1 & t & k \\ \rho & -(q+\rho) & q \end{pmatrix} \right|^2 , \qquad (2)$$

$$t = 2, 4, 6, \quad k = 1, 3, 5, 7, \quad |q| \leqq k, \quad \rho = 0, \pm 1,$$

where $\nu_{\alpha\beta}$ is the transition frequency, the $\langle U^{(t)} \rangle$ are the matrix elements which are the same as in Eq. (1), the $\Xi'(k,t)$ are parameters which contain quantities that characterize the opposite-parity configurations which are responsible for inducing the electric dipole transitions within the 4f configuration and other constants, and the $\epsilon_\rho^{(1)*}$ are the complex conjugates of the polarizer components in tensor form where $\rho = 0$ corresponds to π transitions and $\rho = \pm 1$ are for σ transitions. The A^k_q are the parameters of the odd-parity terms (i. e., k odd) in the usual multipole expansion of the crystal-field potential energy V_c. They are functionally dependent on the coordinates of the surrounding charges. We note that these odd-parity terms can only be non-zero in sites lacking inversion symmetry. The quantities $\mathcal{T}^{(t)}_{q+\rho}$ are given by

$$\mathcal{T}^{(t)}_{q+\rho} \equiv \sum_{\zeta \zeta'} C^*_\alpha (J_z) C_\beta (J_z') (-1)^{J-J_z} \begin{pmatrix} J & t & J' \\ -J_z & q+\rho & J_z' \end{pmatrix}, \qquad (3)$$

where the C's are the J_z-mixing coefficients and the ζ's are integers that specify which J_z values are present in the corresponding states, and

52

therefore, which are to be considered in the summations of Eq. (3). The values of the J_z-mixing coefficients are obtained from the crystal field calculation which requires detailed knowledge about the spectra. This calculation involves products in V_c of the form

$$V_c \propto A_q^k \begin{pmatrix} J & k & J' \\ -J_z & q & J_z' \end{pmatrix} , \tag{4}$$

where k = 2,4,6 only and the 3-j symbol is identically zero when the numbers in the top row cannot form a triangle or when the sum of numbers in the bottom row is not zero. In the absence of any external fields, the states of the ion are specified by a single value of J. However, the 3-j symbol in Eq. (4) connects states having different J and J_z values. Thus J and J_z are no longer good quantum numbers in the presence of a crystal field.

In the description of crystal-field splitting, Hellwege [16] showed that for sites having a well-defined p-fold rotational symmetry axis, the J_z composition of a crystal-field level is determined by a crystal-field quantum number μ as given by

$$J_z = \mu + \zeta p \equiv \mu \ (\mathrm{mod}\ p) \tag{5}$$

where p is the fold symmetry of the axis of the crystal field (assuming only non-cubic symmetries), and $\zeta = 0, \pm 1, \pm 2, \ldots$ In Nd:YAG, the Nd site symmetry is D_2 with p = 2. However, in Nd:YVO$_4$, the site symmetry is D_{2d} which includes, in addition to three 2-fold rotational axes, a S_4 symmetry operation which is a pure rotation of 90° followed by a reflection in a plane perpendicular to the axis of rotation about one of these axes (i.e., the z axis). As the result of this operation, Eq. (5) is no longer sufficient to describe the decomposition of an arbitrary J state in a D_{2d} crystal field. This can be understood by determining the requirements that the S_4 operation places on the crystal-field wave functions.

In general, the states associated with a crystal-field level α of a

given J manifold can be written as

$$|\alpha\mu\rangle = \sum_{\xi} C_{\alpha}(\mu J_z)|J_z\rangle \quad , \tag{6}$$

where the $C_{\alpha}(\mu J_z)$ are the same as in Eq. (3) and the summation is over values of ξ to be determined. The S_4 and S_4^{-1} operations are equivalent to a 4-fold rotation followed by inversion as specified by IC_4^{-1} and IC_4, respectively. A p-fold rotation operation $\mathcal{D}(2\pi/p)$ followed by the inversion operation $\mathcal{I}$ can be expressed as [15]

$$\mathcal{S}|\alpha\mu\rangle = S|\alpha\mu\rangle , \tag{7}$$

where $\mathcal{S} \equiv \mathcal{I}\,\mathcal{D}(2\pi/p)$ and the operations are defined as follows:

$$\mathcal{I}\,\psi_{J_z}(x, y, z) = \psi_{J_z}(-x, -y, -z) = (-1)^{\sum_i \ell_i}\psi_{J_z}(x, y, z),$$

and

$$\mathcal{D}(2\pi/p)\,\psi_{J_z}(r, \theta, \varphi) = \psi_{J_z}(r, \theta, \varphi + 2\pi/p) = e^{i\frac{2\pi J_z}{p}}\psi_{J_z}(r,\theta,\varphi),$$

where ℓ_i is the orbital angular momentum quantum number of the ith electron in the configuration of interest. Substituting Eq. (6) into Eq. (7) allows the J_z states to be separated into classes of states having a common phase factor specified by μ which depends on whether the configuration has even parity (i.e., $\sum_i \ell_i$ even) or odd parity (i.e., $\sum_i \ell_i$ odd). If the configuration is even, Eq. (5) is obtained. If the configuration is odd, as it is for Nd, then we find for the S_p operation,

$$\mu = J_z \pm \frac{p}{2} + \xi p .$$

Since ξ is a running index which can have either sign and has no physical significance of its own, the two sign choices in the above expression gives the same result for a given $|J_z|_{max} = J$ value. Therefore, we chose to use

$$J_z = (\mu + \frac{p}{2}) \pmod{p} \ . \tag{8}$$

The tables of Koster et al. [17] show that in D_2 symmetry, crystal-field levels arising from a J state of the $4f^3$ configuration of Nd are of only one irreducible representation (rep) namely Γ_5 with $\mu = \pm\frac{1}{2}$ (i.e., doubly degenerate). Whereas, in D_{2d} symmetry, two doubly degenerate reps are possible, namely Γ_6 with $\mu = \pm1/2$ and Γ_7 with $\mu = \pm3/2$. The J_z values permitted in the Γ_5 crystal-field rep of the D_2 symmetry using Eq. (5) with p = 2 are as follows:

For $\mu = +1/2$, $\xi = 0, 1, -1, 2, -2, 3, -3, \ldots,$

$J_z = 1/2, 5/2, -3/2, 9/2, -7/2, 13/2, -11/2, \ldots,$

and for $\mu = -1/2$, $\xi = 0, 1, -1, 2, -2, 3, -3, \ldots,$

$J_z = -1/2, +3/2, -5/2, +7/2, -9/2, 11/2, -13/2, \ldots$

Likewise for the Γ_7 and Γ_6 reps of D_{2d} symmetry, we obtain the following values for Nd from Eq. (8) with p = 4.

For $\mu = -3/2$, $\xi = 0, 1, -1, 2, -2, \ldots,$

$J_z = 1/2, 9/2, -7/2, 17/2, -15/2, \ldots,$

$\mu = +3/2$, $\xi = 0, 1, -1, -2, -3, \ldots,$

$J_z = 7/2, 15/2, -1/2, -9/2, -17/2, \ldots,$

$\mu = -1/2$, $\xi = 0, 1, -1, 2, -2, \ldots,$

$J_z = 3/2, 11/2, -5/2, 19/2, -13/2, \ldots,$

and for $\mu = +1/2$, $\xi = 0, 1, -1, -2, -3, \ldots,$

$J_z = 5/2, 13/2, -3/2, -11/2, -19/2, \ldots.$

In D_2 symmetry, the free-ion states split as follows [17, 18]:

$^2P_{1/2} \rightarrow \Gamma_5$

$^4F_{3/2} \rightarrow 2\Gamma_5$,

$^4I_{9/2} \rightarrow 5\Gamma_5$,

$^4I_{11/2} \rightarrow 6\Gamma_5$.

In D_{2d} symmetry, for $4f^3$, an odd-parity configuration, we find

$$^2P_{1/2} \rightarrow \Gamma_7 \, ,$$

$$^4F_{3/2} \rightarrow \Gamma_6 + \Gamma_7 \, ,$$

$$^4I_{9/2} \rightarrow 2\Gamma_6 + 3\Gamma_7 \, ,$$

$$^4I_{11/2} \rightarrow 3\Gamma_6 + 3\Gamma_7 \, .$$

We note that in even-parity configurations, Γ_6 and Γ_7 exchange places in the above list. Thus, in YAG, the two crystal-field levels belonging to the $^4F_{3/2}$ state <u>each</u> can have a J_z composition consisting of a mixture of $J_z = \pm 1/2$ and $\pm 3/2$. On the other hand, in

$$\Gamma_6(\mu = \pm 1/2), \text{ pure } J_z = \mp 3/2,$$

and

$$\Gamma_7(\mu = \pm 3/2), \text{ pure } J_z = \mp 1/2.$$

Similarly, in Nd:YAG

for $^4I_{9/2}$, $\Gamma_5 (\mu = \pm 1/2)$, mixed $J_z = \pm1/2, \mp3/2, \pm5/2, \mp7/2, \pm9/2,$

and for $^4I_{11/2}$, $\Gamma_5(\mu = \pm1/2)$, mixed $J_z = \pm1/2, \mp3/2, \pm5/2, \mp7/2, \pm9/2, \mp11/2.$

Whereas, in Nd:YVO$_4$

for $^4I_{9/2}$, $\Gamma_6(\mu = \pm1/2)$, mixed $J_z = \mp3/2, \pm5/2,$

$\Gamma_7(\mu = \pm3/2)$, mixed $J_z = \mp1/2, \pm7/2, \mp9/2,$

and for $^4I_{11/2}$, $\Gamma_6(\mu = \pm1/2)$, mixed $J_z = \mp3/2, \pm5/2, \mp11/2,$

$\Gamma_7(\mu = \pm3/2)$, mixed $J_z = \mp1/2, \pm7/2, \mp9/2.$

It should be noted that from Eq. (4), the J_z values permitted in a given state cannot be changed by J mixing unless the symmetry is changed.

The differences between these two symmetries are significant when considering Eq. (2). In D_2 symmetry, the non-zero A^k_q parameters occur for all possible odd values of k with $|q| = 2, 4, 6$ and $|q| < k$. However, in D_{2d} symmetry, only $A^3_{\pm 2}$, $A^5_{\pm 2}$, $A^7_{\pm 2}$, and $A^7_{\pm 6}$ are non-zero, in general. The two 3-j symbols that appear in Eqs. (2) and (3) govern which parameters A^k_q are active in a given transition. Thus, for the $^4I_{9/2} \longleftrightarrow {}^4F_{3/2}$ transitions, t = 4, 6 and k = 3, 5, 7. Since all permitted values of q can occur in D_2 symmetry, then from the rule on the bottom row of the 3-j symbol in Eq. (3), namely

$$J_z = J'_z + \rho + q, \tag{9}$$

it is clear that all transitions are permitted in both π and σ polarizations. This is really trivial because with only one crystal field state, viz. Γ_5, this must follow logically.

In D_{2d} symmetry, since $q = \pm 2, \pm 6$ then we have from Eq. (9) that

$$J_z = J'_z + \rho \pm 2, \text{ and } J_z = J'_z + \rho \pm 6.$$

Using this relation, Table 4 is obtained for the $^4I_{9/2} \leftrightarrow {}^4F_{3/2}$ transitions.

The significant fact obtained from Table 4 is that the transitions which couple to the Γ_7 crystal levels of the $^4I_{9/2}$ state depend on the contributions to Eq. (2) of the $A^3_{\pm 2}$, $A^5_{\pm 2}$, $A^7_{\pm 2}$ terms relative to that of $A^7_{\pm 6}$. Thus, if one of the Γ_7 levels in that state had pure or nearly pure $|J_z| = 9/2$ composition and the $A^7_{\pm 6}$ term was dominant, then the π transition with the Γ_6 state and the σ transition with the Γ_7 state would be expected to be stronger than the σ transition with the Γ_6 state. Also, a transition with a given level having $|J_z| = 3/2$, 5/2 composition (i.e., Γ_6) would be comparatively weak if not completely missing. On the other hand, if q was restricted to ± 2 due to the smallness $A^7_{\pm 6}$, then

Table 4. Transitions permitted by the 3-j symbol in Eq. (3) for the $^4I_{9/2} \leftrightarrow {}^4F_{3/2}$ transitions of Nd^{3+} in D_{2d} symmetry. [a]

ρ	J'_z	J_z	
		$q = \pm 2$	$q = \pm 6$
π $\begin{cases} 0 \\ 0 \end{cases}$	$\left.\begin{array}{c} +1/2 \\ -1/2 \end{array}\right\} (\Gamma_7)$	$+5/2, \ -3/2$ $-5/2, \ +3/2$	$\left.\begin{array}{c} - \ - \\ - \ - \end{array}\right\} (\Gamma_6)$
σ $\begin{cases} +1 \\ +1 \\ -1 \\ -1 \end{cases}$	$+1/2$ $-1/2$ $+1/2$ $-1/2$	$+7/2, \ -1/2$ $+5/2, \ -3/2$ $+3/2, \ -5/2$ $+1/2, \ -7/2$	$-9/2 \quad (\Gamma_7)$ $- \ - \quad (\Gamma_6)$ $- \ - \quad (\Gamma_6)$ $+9/2 \quad (\Gamma_7)$
π $\begin{cases} 0 \\ 0 \end{cases}$	$\left.\begin{array}{c} +3/2 \\ -3/2 \end{array}\right\} (\Gamma_6)$	$+7/2, \ -1/2$ $+1/2, \ -7/2$	$\left.\begin{array}{c} -9/2 \\ +9/2 \end{array}\right\} (\Gamma_7)$
σ $\begin{cases} +1 \\ +1 \\ -1 \\ -1 \end{cases}$	$+3/2$ $-3/2$ $+3/2$ $-3/2$	$+9/2, \ +1/2$ $+3/2, \ -5/2$ $+5/2, \ -3/2$ $-1/2, \ -9/2$	$-7/2 \quad (\Gamma_7)$ $- \ - \quad (\Gamma_6)$ $- \ - \quad (\Gamma_6)$ $+7/2 \quad (\Gamma_7)$

a. See text.

58

Γ_7 ($|J_z| = 9/2$) $\overset{\pi}{\to} \Gamma_6$ and $\overset{\sigma}{\to} \Gamma_7$

would not be observed or would be very weak.

Applying the above analysis to the $^4F_{3/2} \longleftrightarrow {}^4I_{9/2}$ transitions, we would expect to find 10 lines in the Nd:YAG spectrum which is the case [17]. However, from Table 4, we have sufficient reason to expect lines to be missing from the spectrum of Nd:YVO$_4$. The symmetry allowed transitions in the host are found from Eq. (8), where $\mu - \mu' \equiv \Delta\mu = \Delta J_z \pmod 4$, which becomes, from Eq. (9),

$$\Delta\mu = (\rho + q) \bmod 4, \quad q = \pm 2, \pm 6. \tag{10}$$

The selection rules which result from Eq. (10) are $\Delta\mu = \pm 2$ for π polarization and $\Delta\mu$ ($\rho = \pm 1$) $= \mp 1, \pm 3$ for σ polarization and are summarized in Table 5. Applying these rules to the transitions in question indicates we should observe 10 lines in σ polarization and 5 lines in π polarization. The low temperature fluorescence spectrum given in Figure 25 shows only 8σ lines and 3π lines with one π line very strong supporting the implications derived from Table 4.

3. The $^2P_{1/2}$ State in D$_{2d}$ Symmetry

The 2-fold degeneracy of the $^2P_{1/2}$ state, being of magnetic origin (i.e., spin) cannot be split by a crystal field. Furthermore, the spin selection rule $\Delta S = 0$ forbids transitions between the $^4I_{9/2}$ ground state and a doublet. However, Rajnak [19] has shown that the "free-ion" eigenvector for the energy level associated with the $^2P_{1/2}$ state contains a significant admixture of the $^4D_{1/2}$ state which will accept transitions from the ground manifold. Thus, by observing these transitions, it should be possible to unambiguously locate and identify the levels in the ground manifold. From Table 5, there can be 5 σ lines and only 2 π lines between 2Γ_6 + 3Γ_7 levels

59

Table 5.   Electric dipole selection rules
            in D_{2d} Symmetry[a]

	$\Gamma_6(1/2)$	$\Gamma_7(3/2)$
$\Gamma_6(1/2)$	σ	π σ
$\Gamma_7(3/2)$	π σ	σ

a. The quantities in parentheses are the
    crystal field quantum numbers $|\mu|$.

and one Γ_7 level. Figure 23 shows 2 π lines but only 3 σ lines. This clearly fixes the two Γ_6 levels in the ground manifold and implies that the ground state is Γ_7. The missing σ lines can be assumed to be due, at least in part, to the details of the J_z compositions of the levels associated with the missing lines.

E. Energy Level Scheme

The spectra in Figures 23-25 show that one of the $^4I_{9/2} \overset{\pi}{\to} {}^2P_{1/2}$ transitions originates from a level that also couples to one of the $^4F_{3/2}$ levels in π polarization. This means that choosing the label Γ_7 for the $^2P_{1/2}$ level must, if we follow Table 5, fix the order of levels in the $^4F_{3/2}$ state to be Γ_7 ($\mu = \pm 3/2$) high and Γ_6 ($\mu = \pm 1/2$) low in energy. Since the ground state couples to the lower level in π polarization, then the ground state must be Γ_7 as found in Section D. 3. above. From EPR studies of Nd:YVO$_4$, Ranon [20] reported that the ground state could only be fitted to a linear combination of the $|J_z|$ values 1/2, 7/2, and 9/2. From Table 4, this corresponds to a Γ_7 level consistent with our findings.

As previously suggested [12], because of the similarity between the crystal-field expansions for CaWO$_4$ and YVO$_4$, the direction of the $^4F_{3/2}$ splitting in the two hosts should be consistent with the sign A^2_0. This comes from Eq. (4) which, for $J' = J = 3/2$, only k = 2 gives a non-zero value. The sign of the A^2_0 parameter can easily be found from

$$A^2_{\,0} = \sum_j [e^2 Q_j / r_j^{\,3}] (3z_j^{\,2} - r_j^{\,2}) / r_j^{\,2}$$

where e is the electronic charge, $-eQ_j$ is the charge of the jth ion, r_j is the radial separation between the site center and the jth ion where z_j is the corresponding z component, and the summation is taken over all the ions surrounding the site. If all the ions or groups of ions of the same kind are located at the corners of regular tetrahedra having a common center at

which the Nd ion is located, then $z_j = \pm r_j /\!/\sqrt{3}$ and $A_0^2 = 0$. In D_{2d} symmetry, as described in Section D.1., the tetrahedra are shorter in the z direction than in the x and y directions. Therefore, $z_j^2 < r_j^2/3$ and since the net charges of the surrounding ions are negative, $A_0^2 < 0$ as was reported for Eu^{3+} in YVO_4 [21] and for Nd:YVO_4 [10, 12]. The sign of A_0^2 in $CaWO_4$ has been reported to be positive [22] with the $\mu = \pm 3/2$ level split down consistent with our results for YVO_4.

Having established the ordering of the states in the $^4F_{3/2}$ manifold as described above, the identity of the four observed transitions in the $^4F_{3/2} \xrightarrow{\pi} {}^4I_{11/2}$ spectrum can be established. In the discussion concerning the anomolous appearance of two of the strong σ lines in the π spectrum, we concluded that there is a fifth π line in the long wavelength wing of the strong π line. This is sufficient to complete the specification of the 6 levels to be alternating Γ_6 and Γ_7 with the lowest level of the $^4I_{11/2}$ manifold being Γ_7.

The energy level scheme based on the above deductions is given in Figure 28 for room temperature. Also shown are the observed transitions. The experimental frequencies of these transitions taken at room temperature and $\sim 85^\circ K$ are presented in Table 6. The line widths and peak cross sections of the $^4F_{3/2} \xrightarrow{\pi\sigma} {}^4I_{11/2}$ transitions at room temperature were also measured. These results are given in Table 7. The strengths were determined by comparing the fluorescence intensities to the intensity of the $^4I_{9/2}(e) \rightarrow {}^4F_{3/2}(b)$ resonance line. The laser transition $^4F_{3/2}(a) \rightarrow {}^4I_{11/2}(a)$ is at $10,640.9 \pm 0.2$ Å and is predominantly π polarized. It was found to have a peak cross section of 4.6 times greater than that of the 1.064 μm laser transition in Nd:YAG which has been found to be 6.5×10^{-19} cm^2 [9].

62
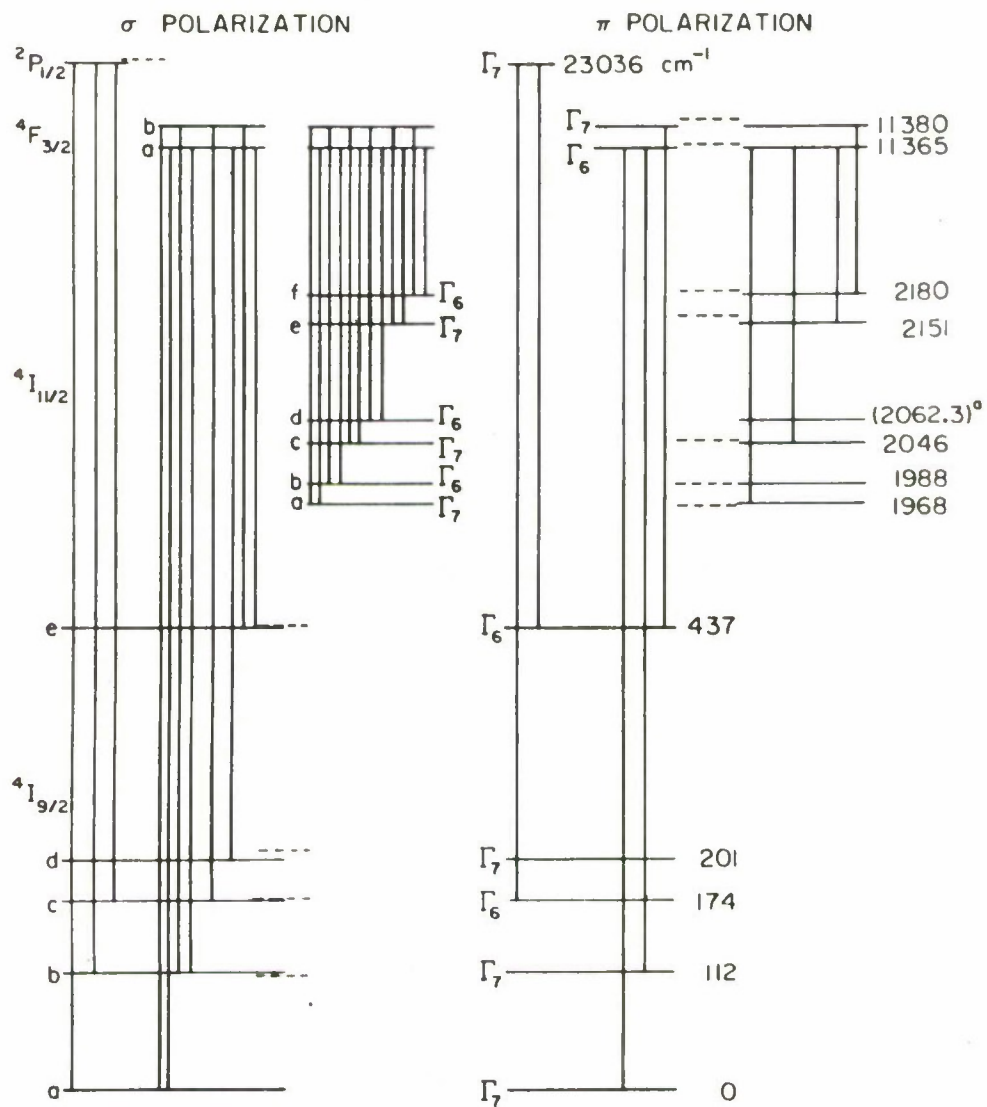
Figure 28. Energy levels ($\pm$ 1 cm^{-1}) of selected states of Nd:YVO$_4$ at room temperature showing transitions resolved at ~85°K. The approximate positions of the levels at ~85°K are shown as short dashed lines. (a) This is the ~85°K value. See Table 6.

Table 6. Observed Transitions of ~1 Atomic % Nd^{3+} in YVO_4.[a]

Transition	Polarization[b]	ν_{air} (cm^{-1})	
		~85°K	~300°K
$^4I_{9/2} \rightarrow {}^2P_{1/2}$			
a - a	σ	23 040.4	23 036.3
b - a	σ	22 928.9	22 922
c - a	σ, π	22 866.1	22 863
d - a	-	n/o	n/o
e - a	π	n/o	22 600
$^4F_{3/2} \leftrightarrow {}^4I_{9/2}$			
a - a	σ, π	11 368.1	11 365.4
a - b	σ, π	11 258.6	11 253.2
a - c	-	n/o	n/o
a - d	σ	11 158.2	~11 164
a - e	σ	10 931	10 929[c]
b - a	σ, (π)	11 386.1	11 379.6
b - b	σ	11 276.4	11 267[c]
b - c	σ	11 211.2	11 205.5
b - d	-	n/o	n/o
b - e	σ, π	10 948	10 943
$^4F_{3/2} \rightarrow {}^4I_{11/2}$			
a - a	σ, π	9 400.9	9 397.7
a - b	σ, (π)	9 379.9	9 377.5
a - c	σ, π	9 320.8	9 319.1
a - d	σ	9 306.2	n/o
a - e	σ, π	9 213.5	9 214.8
a - f	σ	9 186.7	9 185.9[c]
b - a	σ, (π)	9 418.6	9 411.9
b - b	σ, π[d]	9 397.7	9 391.6[c]
b - c	σ	9 338.2	9 333.7
b - d	σ, π[d]	9 323.5	n/o
b - e	σ	9 230.6	9 228.8
b - f	σ, π	9 203.8	9 200.0

Values given to 0.1 cm^{-1} are accurate to ± 0.5 cm^{-1} or better.
All other values are to ± 1 cm^{-1}.

a. See Figures 1 - 4 for traces of spectra. n/o means "not observed."
b. The σ transitions which appear weakly in π polarization are denoted by (π).
c. These values had to be deduced from other values because of interference from neighboring lines.
d. This polarization was not resolved. See text.

Table 7. Parameters for $^4F_{3/2} \to {}^4I_{11/2}$ Transitions of Nd:YVO$_4$ at Room Temperature.[a]

| Transition | Frequency[b] (cm^{-1}) | Linewidth[c] (cm^{-1}) | Peak Cross-section (x 10^{-19} cm^2)[c] | | |
| | | | Along c-axis | Along a-axis | |
				σ	π
b→a	9411.9	7.8	13	7.0	--[d]
a→a	9397.7	6.9	~12	~6.4	30
b→b	9391.6	6.5	~9	~4.9	--[d]
a→b	9377.5	7.7	17	9.4	--[d]
b→c	9333.7	12.8	2.4	1.6	n/o
a→c	9319.1	9.7	weak	weak	3.0
b→d	(9323.5)	--	n/o	n/o	n/o
a→d	(9306.2)	--	n/o	n/o	n/o
b→e	9228.8	11.6	7.2	4.2	n/o
a→e	9214.8	9.1	weak	weak	3.0
b→f	9200.0	15.2	6.6	2.0	weak
a→f	9185.9	--	weak	weak	n/o

a. See Figure 26 for traces of spectra. n/o means not observed. See Table 6.

b. Frequencies in parentheses are ~85°K values.

c. These data were obtained from a Dess-Bolin sample (see text and Ref. 5) having a Nd weight percentage of 0.91%. Cross section values to ±20%.

d. These lines are too obscured by a → a line for measurement. See text.

65

Comparing the spectra given in Figures 25 and 26 with Figure 28 and Table 7, we note that the two strongest fluorescence lines are the $a \xrightarrow{\pi} a$ transitions with the corresponding $b \rightarrow a$ transitions among the strongest in the σ spectra. As mentioned in Section D.2., this is the behavior predicted from Table 4 for the transitions to a Γ_7 state having a large $|J_z| = 9/2$ composition where the $A^7_{\pm 6}$ parameter is dominant. Although this is the only case in Table 4 that could clearly produce one strong line while discriminating against the remaining lines in π polarization, other possibilities may exist. It is sufficient to recognize that Table 4 predicts the possibility.

It is interesting in this regard to compare YVO_4 to $CaWO_4$. The Nd site symmetry in the latter is the S_4 group. The only difference in the formal expansion of the crystal-field potential compared to YVO_4 is that the terms having $|q| > 0$ are, in general, complex [23]. Yet the spectrum of Nd:$CaWO_4$ [24] does not show a large concentration of the available oscillator strength into one transition as is observed in Nd:YVO_4. Since Table 4 is applicable to $CaWO_4$ except for the rep labels (see Reference 17), we conclude that something akin to the $A^k_{\pm 2}$ (k odd) being competitive with $A^7_{\pm 6}$ is the cause for this difference between the two hosts. In other words, the odd-parity portion of the crystal field is concentrated in the high-order terms in YVO_4 while in $CaWO_4$, it is either in the low-order terms or distributed over all the terms. This difference appears to be reflected in the even-parity terms. The ratio B^6_0/B^2_0 for Nd in $CaWO_4$ is -0.031 [22] while in YVO_4 it is 8.6 [12]. (Note that $B^k_q \equiv \langle r^k \rangle A^k_q$, where $\langle r^k \rangle$ are the usual radial integrals.)

It can be shown that the odd-parity A^k_q are quite sensitive to ion placements and to slight deviations from the normal site symmetry. The difference between YVO_4 and other hosts may be a result of this sensitivity. A case that illustrates the dependence of line strengths on the ion placements is the behavior of the $^8S \rightarrow {}^6I$ transitions of Gd^{3+} in BaF_2 [25]. These

66

transitions are magnetic dipole forbidden but are observed in CaF_2 and SrF_2 as electric dipole transitions via intermediate coupling [26, 27] and the A^5_q and A^7_q parameters. However, they are absent in BaF_2 at low Gd^{3+} concentrations, say $\lesssim 0.1$ atomic %. As the concentration is increased, these transitions suddenly turn on at around 0.2 atomic % and grow very rapidly. It was determined that this effect was due to the minute change in the lattice parameter introduced by substituting the smaller Gd^{3+} ion (1.02 Å) for the Ba^{2+} ion (1.35Å). In simple terms, this small change in lattice dimension produced large changes in the above odd parity terms while the crystal field splittings changed by < 1 cm^{-1}.

There is the question of the missing transitions in Figure 28 that are allowed by the selection rules. This is most evident in transitions with the c and d levels of the $^4I_{9/2}$ manifold and with the d and e levels of the $^4I_{11/2}$ manifold. Regarding the former and referring to the low temperature σ spectrum in Figure 25, we see that one of the transitions a → d or b → d is missing. Since d is a Γ_7 as are levels a and b, then from Table 4 assuming $A^7_{\pm 6}$ is dominant we see that unless d has some $|J_z| = 9/2$ content, it will not be observed in π polarization. It will be observed in σ polarization via its $|J_z| = 7/2$ content but only to a Γ_6 level. Thus, we are led to identify the observed transition to be a → d. This choice is contrary to that reported in previous studies [9, 10, 12], but is consistent with the absence of the $^4I_{9/2}(d) \xrightarrow{\sigma} {}^2P_{1/2}$ transition.

There is no ambiguity in the assignment of the transitions with level $^4I_{9/2}(c)$ because of the observed transition to the $^2P_{1/2}$ level. The corresponding line in the Figure-25 σ spectrum is the b → c transition. This line, being anomolously wider than either of its neighbors, is sufficient to include a weak a → c line in the high wavelength wing. Regarding this width, there have been two Raman modes in YVO_4 reported at 157 and 162 cm^{-1} of symmetry $B_{1g}(\Gamma_3)$ and $E_g(\Gamma_5)$, respectively [28]. Both of

these modes will couple the Γ_6 and Γ_7 states [27] (i.e., levels c and a) which suggests that level c is broadened by a strong coupling with the lattice.

The distribution of oscillator strength in the $^4F_{3/2} \rightarrow {}^4I_{11/2}$ transitions can be understood by extending Table 4 to include $J_z = \pm 11/2$. Again, if the $A^7_{\pm 6}$ parameter dominates the induced dipole moment, then only those Γ_7 levels containing a large admixture of $J_z = \pm 7/2, \mp 9/2$ and those Γ_6 levels containing $J_z = \pm 11/2$ will have strong transitions terminating on them. Saying it another way, those levels having little or none of these J_z values will have little or no coupling with the $^4F_{3/2}$ levels.

Regarding the absence of the $^4I_{9/2}(e) \xrightarrow{\sigma} {}^2P_{1/2}$ transition, it is reasonable to assign this to the Boltzmann depopulation of the level e plus an oscillator strength smaller than the corresponding π transition.

F. Summary

A reasonably unambiguous determination of the positions of the crystal-field levels of the $^4I_{9/2}$, $^4I_{11/2}$, $^4F_{3/2}$, and $^4P_{1/2}$ J manifolds of Nd in YVO_4 has been made. The proposed energy level scheme is consistent with the observed polarized spectra. The ground state was determined to be $\Gamma_7(\mu = \pm 3/2)$ with a J_z composition of $\mp 1/2$, $\pm 7/2$, and $\mp 9/2$ consistent with previous studies [12, 20]. An analysis of the implications of the Judd-Ofelt theory [13] regarding the transitions between the crystal-field levels showed that (1) lines can be missing, and (2) it is possible for a π transition to have a relatively high oscillator strength in the spectra of Nd in D_{2d} or a similar symmetry. It was found that the unusual disparity of strengths of the strong lines relative to the remaining lines, particularly in the π spectra, could be qualitatively understood if the contribution of the $A^7_{\pm 6}$ parameter to the induced electric dipole moments is significantly greater than the contributions from the $A^k_{\pm 2}$ (k = 3, 5, 7) parameters. This suggests that it would be of value to compare detailed crystal-field and line-strength calculations performed for various host crystals in order that the difference between YVO_4 and other laser hosts can be more clearly understood.

IV. SURVEY OF Nd:YVO$_4$ ABSORPTION

The Cary 17 Dual Beam Spectrophotometer was used to measure the absorption spectrum of Nd:YVO$_4$ from 0.38 to 2.0 μm. The lower limit was determined by the material's uv absorption edge and the upper limit by the instrument. Several bands of interest were probed. There are at ~1.6, 0.89, 0.81, 0.75, 0.59, 0.53, 0.48 and 0.44 μm. The observed lines are tabulated in Table 8. Copies of the data for these bands obtained with a 1% Nd:YVO$_4$ sample, 4 mm thick, are included for both σ and π polarized light in Figures 29-44.

The most intense absorption line in the ~0.81 μm band is the 0.8080 μm line for π polarized light. Its absorptivity is ~8.6 cm^{-1}. The 0.8078 μm line for σ polarized light is also strong having an absorptivity of ~4.2 cm^{-1}. Since these lines are part of a strong pump band, it is therefore recommended that diodes for laser excitation of Nd in YVO$_4$ be tuned for 0.8080 μm and have sufficient line width to also pump at 0.8078 μm.

The "yellow" absorption band (at ~0.59 μm) is the most intense absorption band in the Nd:YVO$_4$ spectrum. In π polarized light the line at 0.5940 μm has an absorptivity of ~15.3 cm^{-1}. There are several other very intense lines in this group for both σ and π polarized light. Since dye lasers in this spectral region are available, laser excitation using these lines should be possible.

It should be noted that pumping at the most intense absorption wavelengths will result in very high thermal loading to a very small volume of material. This may result in pump induced catastrophic or non-catastrophic material failure. In addition, the pumped volume will be restricted to the region near the entrance surface and so any lasing which occurs will be similar to that produced by a surface laser. It is suggested therefore that dye laser pumping studies be conducted for a variety of wavelengths in the "yellow" band so that the optimum combination of absorptivity,

excited lasing volume and thermal loading can be found.

In the cw laser experiments we pumped with the 0.5145 μm laser line from an argon ion laser. The nearest absorption line for this pump source is the 0.5143 μm line for σ polarized light. Even though it presents a good wavelength match to the pump line, this line is relatively weak. Its absorptivity is only ~ 0.4 cm^{-1}. The absorption at 0.5145 μm for π polarized light is in the edge of the 0.5118 μm line and has an absorptivity of ~ 0.4 cm^{-1}.

The π and σ absorption spectra of a 3%, 8.5 mm thick, Nd:YVO$_4$ crystal in the 0.89 μm band are included in this report. These should be compared with the same spectra for the 1% Nd:YVO$_4$ sample. It is clear that the line shapes and position do not change with concentration. In addition, for all absorption wavelengths in the 0.7-0.95 μm range, the absorption strengths were found to scale with the Nd concentration.

As a result of our spectral measurements at 1.6 μm we have shown the Cary 17 Spectrophotometer to be partially linearly polarized. In particular, it appears to be partially polarized in the horizontal plane. Its optical system is essentially the same as that of the Cary 14 and so we suggest that data taken with such instruments be scrutinized for this effect. To insure the linear polarization necessary for separation of the σ and π spectra of the shorter wavelength absorption bands, calcite-Glan polarizers were inserted in both the sample and reference beams of the instrument.

Table 8. Absorption Lines of Nd:YVO_4 at Room Temperature Nominally 1% Nd

Classification	σ Polarization		π Polarization	
	λ (μm)	α (cm^{-1})	λ (μm)	α (cm^{-1})
$^4F_{9/2} \rightarrow {}^4I_{13/2}$	2.564		2.535	
	2.538		2.518	strongest
	2.480		2.483	
	2.455		2.455	
	2.408	strongest	2.408	
$^4I_{9/2} \rightarrow {}^4I_{15/2}$	1.766	0.018	1.766	0.081
	1.747	0.064	1.748	0.012
	0.738	0.055	1.713	0.035
	1.713	0.166	1.705	0.035
	1.706	0.129	1.691	0.042
	0.667	0.023	1.675	0.035
	1.638	0.046	1.650	0.115
	1.627	0.037	1.627	0.075
	1.598	0.055	1.598	0.449
	1.583	0.216	1.583	0.081
			1.302	0.063
			1.288	0.046
$^4I_{9/2} \rightarrow {}^4F_{3/2}$	0.9138	0.253	0.9132	0.293
	0.9030	0.127	0.901	0.144
	0.8913	0.753	0.8877	0.805
	0.8868	0.886	0.8794	4.899
	0.8785	1.500	0.8675	0.293
	0.8687	0.196	0.8577	0.219
	0.8350	0.661	0.8351	0.288
	0.8158	2.645	0.8180	1.323
	0.8078	4.169	0.8080	8.596
	0.7883	0.270	0.790	0.230
	0.7754	0.230	0.7745	0.633
	0.7666	0.587	0.7562	3.726
	0.7530	4.255	0.7505	4.428
	0.7435	1.783	0.7440	2.358
	0.6347	0.075	0.6302	0.029
	0.6308	0.144	0.6260	0.173
	0.6262	0.058	0.610	0.219
	0.6101	2.358	0.6045	1.610
	0.6048	1.541	0.6015	3.996
	0.6010	2.128	0.5982	14.346

Table 8.   (Continued)

Classification	σ Polarization		π Polarization	
	λ (μm)	α (cm^{-1})	λ (μm)	α (cm^{-1})
	0.5981	6.986	0.5957	14.470
	0.5957	7.744	0.5940	15.266
	0.5938	8.424	0.5890	5.520
	0.5892	10.810	0.5866	5.923
	0.5870	4.313	0.5832	6.383
	0.5853	3.565	0.5795	1.265
	0.5795	5.750	0.5770	0.661
	0.5755	0.431	0.573	0.316
	0.5735	0.259	0.570	0.259
	0.5715	0.173	0.566	0.219
	0.5680	0.144	0.563	0.219
	0.5661	0.127	0.560	0.219
	0.5630	0.115		
	0.5600	0.115		
	0.5555	0.086		
	0.5525	0.058		
	0.5510	0.058		
	0.5452	0.086	0.5523	0.173
	0.5437	0.104	0.5433	0.863
	0.5408	0.288	0.5408	2.444
	0.5382	0.977	0.5382	0.058
	0.5362	1.484	0.5358	0.058
	0.5380	0.391	0.5333	0.661
	0.5362	0.903	0.5301	1.524
	0.5325	3.939	0.5285	0.288
	0.5285	1.926	0.5245	0.604
	0.5250	0.010	0.5222	1.265
	0.5223	1.236	0.5200	2.128
	0.5202	0.288	0.5170	1.254
	0.5178	0.201	0.5118	1.495
	0.516	0.173	0.5095	0.920
	0.5143	0.403	0.5070	0.345
	0.511	0.288	0.5050	0.086
	0.5097	0.431		
	0.5070	0.288		
	0.4912	0.029*	0.4970	0.029*
	0.4855	0.086	0.4912	0.069
	0.4838	0.219	0.4885	0.012
	0.4820	0.230	0.4850	0.259
	0.4790	0.184	0.4819	0.805
	0.4760	0.288	0.4790	0.144

Table 8. (Continued)

Classification	σ Polarization		π Polarization	
	$\lambda\,(\mu m)$	$\alpha\,(cm^{-1})$	$\lambda\,(\mu m)$	$\alpha\,(cm^{-1})$
	0.4735	0.115	0.4759	2.156
	0.4710	0.132	0.4713	0.633
	0.468	0.173	0.4670	0.328
	0.465	0.219	0.4625	0.230
	0.4632	0.276	0.4420	0.098
	0.4372	0.173	0.4371	1.064
	0.4360	0.086	0.4340	0.058
	0.4340	0.943	0.4250	0.069
	0.4235	0.058	0.4235	0.155

* The absorptivity for all lines at wavelengths <5000 Å has been corrected for the broad color center band absorption evident in Figures 43 and 44.
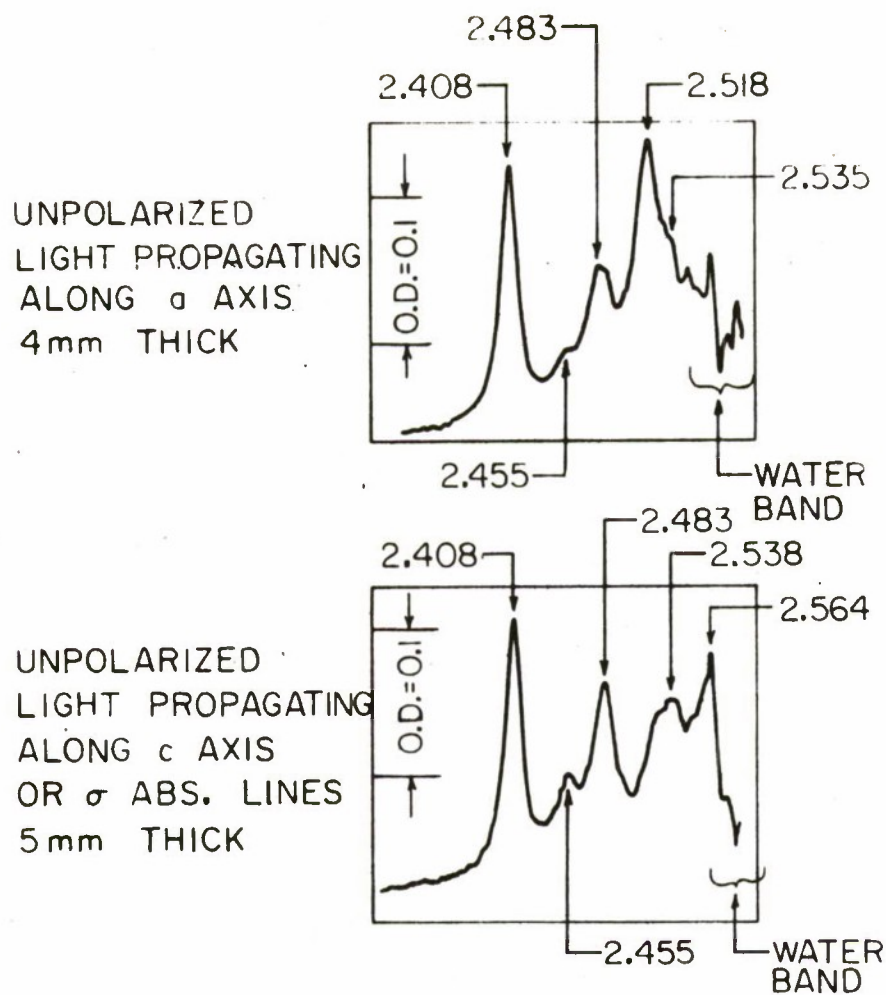
Figure 29. 2.5 μm Band of Nd:YVO$_4$ Absorption Spectra at Room Temperature. Taken with Beckman DK-2A Spectrophotometer. 1% Nd. 4 mm thick.

74
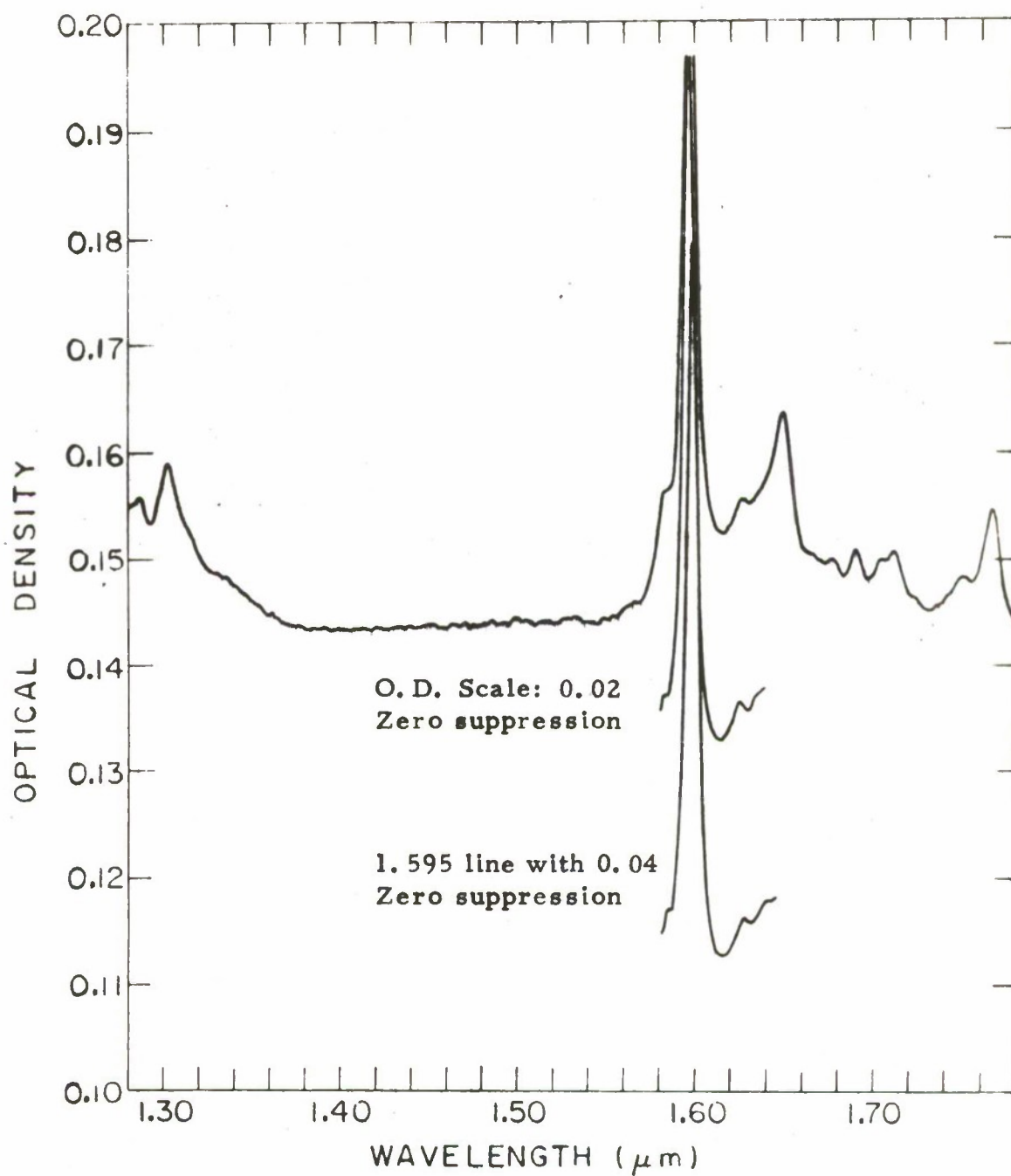
Figure 30. 1.6 μm Band of Nd:YVO$_4$ Absorption Spectra at Room
Temperature. Partially polarized light propagating along
the a-axis. Mostly π spectrum. 1% Nd. 4 mm thick.
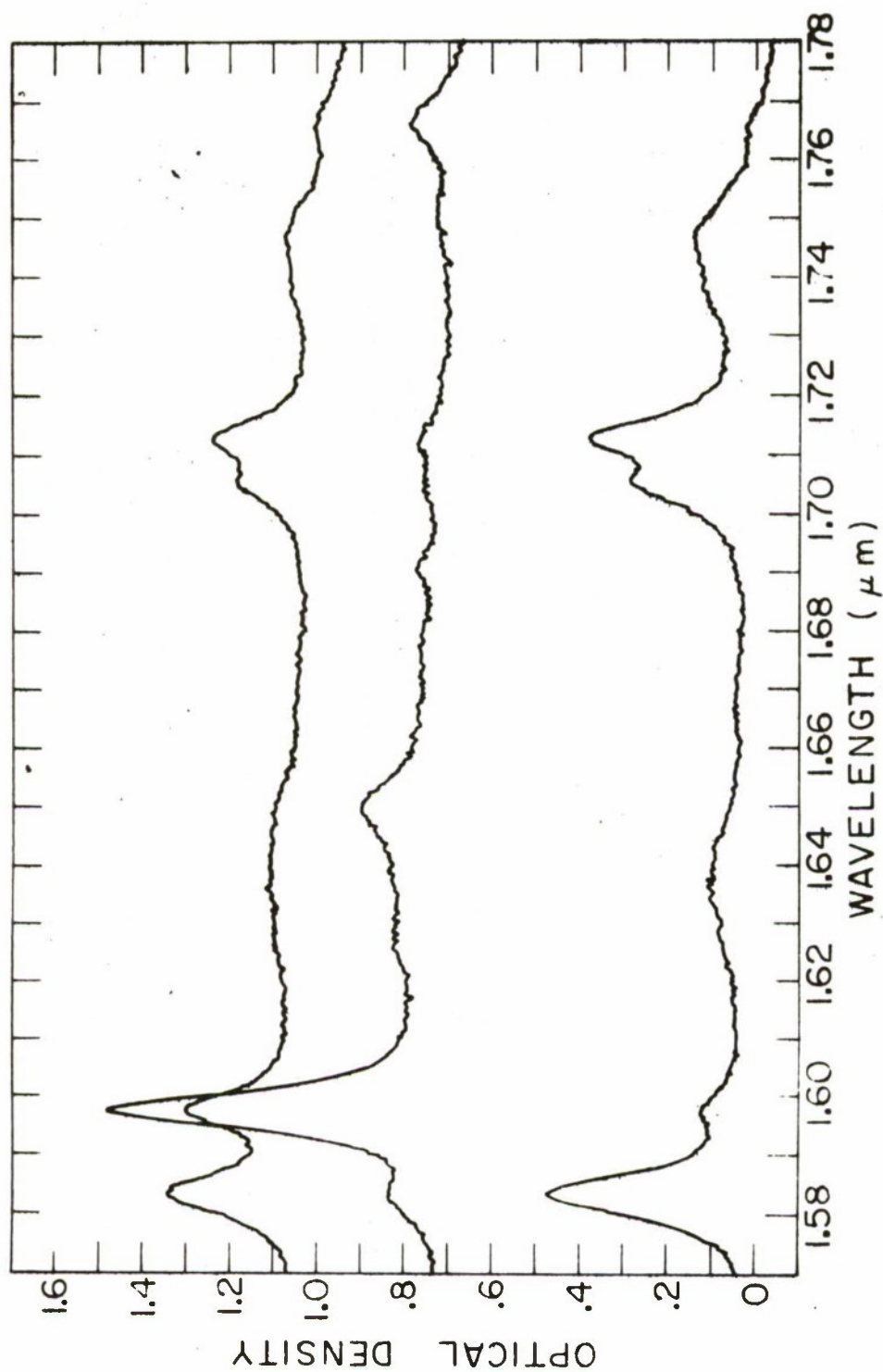
Figure 31. 1.6 μm Band of Nd:YVO$_4$ Absorption Spectra at Room Temperature. Lower curve is σ spectrum. Propagation along c-axis. 1% Nd. 5 mm thick. Upper curves demonstrate the fact that the Cary 17 Spectrophotometer is partially linearly polarized. Propagation along a-axis. 1% Nd. 4 mm thick.
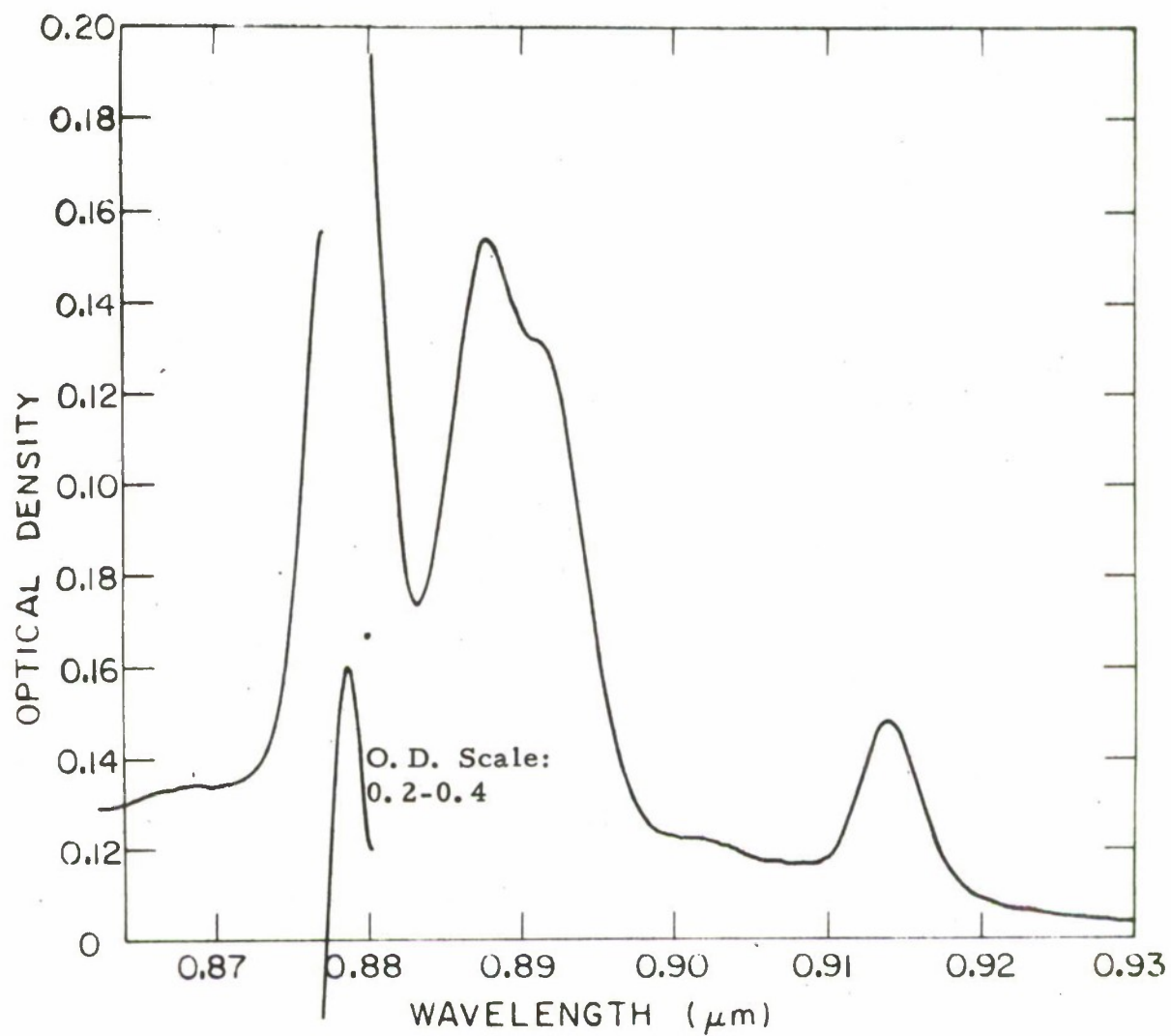
Figure 32.   0.89 μm Band of Nd:YVO$_4$ Absorption Spectra at Room
Temperature.   σ spectrum.   1% Nd.   4 mm thick.

Figure 33.   0.89 μm Band of Nd:YVO$_4$ Absorption Spectra at Room
Temperature.   σ spectrum.   3% Nd.   8.5 mm thick.
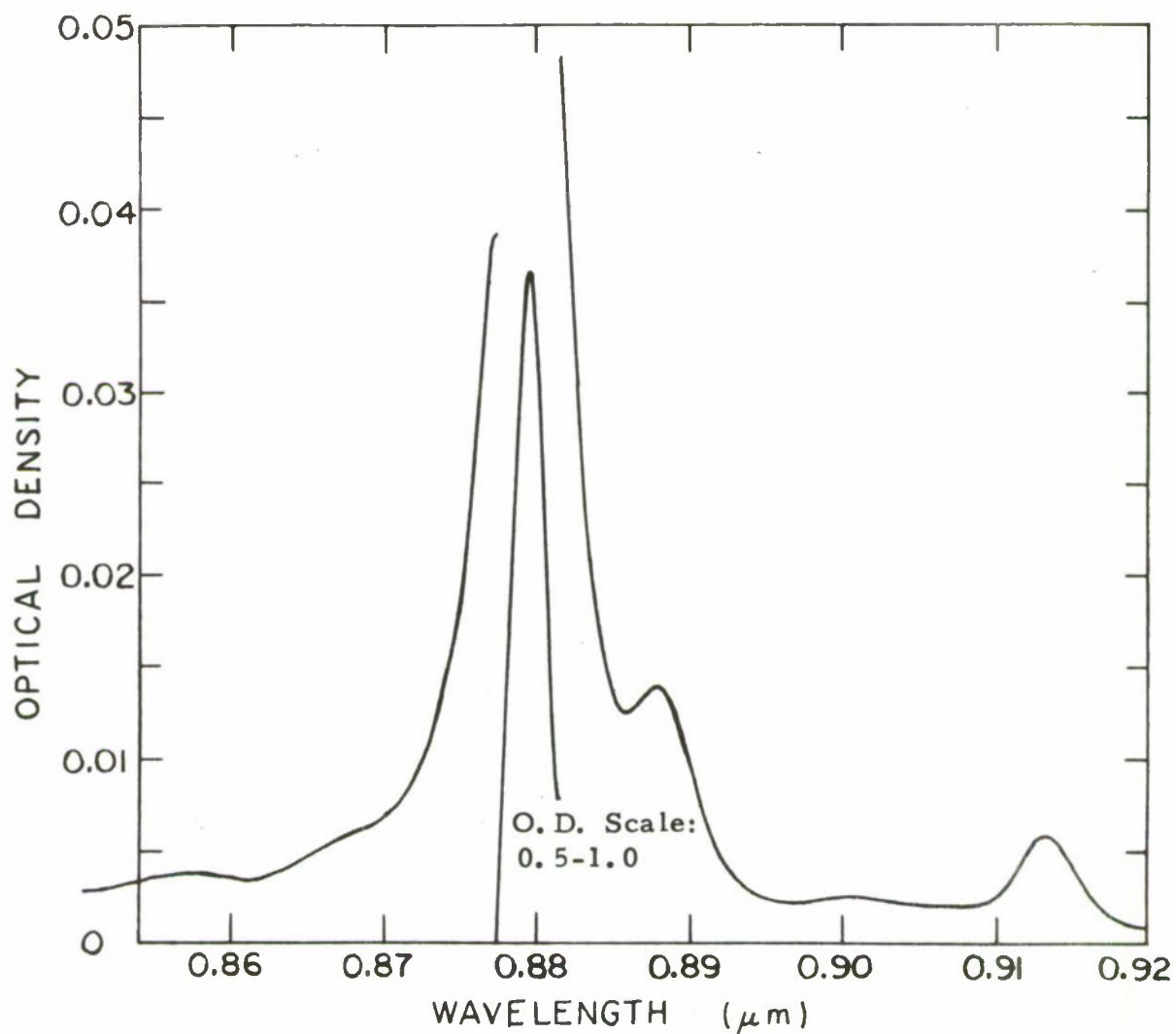
Figure 34.   0.89 μm Band of Nd:YVO₄ Absorption Spectra at Room
Temperature.   π spectrum.   1% Nd.   4 mm thick.
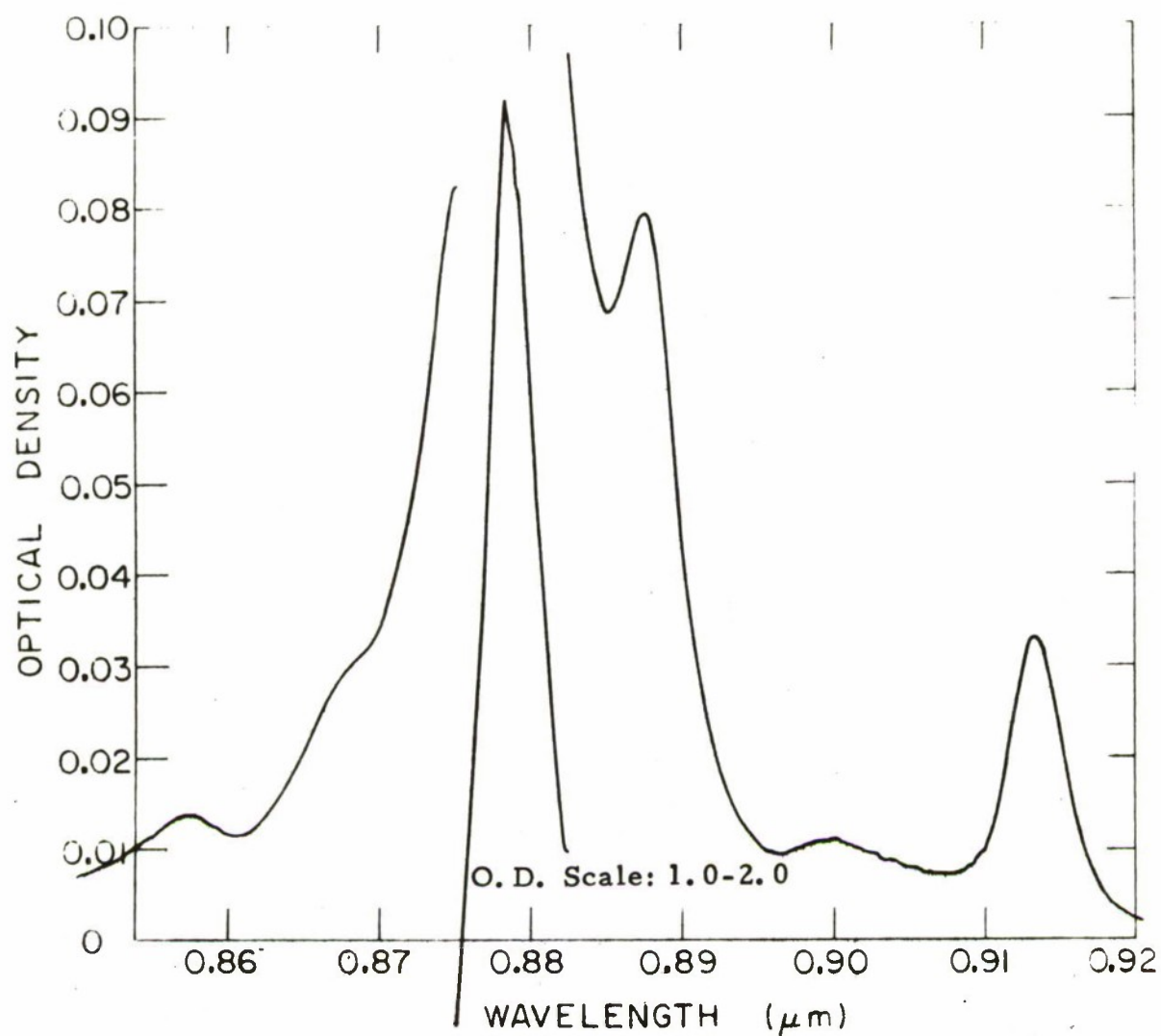
Figure 35. 0.89 μm Band of Nd:YVO$_4$ Absorption Spectra at Room Temperature. π spectrum. 3% Nd. 8.5 mm thick.
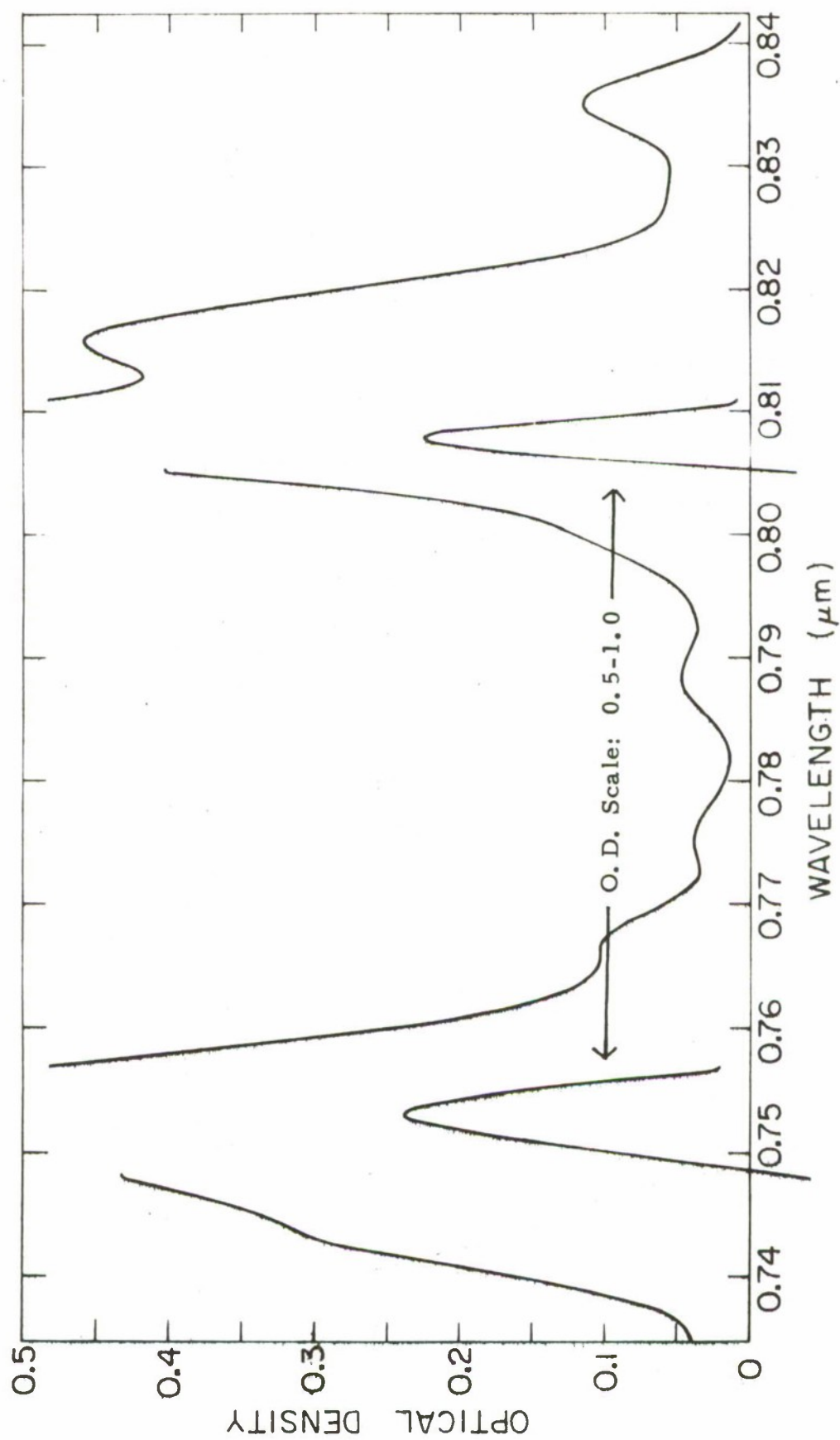
Figure 36. 0.75 and 0.81 μm Bands of Nd:YVO$_4$ Absorption Spectra at Room Temperature. σ spectrum. 1% Nd. 4 mm thick.
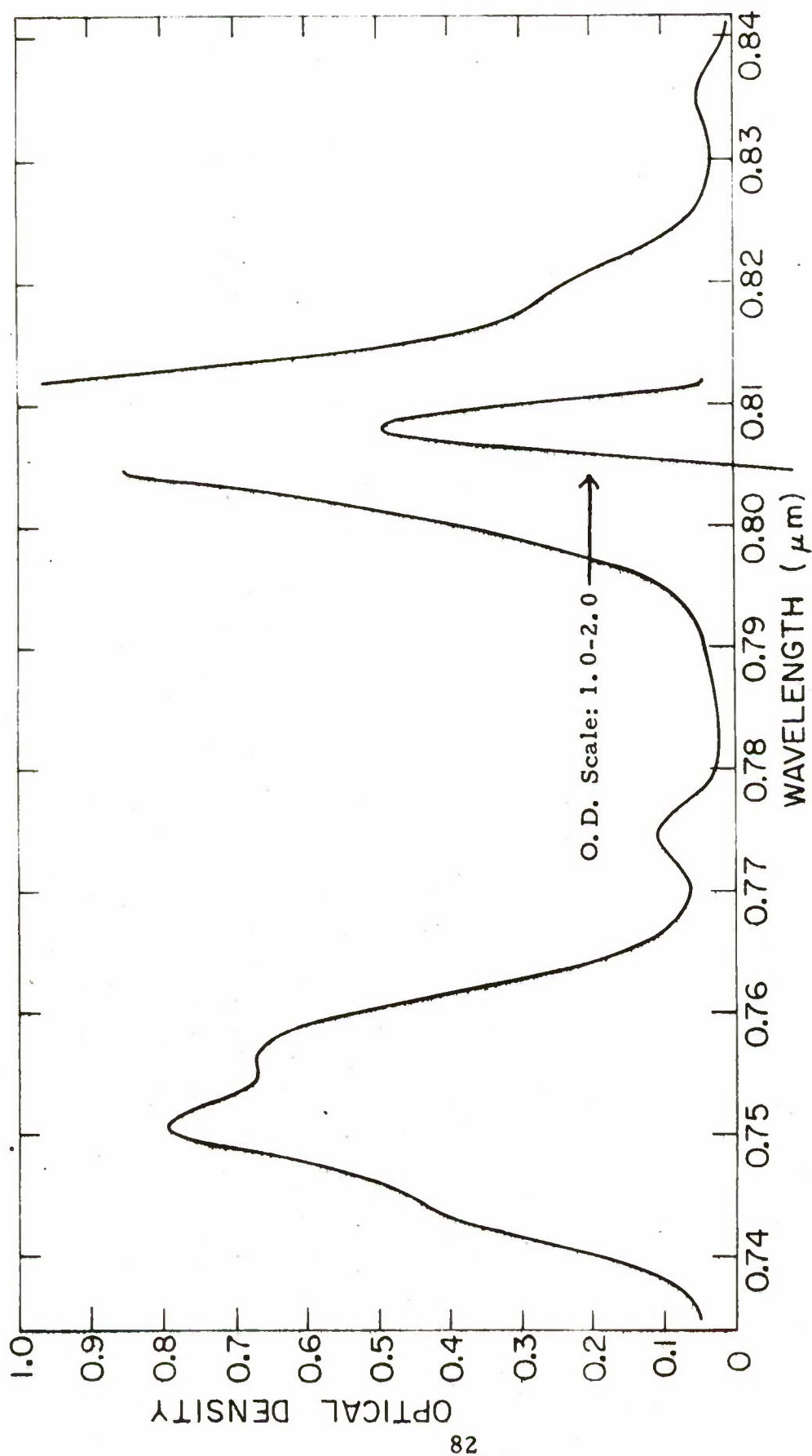
Figure 37. 0.75 and 0.81 μm Bands of Nd:YVO₄ Absorption Spectra at Room Temperature. π spectrum. 1% Nd. 4 mm thick.

O.D. Scale: 1.0-2.0
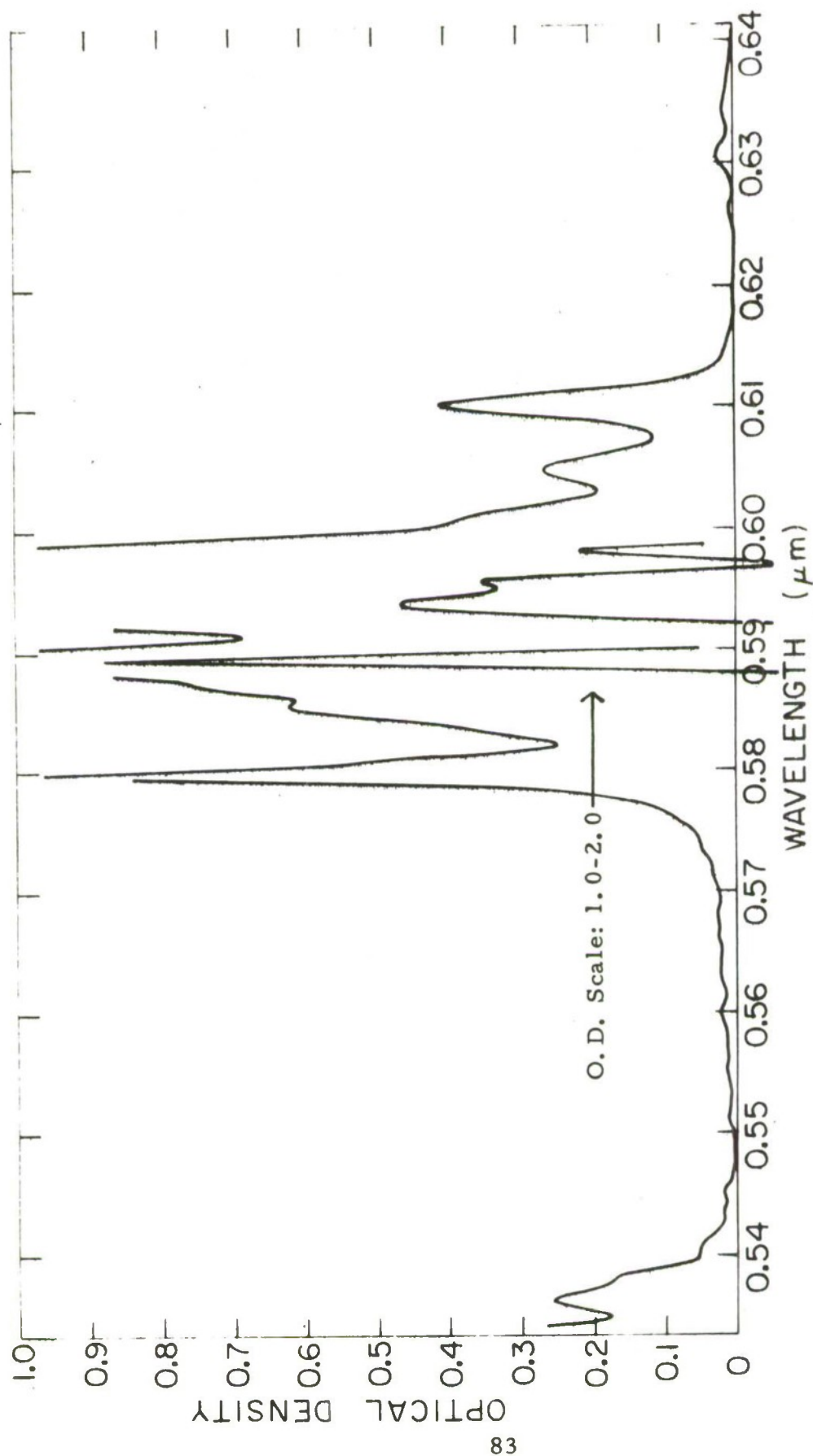
Figure 38.   0.59 μm (Yellow) Band of Nd:YVO₄ Absorption Spectra at Room Temperature. σ spectrum. 1% Nd. 4 mm thick.

83
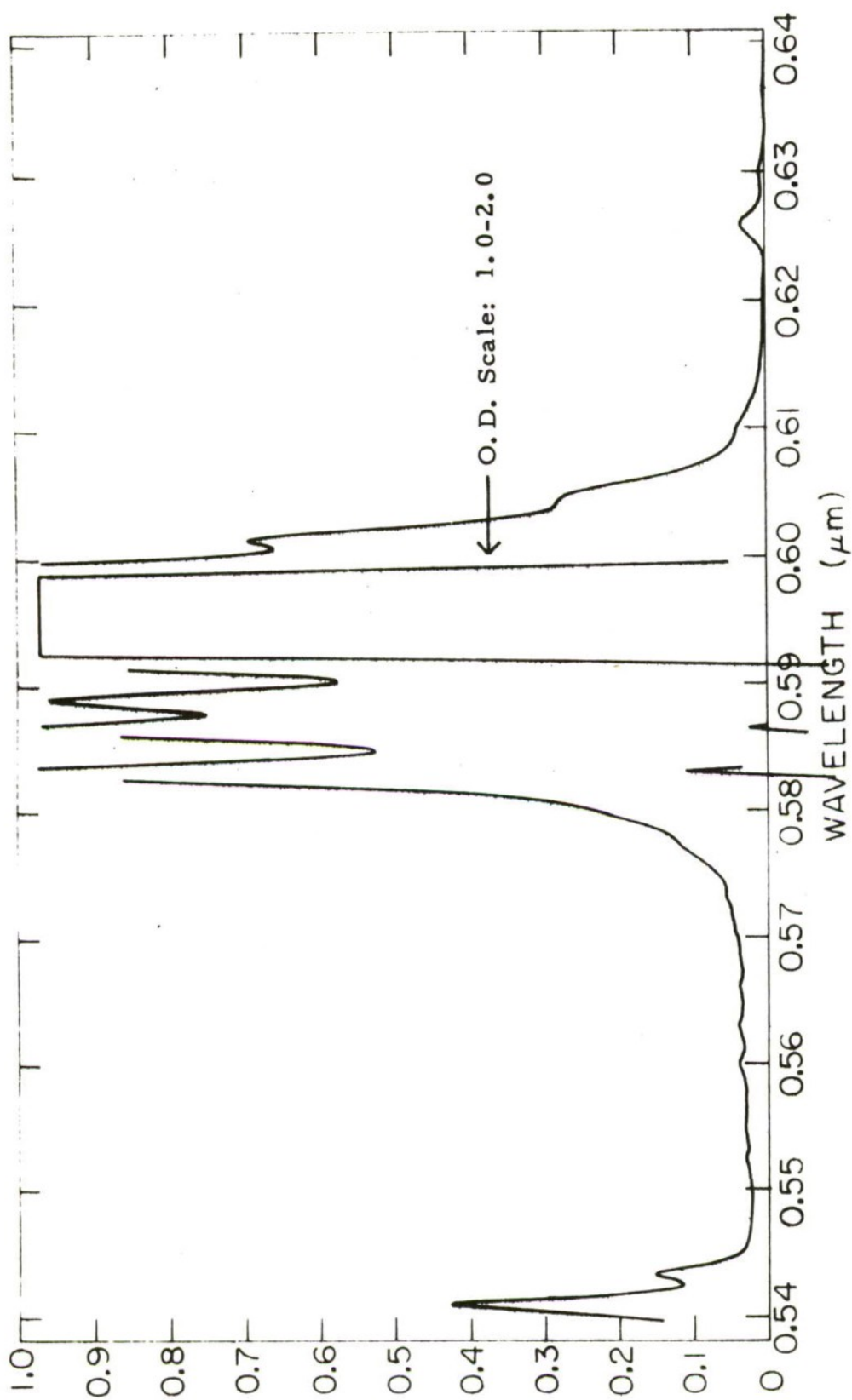
Figure 39. 0.59 μm (Yellow) Band of Nd:YVO$_4$ Absorption Spectra at Room Temperature. π spectrum. 1% Nd. 4 mm thick.

O. D. Scale: 1.0-2.0

WAVELENGTH (μm)
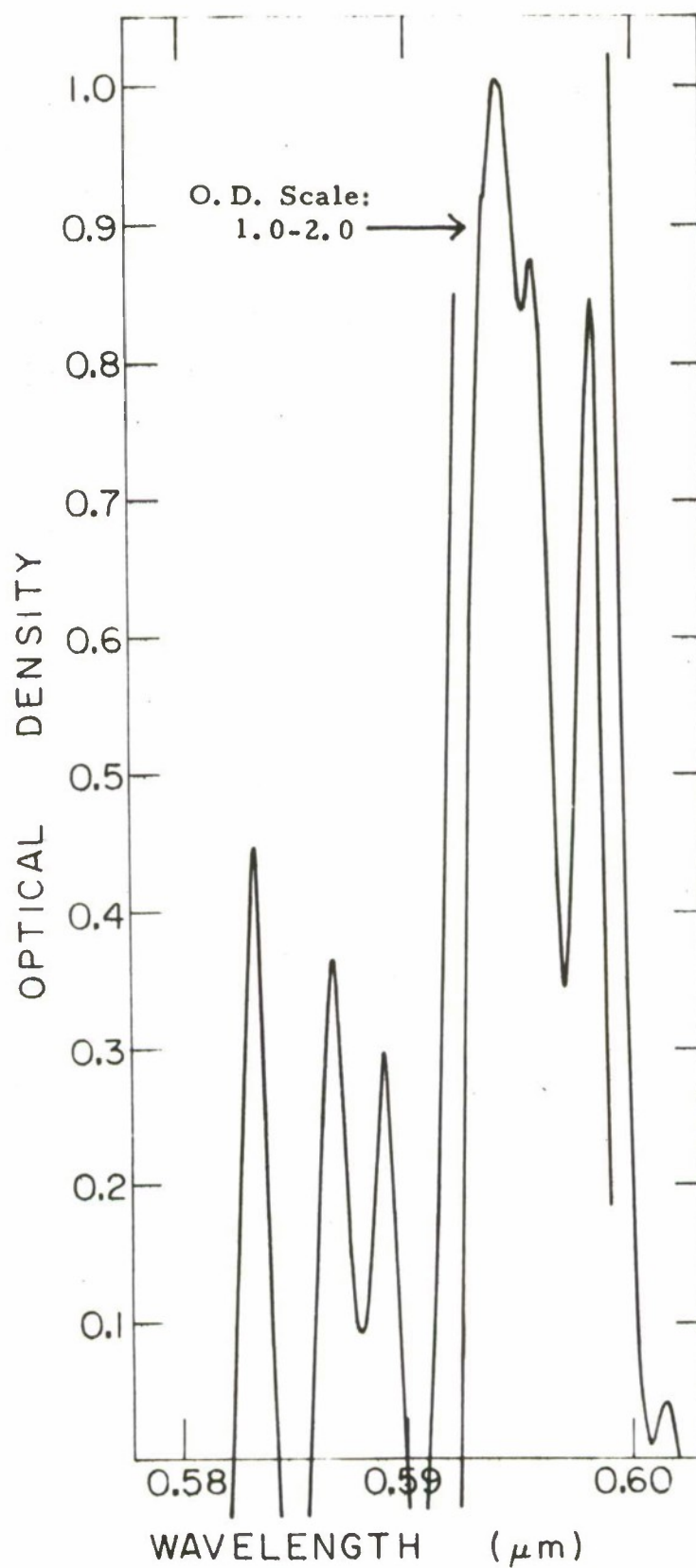
Figure 40.   Yellow Band of Nd:YVO$_4$ Absorption Spectra at Room Temperature.   π spectrum on scale. 1% Nd.   4 mm thick.
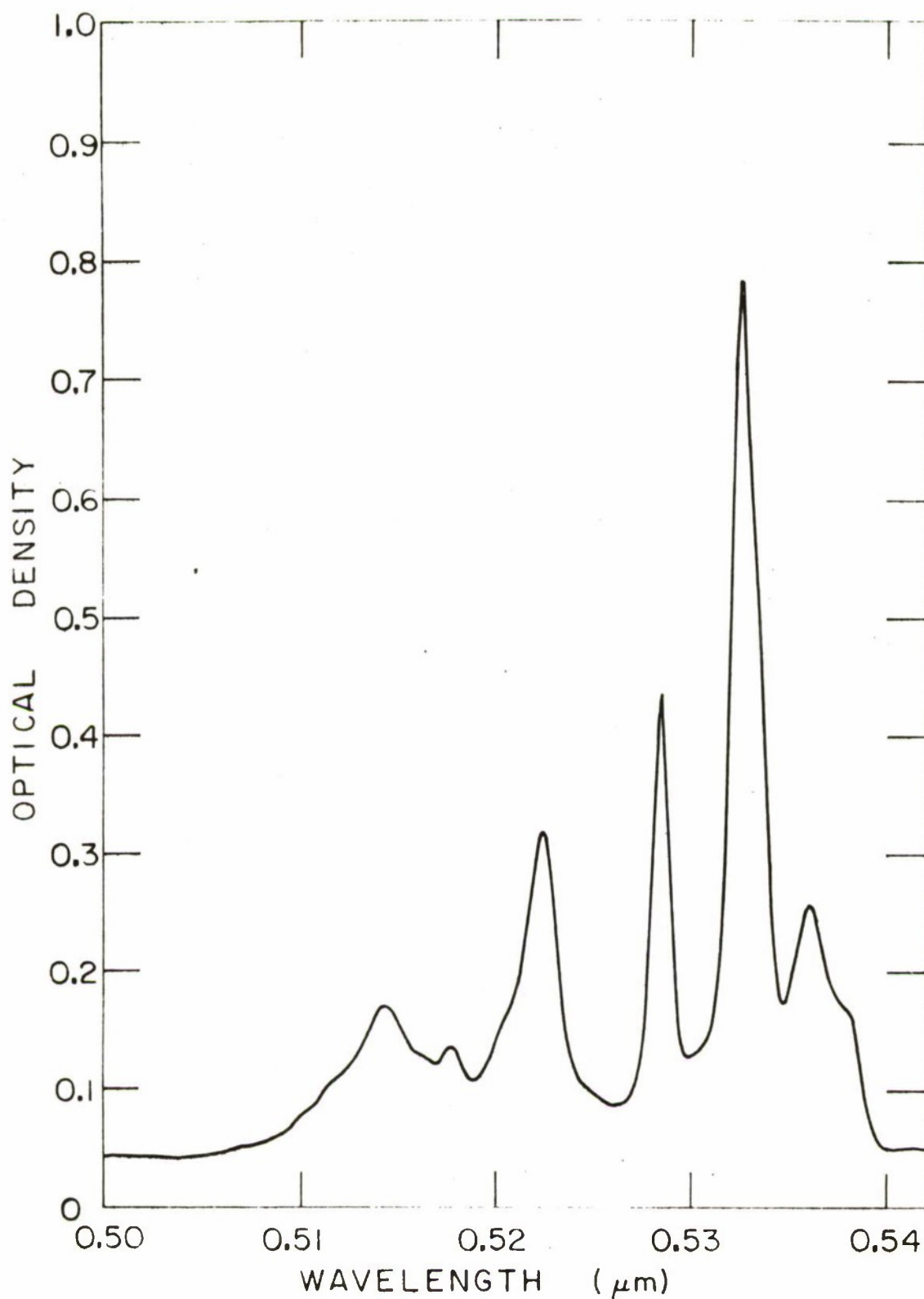
Figure 41.   0.53 μm Band of Nd:YVO$_4$ Absorption Spectra at Room
Temperature.   σ spectrum.   1% Nd.   4 mm thick.
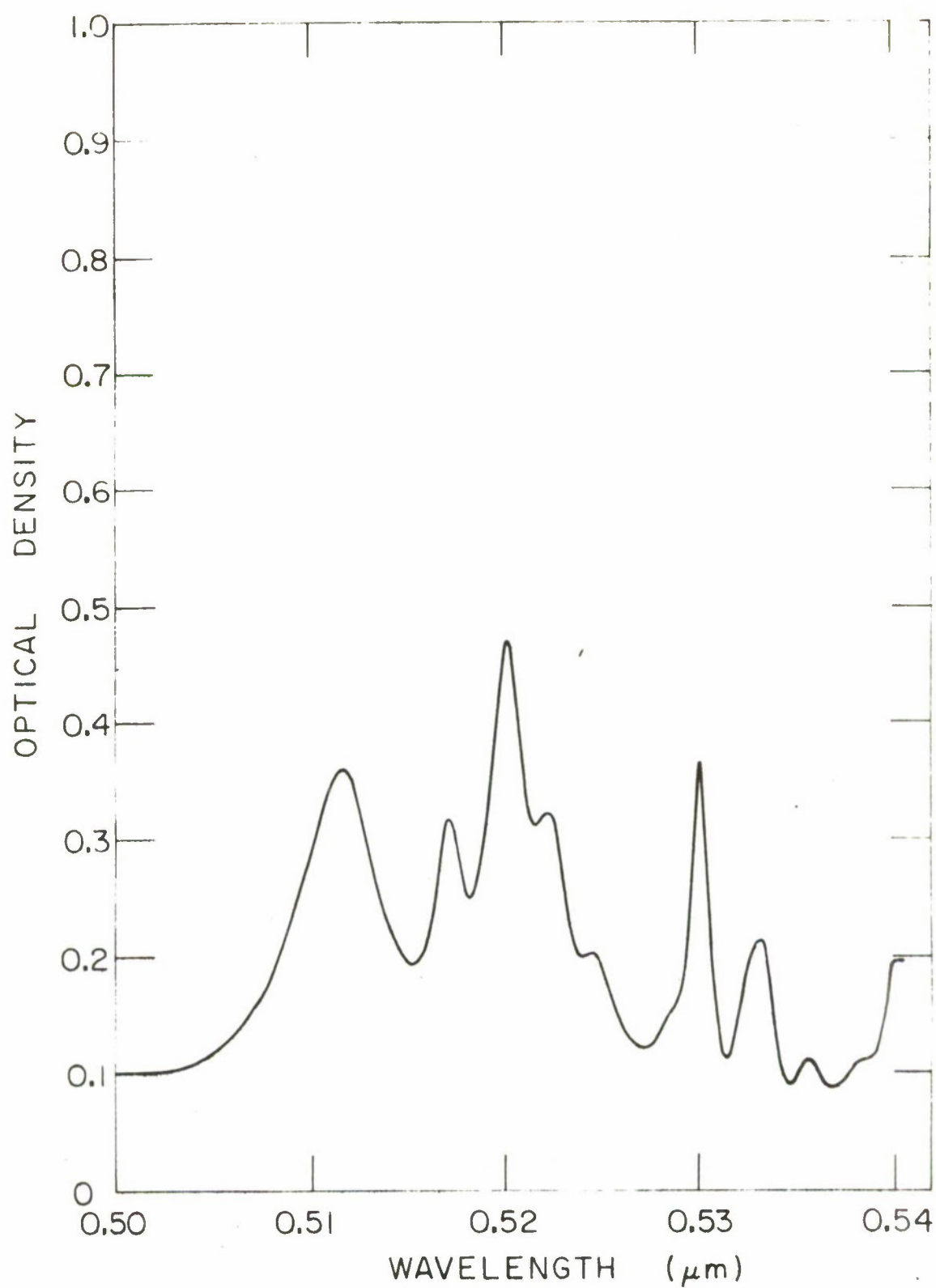
Figure 42.   0.53 μm Band of Nd:YVO$_4$ Absorption Spectra at Room Temperature.   π spectrum.   1% Nd.   4 mm thick.
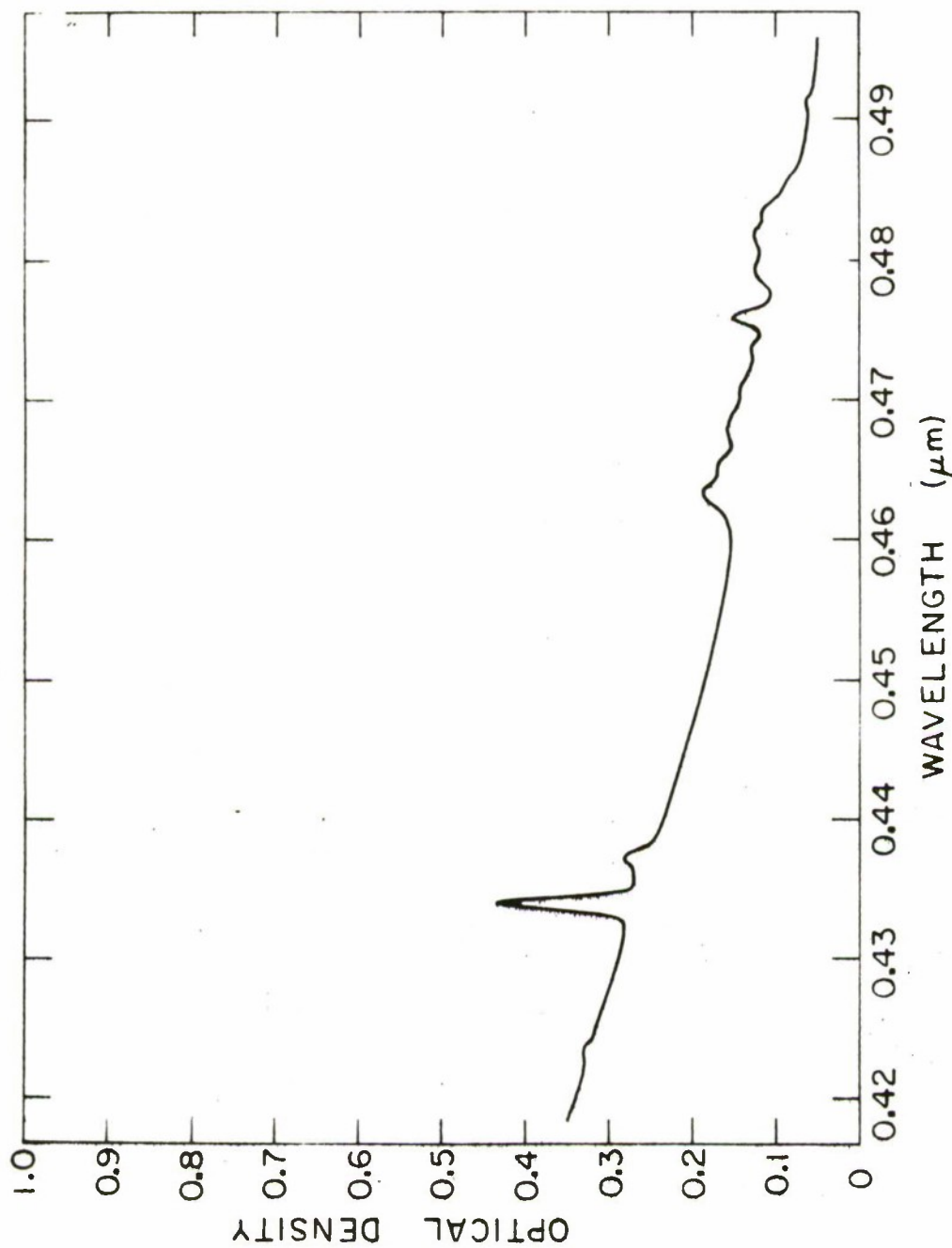
Figure 43. $\lambda < 0.5\ \mu m$ Bands of Nd:YVO$_4$ Absorption Spectra at Room Temperature. σ spectrum. 1% Nd. 4 mm thick.
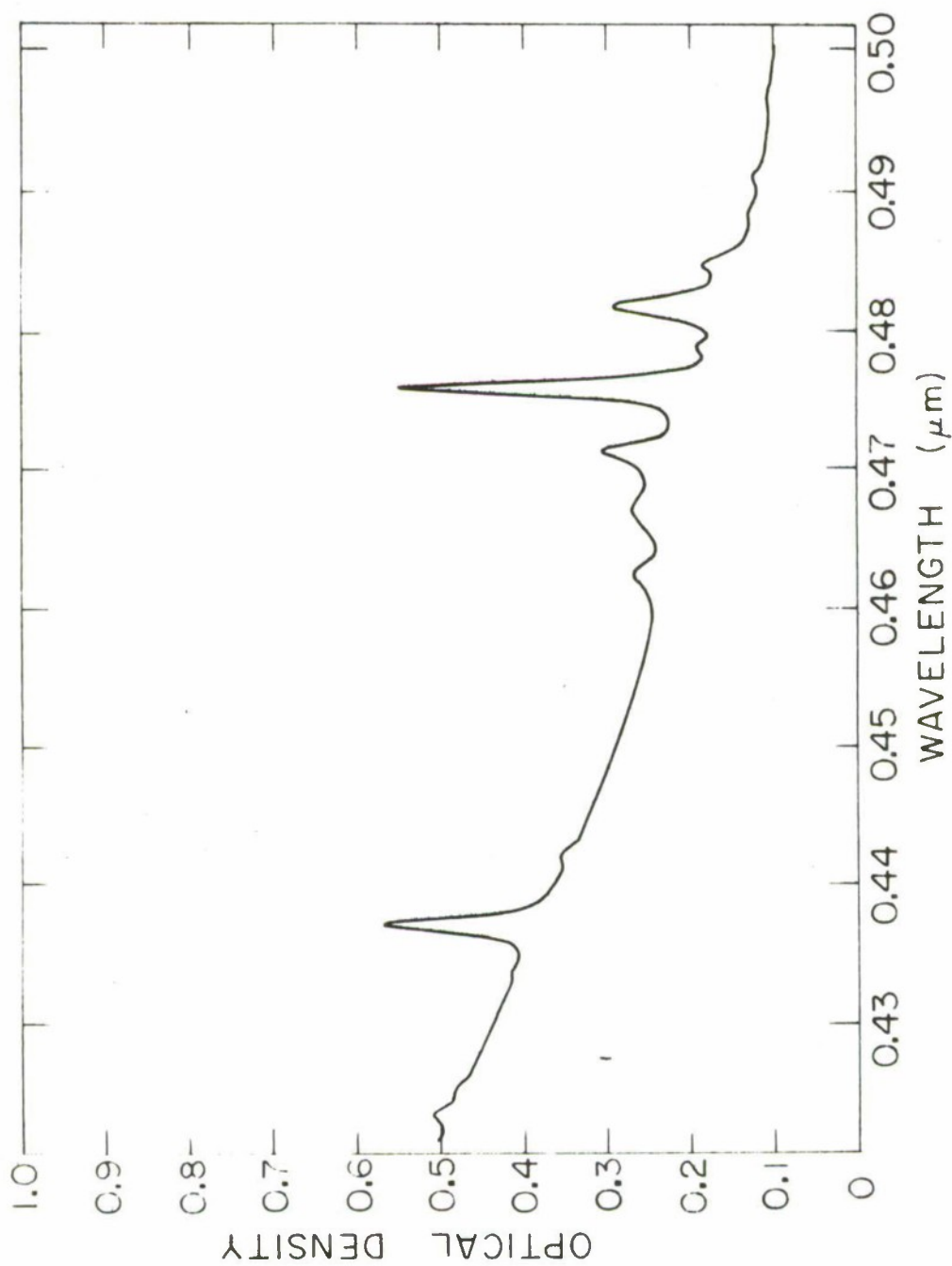
88
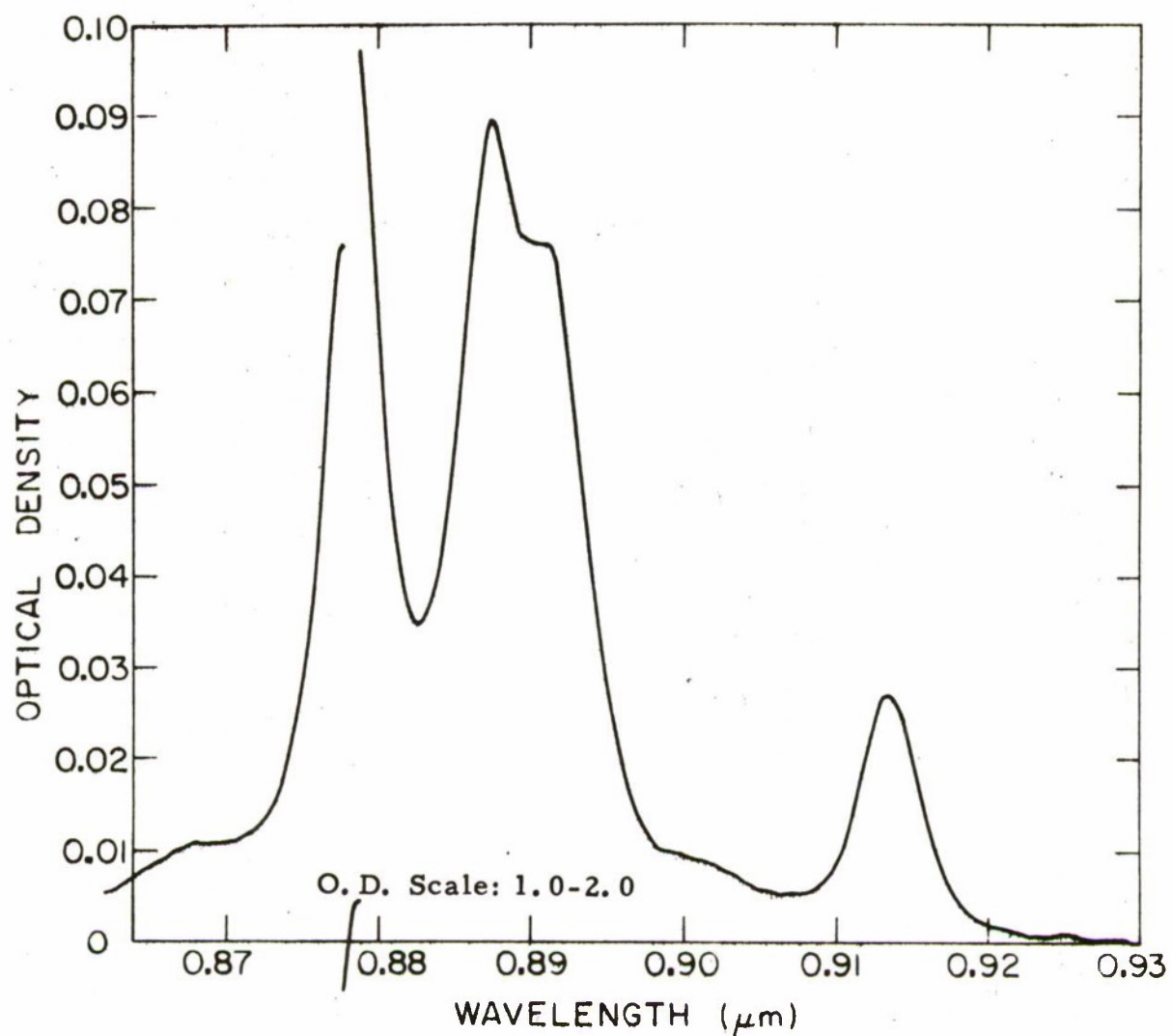
Figure 44. $\lambda < 0.5$ μm Bands of Nd:YVO$_4$ Absorption Spectra at Room Temperature. π spectrum. 1% Nd. 4 mm thick.

V. LASER PERFORMANCE TESTING

A. Laser Testing

During the second half of this project, no Nd doped YVO_4 laser rods suitable for testing were delivered by the subcontractor. Those rods that were delivered were either too short to satisfy the requirements of this program or too lossy for meaningful laser testing due to the presence of particulate scattering centers. We were therefore unable to conduct further pulse pumped Q switched laser testing of $Nd:YVO_4$. In addition, though Ho, Er, Tm:YVO_4 laser rods were delivered, we suspended the planned effort to study lasing from Ho in YVO_4 at the request of USA-ECOM.

We did, however, evaluate the effect of the ignitron in the flashlamp circuit on the laser's performance. As shown in Figure 45, the effect of the ignitron was negligible. We also tested a Nd:YAG rod in pulse pumped Q switched operation in our laser cavity. This laser rod was obtained on loan from USA-ECOM to provide data which would demonstrate the quality of our pump cavity and laser cavity optics. It would also be data which would permit easy intercomparison of our system with that in use at ECOM. Figure 46, shows this data obtained from the ECOM Nd:YAG rod and for comparison, Figure 47 is a reproduction of Figure 19 of the semiannual report which shows the Q switched performance of Nd:YVO_4 laser rod, 3L.

B. Electrooptic Q Switching of the Nd:YVO_4 Laser Without an Intracavity Polarizer

Pulse-pumped Nd:YAG lasers are often Q switched using the Pockels-cell-Glan-polarizer combination shown in Figure 48(a). Since the host material is optically isotropic, both the Pockels cell and the Glan polarizer must be placed in the optical cavity to prevent premature lasing or pre-pulsing. As indicated in Figure 48(a), when the voltage applied to the Pockels cell produces a one-quarter wave, $\lambda/4$, phase retardation at the laser wavelength, the light reflected from the 100-percent R-cavity mirror enters the

90
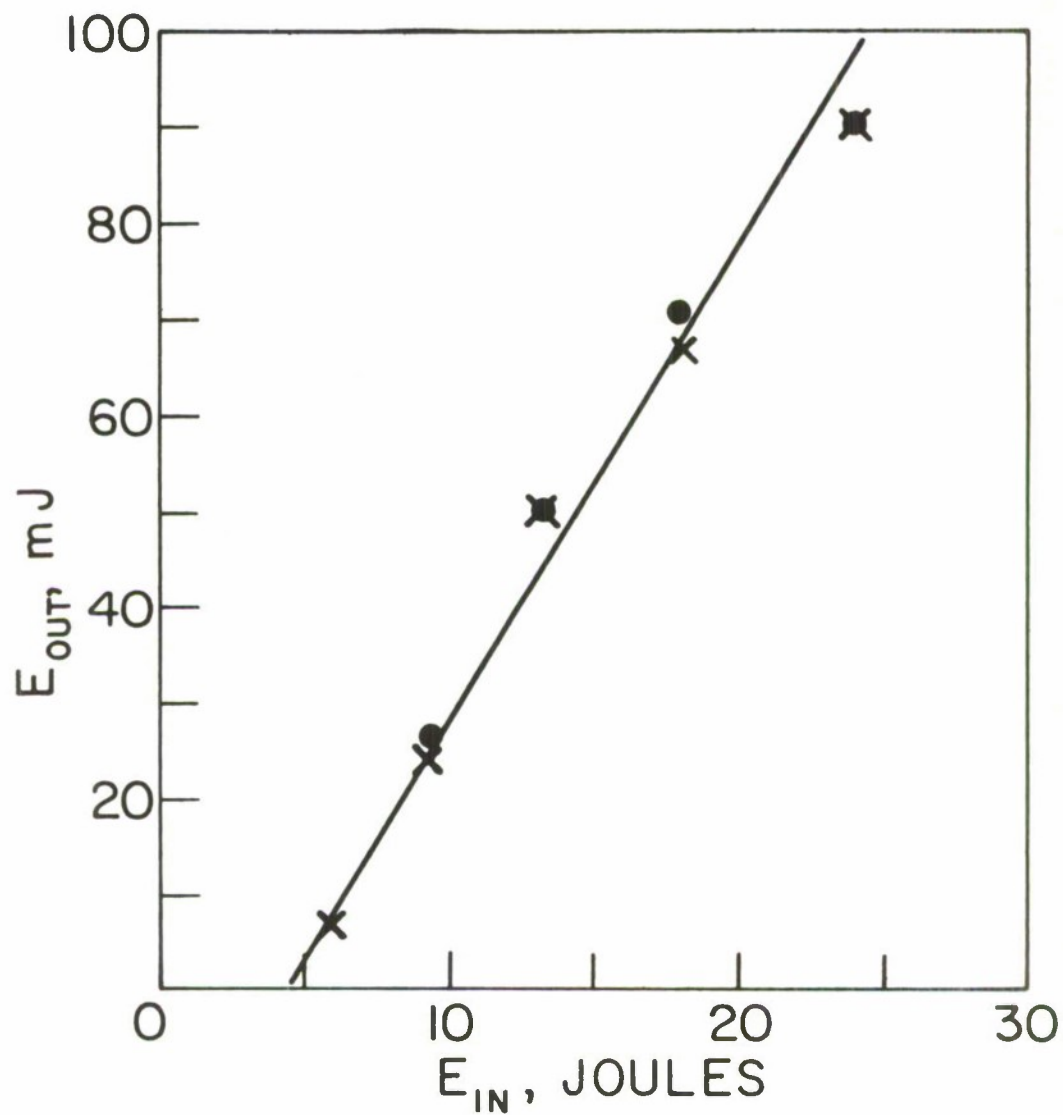
Figure 45. Nd:YAG laser output vs. input energy data with and
without the ignitron in the discharge circuit. Current
pulse FWHM is 125 μs with a krypton-filled lamp,
1200 Torr.
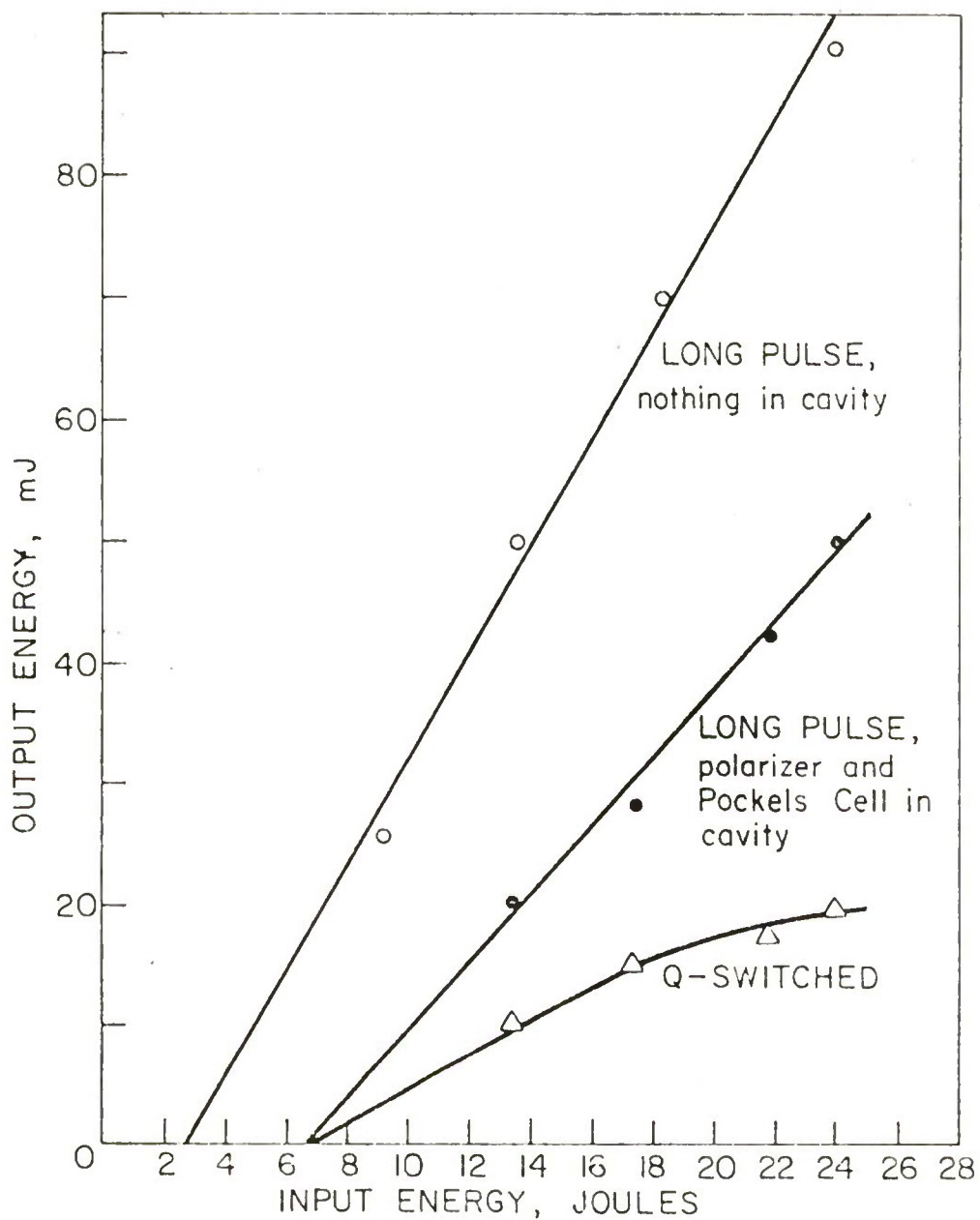
Figure 46. Output versus input energies for the 3 x 30 mm Nd:YAG (ECOM-YAG) using the Xe flashlamp (450 T) and the 125 μsec (FWHM) pump pulse duration. Output R = 45%.
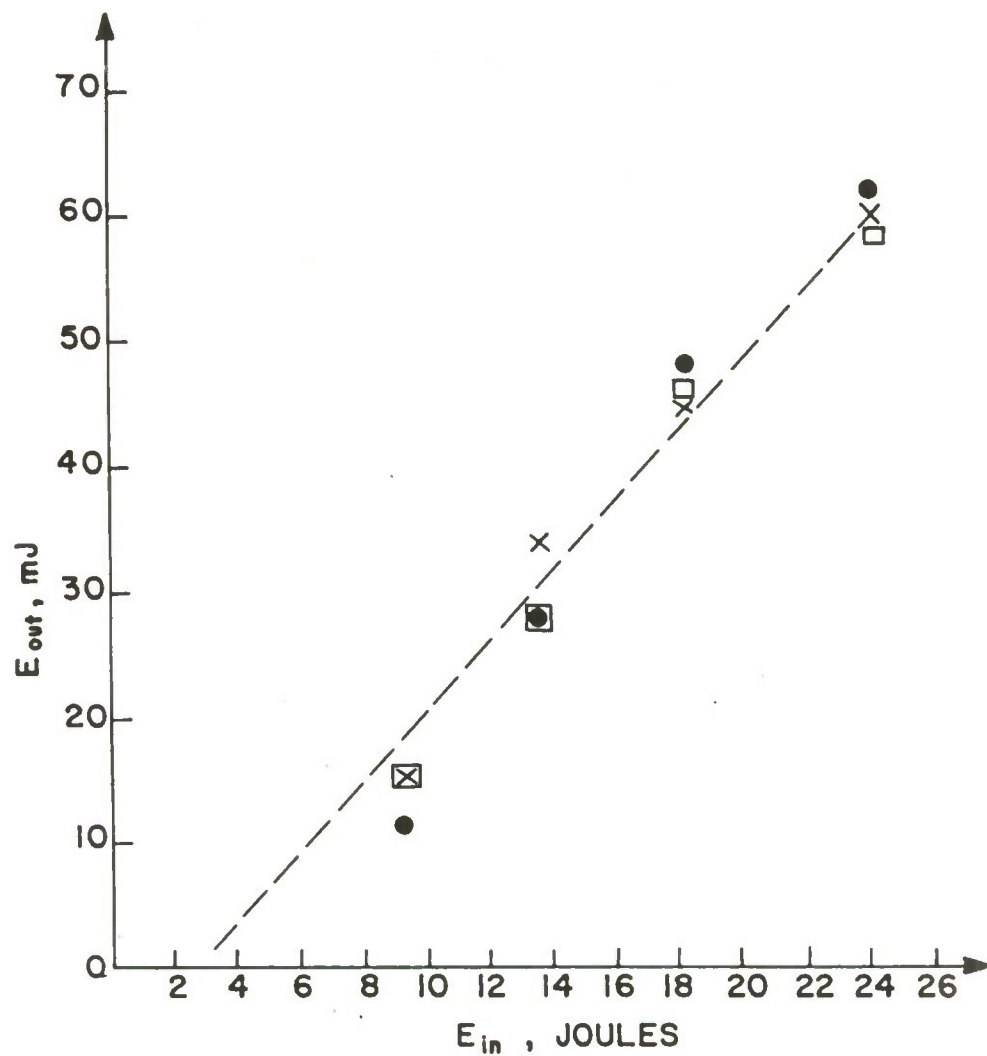
Figure 47.   Q-switched laser output vs. input energy from
Nd:YVO$_4$ (rod 3L) using a Pockels cell Q-switch
with no intracavity polarizer.   The output reflector
was 3%R at 1.06 μm.   x Pockels cell Q-switched.
o Long pulse lasing with Pockels cell in cavity.
▢ Long pulse lasing, empty cavity.
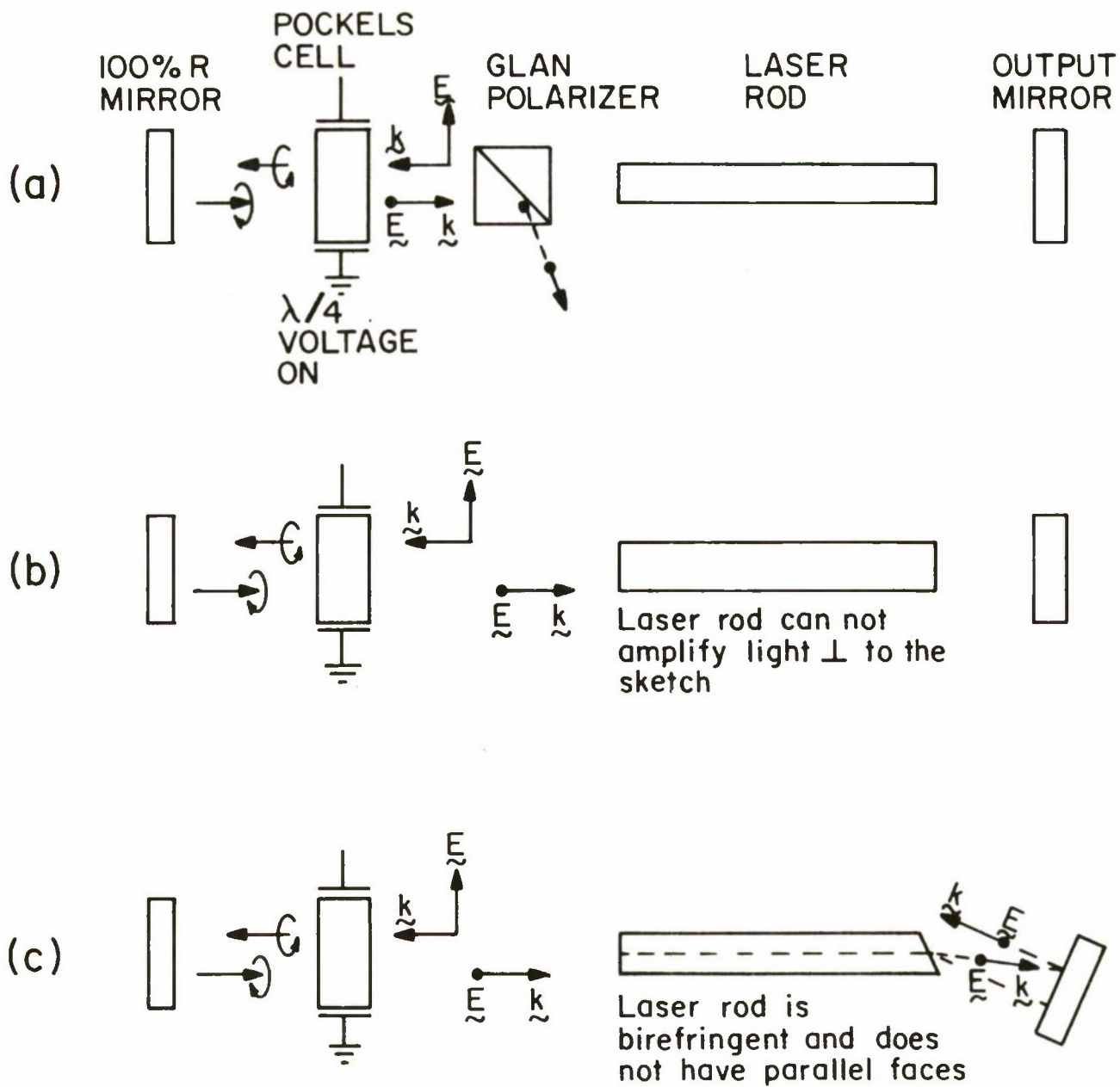
Figure 48. Electrooptically Q-switch configurations. (a) A Pockels-cell-Glan-polarizer combination in a Nd:YAG laser cavity. (b) A Pockels cell only in a cavity which has a strong polarization-dependent gain. (c) A Pockels cell in a cavity where the laser rod is slightly wedged and strongly birefringent.

94

Glan polarizer polarized so that it is not transmitted. The combination of intracavity Pockels cell and Glan polarizer thus spoils the cavity Q by isolating the 100-percent R mirror from the optical resonator. When the voltage applied to the Pockels cell is reduced to zero, there is no phase retardation, the cavity Q is restored, and an intense Q-switched pulse of laser light is produced.

A significant simplification of the Q-switched laser could be achieved if the optical resonator did not require an intracavity polarizer for prepulse free operation. This was attempted by McClung and Hellwarth [29] for a ruby laser and by Weber et al. [30] for a Nd:YAlO$_3$ laser. In both of these cases, the authors attempted to use the anisotropic properties of the laser gain in a crystalline host to prevent premature oscillation in the laser cavity.

Consider a laser cavity where the active medium has gain for light polarized in one direction only. After two complete round trips through this cavity with no intracavity polarizer and $\lambda/4$ voltage applied to the Pockels cell (see Figure 48(a)), a condition for oscillation can be reached. If this condition

$$(R_1)^2 \exp(2\beta_H \ell) = 1$$

is met, there will be prepulsing. Here R_1 is the output mirror reflectivity, β_H is the net laser gain (β_H is assumed to be zero for light polarized normal to the figure in Figure 48(b)), and ℓ is the length of pumped medium. At threshold for lasing with no voltage applied to the Pockels cell, the oscillation condition is

$$R_1 \exp(2\beta_{Th} \ell) = 1.$$

Thus $\beta_H = 2\beta_{Th}$ and so no holdoff is possible at pump levels which produce a gain equal to twice that at threshold. This is in agreement with the results in [29] and [30]. Recently, however, prepulse-free electrooptic Q switching of Nd:YVO$_4$ with no intracavity polarizer was reported at pump levels as

high as eight times threshold [7] (see Figure 47). Since the anisotropic gain of the laser crystal cannot account for such excellent performance, the explanation must lie elsewhere.

The Nd:YVO$_4$ laser rod studied in [7] was inadvertently polished so that its flat end faces were wedged with respect to each other by ~6×10^{-3} rad. This, coupled with the very strong birefringence of the YVO$_4$ host ($n_o = 1.958$ and $n_e = 2.168$ at 1.06 μm^3), permitted the laser rod to act as its own intracavity polarizer. To understand the importance of the wedge between the rod faces consider that if the flat, 0.25-percent R faces had been parallel, laser action would have occurred between the rod faces at pump levels ~3.5 times that required for lasing in the main optical resonator (100% and 3% R mirrors). Since no oscillations at all were reported with the optical-cavity mirrors misaligned, the wedge between the rod faces is sufficient to prevent unwanted lasing, and therefore is a critical factor in determining the properties of the Nd:YVO$_4$ laser.

Suppose, for simplicity, that the face of the rod nearest the 100-percent R mirror was normal to the rod axis and that the other face was misaligned by the wedge angle (6×10^{-3} rad) (see Figure 48(c)). Since the cavity mirrors were aligned for best long-pulse lasing, they were oriented so that light polarized parallel to the direction having maximum gain propagated parallel to the rod axis. In [7] the rod was nominally cut with its axis parallel to the crystalline a axis and, since maximum gain in Nd:YVO$_4$ occurs for light polarized parallel to the optic axis, light which propagated as an extraordinary ray in the laser rod was that which could oscillate.

When the Pockels cell voltage was on, light reflected from the 100-percent mirror entered the rod as an ordinary ray. As it left the Nd:YVO$_4$ rod it was not refracted far enough to be normal to the output mirror, and so no premature oscillations were possible. For the wedge angle of 6×10^{-3} rad of the Nd:YVO$_4$ laser rod in [7], the extraordinary ray would

have been refracted by 14×10^{-3} rad and the ordinary ray by 11.8×10^{-3} rad. The resulting 2.2×10^{-3} rad (0.126°) misalignment would have been sufficient to prevent prepulsing, and thus explains the excellent results reported.

The observation that a suitably birefringent laser crystal can be prepared so that is can act as its own intracavity polarizer for electrooptic Q switching can lead to great simplification in Q-switched laser systems. This was demonstrated in the present correspondence for Nd:YVO$_4$ and can be adapted to the design of other birefringent laser crystals.

VI. CONCLUSIONS AND RECOMMENDATIONS
FOR FUTURE EFFORTS

Using a laser rod designed according to the results of our spectroscopic studies we have demonstrated excellent pulse-pumped Q-switched laser performance from $Nd:YVO_4$. Due to the inherent birefringence of the host material, a wedged laser rod made possible pre-pulse free Q switching with no intracavity polarizer. This simplifies the design of laser systems using $Nd:YVO_4$ and can significantly reduce their cost.

Because of the high cross section for stimulated emission of Nd^{3+} in YVO_4, we foresee major uses of this material in pulse pumped and CW 1.06 μm laser systems where the available pump power is limited. In addition, where simplicity is essential, Q-switched lasers at 1.06 μm can benefit from the use of $Nd:YVO_4$ laser rods.

The major problems to be solved in the use of $Nd:YVO_4$ in laser systems is reliable crystal growth and fabrication techniques. Inclusions lying along cleavage planes cause cracking during cool-down and sometimes during rod fabrication. These inclusions also cause scattering and in this project resulted in Ho, Er, $Tm:YVO_4$ crystals that were too lossy to lase.

We recommend future efforts to 1) develop crystal growth and fabrication techniques, 2) study CW lasing of $Nd:YVO_4$ and 3) study Ho, Er, $Tm:YVO_4$ lasing near 2 μm.

REFERENCES

1. J.R. O'Connor, Appl. Phys. Lett. 9, 407 (1966).

2. R.J. Pressley, "Improving Solid-State Lasers," RCA Laboratories, 1969.

3. H.G. McKnight and L.R Rothrock, "Research and Development Work for the Growth of Single Crystal Yttrium Orthovanadate," Technical Report ECOM0022F, U.S. Army ECOM Contract DAAB07-72-C-0022, April 1973.

4. H.M. Dess and S.R. Bolin, paper presented at Electronics Materials Conference, Boston, Mass., Aug. 1966.

5. H.M. Dess and S.R. Bolin, Trans. Metal. Soc. AIME 239, 359 (1967).

6. L.G. DeShazer, M. Bass, U. Ranon, J.K. Guha, and E.D. Reed, VIII Intern. Quant. Elect. Conf., June 1974 (IEEE, New York), pp. 708.

7. M. Bass, L.G. DeShazer, and U. Ranon, Technical Report ECOM-74-0104-1 (October, 1974), U.S. Army ECOM, Fort Monmouth, New Jersey.

8. L.G. DeShazer, A.W. Tucker, M. Birnbaum, and C.L. Fincher, 1975 IEEE/OSA Conference on Laser Engineering and Applications, Digest of Technical Papers (IEEE, New York, 1975), Post Deadline Paper No. 4.10.

9. Kh. S. Bagdasarov, G.A. Bogomolova, A.A. Kaminskii, and V.I. Popov, Dokl. Akad. Navk SSSR 180, 1347 (1968) [Sov. Phys. Dokl. 13, 516 (1968)].

10. A.A. Kaminskii, G.A. Bogmolova, and L. Li, Izvestiya Akad. Nauk. SSSR, Neorganicheskie Materialy 5, 673 (1969).

11. R.J. Pressley, P.V. Goedertier, and H. Weakliem, "MBT 70 Laser Materials Research and Exploratory Development," RCA Lab, Princeton, New Jersey, Report (October 1969).

12. N. Karayianis, C.A. Morrison, and D.E. Wortman, Harry Diamond Laboratories, Washington, D.C. (unpublished).

13. B.R. Judd, Phys. Rev. 127, 750 (1962);
    G.S. Ofelt, J. Chem. Phys. 37, 511 (1962).

14. L. R Rothrock and R. E. Wilder (work reported in References 3 and 8).

15. R. W. G. Wyckoff, Crystal Structures, (Interscience, New York, 1963).

16. K. H. Hellwege, Ann. Physik 4, 95 (1948).

17. G. F. Koster, J. O. Dimmock, R. G. Wheeler, and H. Statz, Properties of the Thirty-Two Point Groups (M. I. T. Press, Cambridge, Mass., 1963).

18. J. A. Koningstein and J. E. Geusic, Phys. Rev. 136, A711 (1964).

19. K. Rajnak, J. Chem. Phys. 43, 847 (1965).

20. U. Ranon, Phys. Letters 28A, 228 (1968).

21. C. Brecher, H. Samelson, A. Lempicki, R. Riley, and T. Peters, Phys. Rev. 155, 178 (1967).

22. N. Karayianis and R. T. Farrar, J. Chem. Phys. 53, 3436 (1970).

23. J. L. Prather, "Atomic Energy Levels in Crystals," NBS Monograph 19 (Superintendent of Documents, Washington, D. C., 1961).

24. J. G. Gualtieri and T. R. Au Coin, J. Chem Phys. 45, 4348 (1966).

25. R. C. Rang and P. P. Yaney, Bull. Am. Phys. Soc. 19, 818 (1974); R. C. Rang, M. S. Thesis (University of Dayton, 1974) (unpublished).

26. R. E. Ziegler, P. P. Yaney, and J. A. Detrio, Technical Report AFML-TR-69-230 (December 1969) Air Force Materials Laboratory, Wright-Patterson AF Base.

27. J. A. Detrio, M. W. Ferralli, P. P. Yaney, D. M. Ware, and V. L. Dolan, J. Chem. Phys. 53, 4372 (1970).

28. R. T. Harley, W. Hayes, and S. R. P. Smith, Solid State Commun. 9, 515 (1971).

29. F. J. McClung and R. W. Hellwarth, J. Appl. Phys. 33, 828, (Mar. 1962).

30. M. J. Weber, M. Bass, K. Andringa, R. R. Monchamp and E. Comperchio, Appl. Phys. Lett. 15, 342 (Nov. 1969).

Analysis of Laser Emission in Ho³⁺-Doped Materials

JOHN A. CAIRD AND LARRY G. DeSHAZER

Abstract—The oscillator strengths, transition rates, and branching ratios associated with known and potential laser transitions in trivalent holmium are discussed. Recently reported laser transitions between the ⁵F₅ and ⁵I₅ energy manifolds are found to have an abnormally low average oscillator strength, and an alternative explanation of the laser observation is suggested.

I. INTRODUCTION

INDUCED electric dipole oscillator strengths and transition rates between energy levels of rare-earth ions in crystals can be calculated using a theory developed by Judd [1] and Ofelt [2]. In recent years the Judd–Ofelt (JO) model has been used in the analysis of rare-earth laser materials [3]–[6], and its use led to the discovery of the four-level Tm:Cr:YAlO₃ laser at 2.35 μm [7]. This paper reports the results of an application of the JO model to known and potential laser transitions in trivalent holmium.

II. THEORETICAL BACKGROUND

According to the JO model, the oscillator strength f and spontaneous emission rate A of crystal field induced electric dipole fluorescence in a rare-earth ion are given by [8]

$$f_{JJ'} = \frac{8\pi^2 mc}{3h\overline{\lambda}(2J+1)} \left[\frac{(n^2+2)^2}{9n} \right]$$
$$\cdot \sum_{t=2,4,6} \Omega_t |\langle 4f^n[S,L]J\|U^t\|4f^n[S',L']J'\rangle|^2 \quad (1)$$

and

$$A_{JJ'} = \frac{8\pi^2 e^2 n^2}{mc\overline{\lambda}^2} \cdot f_{JJ'} \quad (2)$$

where $\overline{\lambda}$ is the mean wavelength associated with the transition, n is the crystal's index of refraction at the mean wavelength, and $2J+1$ is the number of levels in the upper J-manifold. In (1) the $\langle\|U^{(t)}\|\rangle$ are doubly reduced matrix elements of unit tensor operators calculated in the intermediate coupling approximation [1], and the Ω_t are three empirical parameters. These empirical parameters can generally be determined for each ion-host combination by a least squares fit between calculated and measured oscillator strengths in the absorption

spectrum. Equation (1) may then be used to calculate oscillator strengths in the fluorescence spectrum. It should be noted that (1) gives the oscillator strength summed over the Stark split components of the final energy manifold J' and averaged over the components of the initial energy manifold J.

The cross section for stimulated emission integrated over all Stark split components of the upper and lower J-manifolds is given by [5]

$$\int_{J \to J'} o(\nu)\, d\nu = \frac{\overline{\lambda}^2}{8\pi c n^2} A_{JJ'} \quad (3)$$

where $\nu = 1/\lambda$. Using (2) this reduces to

$$\int_{J \to J'} o(\nu)\, d\nu = \frac{\pi e^2}{mc^2} f_{JJ'} \quad (4)$$

which shows the significance of the oscillator strength in laser analysis. Without detailed line shape information (4) cannot be used to predict peak cross sections, but it is evident that transitions with larger oscillator strengths will generally have larger peak cross sections.

In the $4f^n$ ground configuration of rare-earth ions, electric dipole transitions become allowed only when the ion feels a perturbing field lacking inversion symmetry so that parity restrictions are broken. Magnetic dipole (md) transitions between levels with $|\Delta J \leqslant 1|$ are always allowed, however, and can on occasion be comparable in strength to the crystal field induced electric dipole (ed) transitions. A definition of the md oscillator strength consistent with (2) and (4) is given by [9]

$$f_{JJ'}\,(\text{md}) = \frac{h}{6\overline{\lambda}(2J+1)mc}$$
$$\cdot n\,|\langle 4f^n[S,L]J\|L+2S\|4f^n[S',L']J'\rangle|^2 \quad (5)$$

where the matrix elements of $L+2S$ can be evaluated using standard formulas given elsewhere [10].

A computer program was developed capable of calculating the unit tensor operator matrix elements in (1) between all J-manifolds in all rare-earth ions using previously published intermediate coupling wave functions [6]. The program was then used to calculate ed and md oscillator strengths, transition rates, and radiative branching ratios for a large number of ion-host combinations for which intensity parameters Ω_t had been published. The branching ratio for a transition $i \to j$ is simply given by

$$\beta_{i \to j} = \frac{A(i \to j)}{\sum_{j'} A(i \to j')} \quad (6)$$

where the sum in the denominator is over all states of lower energy. In these calculations emphasis was placed on transitions for which laser action and/or fluorescence has been reported, and those for which the radiative transition rates were large enough to exceed multiphonon emission rates. It was found that the vast majority of laser lines had oscillator strengths greater than 10^{-6}. In a few notable exceptions although the oscillator strengths were somewhat lower than 10^{-6}, the branching ratio associated with the laser transition was particularly high, and the upper level lifetime was long, allowing for the buildup of a large inversion density. The only other exceptions were found in cases where a trivalent rare-earth ion was placed on a divalent ion site in the laser material.

III. APPLICATION TO HOLMIUM

Laser emission from Ho^{3+} ions has been observed in many hosts on transitions between the $^5I_7$ and $^5I_8$ energy manifolds at wavelengths near 2 μm. Laser action in the green near 0.55 μm has also been reported on $[^5S_2, {}^5F_4] \rightarrow {}^5I_8$ transitions in CaF_2 [11] and BaY_2F_8 [12]. Recently stimulated emission in $Ho:BaY_2F_8$ near 2.4 μm has been attributed to transitions within the $^5F_5 \rightarrow {}^5I_5$ group [13]. Fluorescence originating in the $^5I_6$ state has also been observed in a number of crystals [9], [13], [14], but emission from other levels is often quenched by nonradiative processes.

The intensity parameters in the JO model for $Ho:YAlO_3$ were determined by Weber et al. [9] to be 1.82, 2.38, and 1.53 ($\times 10^{-20}$ cm^2) for Ω_2, Ω_4, and Ω_6, respectively. The electric dipole oscillator strengths and transition rates for fluorescence from low lying energy levels of Ho^{+3} in $YAlO_3$ can be easily derived from data given in [9] along with the indices of refraction of $YAlO_3$ given in [15]. These are tabulated for transitions from the $^5I_7$, $^5I_6$, $^5F_5$, and $[^5S_2, {}^5F_4]$ states in Table I. Calculation of the md contributions in Table I required the use of intermediate coupling wave functions for Ho^{3+} which were obtained from the authors of [9]. The branching ratios are in close agreement with those reported in [9], with the exception of the $^5F_5 \rightarrow {}^5I_4$ transition for which the ratio is found to be much smaller than previously reported.

Examination of Table I shows that the laser transitions $^5I_7 \rightarrow {}^5I_8$ and $[^5S_2, {}^5F_4] \rightarrow {}^5I_8$ have oscillator strengths greater than 10^{-6}, consistent with most other rare-earth lasers [6]. It is interesting to note that $^5F_4 \rightarrow {}^5I_8$ transitions may be more important than $^5S_2 \rightarrow {}^5I_8$ transitions for green laser emission, and therefore the relative positions of the $^5S_2$ and $^5F_4$ energy levels may have a large effect on laser performance. The $^5S_2 \rightarrow {}^5I_7$ transition at 0.76 μm also appears to have sufficient strength to support laser oscillation, but the $^5I_7$ lifetime is longer than the $^5S_2$, so that quenching of the $^5I_7$ level may be required. Conditions also appear to be favorable for laser emission on both the $^5I_6 \rightarrow {}^5I_7$ line at 2.9 μm and the $^5I_6 \rightarrow {}^5I_8$ line at 1.2 μm, particularly since the fluorescence lifetime of the $^5I_6$ level is reasonably long. At least one attempt to achieve laser action on the $^5I_6 \rightarrow {}^5I_7$ transition,

TABLE I
OSCILLATOR STRENGTHS, TRANSITION RATES, AND BRANCHING RATIOS FOR Ho:YAlO3

Upper Level	Lower Level	Average frequency (cm^{-1}) [ref. 9]	Oscillator Strength ($\times 10^6$)		Transition Rate (sec^{-1})		Radiative Branching Ratio
			electric dipole	magnetic dipole	electric dipole	magnetic dipole	
$^5I_7$	$^5I_8$	5150	1.87	0.66	115	43	1.000
$^5I_6$	$^5I_7$	3500	0.98	0.74	10	22	.16
	$^5I_8$	8540	1.56	--	280	--	.84
$^5F_5$	$^5I_4$	2500	.008	.003	.11	.04	(.0001)
	$^5I_5$	4350	.26	.02	12	1.0	.0032
	$^5I_6$	6918	1.56	.01	160	1.5	.039
	$^5I_7$	10410	2.86	--	770	--	.18
	$^5I_8$	15450	5.46	--	3270	--	.78
$^5S_2$	$^5F_5$	2740	0.04	--	0.6	--	.0002
	$^5I_4$	5030	1.00	--	61	--	.016
	$^5I_5$	7090	8.30	--	62	--	.015
	$^5I_6$	9450	1.12	--	260	--	.054
	$^5I_7$	13150	3.58	--	1450	--	.16
	$^5I_8$	18190	2.62	--	2190	--	.54
$^5F_4$	$^5F_5$	3090	0.41	0.29	9.6	6.8	.002
	$^5I_4$	5380	0.55	.001	59	.07	.005
	$^5I_5$	7440	1.75	.003	240	.41	.031
	$^5I_6$	10000	1.98	--	490	--	.064
	$^5I_7$	13500	1.61	--	710	--	.095
	$^5I_8$	18540	7.08	--	6160	--	.80

however, was unsuccessful [13] even though the $^5I_7$ lifetime was significantly shortened by addition of Pr^{3+} and Eu^{3+} ions.

The oscillator strength of the $^5F_5 \rightarrow {}^5I_5$ emission is seen to be very small in comparison to other rare-earth lasers, and to the other holmium lasers in particular. The transition does not have mitigating advantages either. The upper level lifetime is not long, the lower level lifetime is long (predicted), and the radiative branching ratio is very small. It would seem that stimulated emission from the $^5F_5$ level and terminating on the $^5I_6$, $^5I_7$, and $^5I_8$ levels should have been observed first. One might ask if the intensity parameters for BaY_2F_8 could be much larger than in $YAlO_3$. The predicted radiative lifetimes for the $^5I_6$ and $^5I_7$ levels in $YAlO_3$ are 3 and 6 ms, respectively, while the measured lifetimes in BaY_2F_8 are 5 and 16 ms, respectively [13], indicating that the intensity parameters for BaY_2F_8 must in fact be smaller than for $YAlO_3$. In addition, examination of the unit tensor operator matrix elements involved [9] shows that changing the relative magnitudes of the three intensity parameters could not change the branching ratio appreciably. It could be that the stimulated emission cross section for this transition is sharply peaked, while the integral (4) remains small. However, laser oscillation was reported on three different lines: 2.362 μm, 2.375 μm, and 2.377 μm.

Our own work on the $Tm:YAlO_3$ laser at 2.3 μm [16] leads us to suggest that the emission seen by Johnson and Guggenheim may have been due to impurity thulium ions in their laser rod. It should be noted at the outset, however, that the authors of [13] indicate that the $Ho:BaY_2F_8$ laser

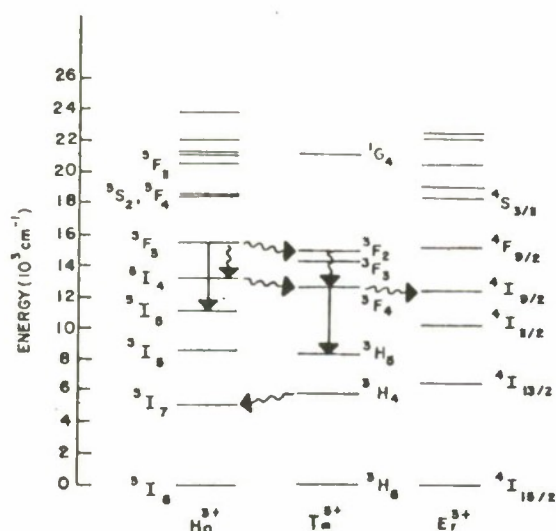Fig. 1. Energy levels of Ho^{3+}, Tm^{3+}, and Er^{3+} indicating transitions in the 2.3-2.4-μm region.

material was of very high purity and that no fluorescence typical of thulium was observed [17].

Fig. I compares the energy levels and laser transitions of Ho^{3+} and Tm^{3+} in question. Er^{3+} is included for later discussion. The laser wavelengths which have been observed in $Tm:YAlO_3$ on $^3F_4 \rightarrow ^3H_5$ transitions are 2.348 μm, 2.349 μm [18], and 2.272 μm [19], while the range of possible wavelengths in this group extends from 2.13 to 2.61 μm based on the energy levels given in [18]. Also indicated in Fig. 1 are possible mechanisms for nonradiative transfer from Ho^{3+} to Tm^{3+}. This excitation scheme is consistent with the observations of Johnson and Guggenheim since they indicate laser oscillation is initiated by pumping the $^5F_5$ level of Ho^{3+}. Nonradiative transfer from Ho^{3+} $^5I_4$ to Tm^{3+} $^3F_4$ is also possible, but direct excitation of the $^5I_4$ level of Ho^{3+} is ineffective because the absorption of the $^5I_4$ level is extremely weak. Cessation of oscillation early in the pump pulse attributed to terminal state population buildup was observed [13] and may be consistent with the Tm^{3+} $^3H_5$ level lifetime in BaY_2F_8 (though this is not observed in $YAlO_3$). The normal thulium $^3H_4 \rightarrow ^3H_6$ fluorescence at 1.9 μm would be quenched by nonradiative energy transfer from the Tm^{3+} $^3H_4$ to the Ho^{3+} $^5I_7$ level, and would therefore be difficult to observe. Fluorescence from the $^3F_4 \rightarrow ^3H_6$ transition at 0.8 μm might be expected, however, if thulium were responsible for the laser action. One might ask why the Tm^{3+} transition is not observed to lase in a large number of crystals in which Ho^{3+}, Er^{3+}, and Tm^{3+} are doped together to sensitize the 2-μm transition in holmium. Reference to Fig. 1 shows that the presence of erbium in these cases would quench fluorescence from the $^3F_4$ level of Tm^{3+} by nonradiative energy transfer to the $^4I_{9/2}$ level of Er^{3+}.

IV. SUMMARY AND CONCLUSION

An analysis of holmium laser transitions has been performed based primarily on the Judd-Ofelt theory of crystal field induced electric dipole oscillator strengths. The JO model appears to be useful in describing some of the actual and potential laser properties of Ho^{3+}, except in the case of the reported $^5F_5 \rightarrow ^5I_5$ transitions. The observation of laser emission from holmium on these lines would not indicate a breakdown of the JO model, but would show that the applicability of the JO model to laser analysis is limited in its present form. If, however, the observed emission could be attributed to thulium impurities in the crystal, the JO model will have been a useful tool in the identification and prediction of the laser transitions.

REFERENCES

[1] B. R. Judd, "Optical absorption intensities of rare-earth ions," *Phys. Rev.*, vol. 127, pp. 750-761, 1962.
[2] G. S. Ofelt, "Intensities of crystal spectra of rare-earth ions," *J. Chem. Phys.*, vol. 37, pp. 511-520, 1962.
[3] W. F. Krupke, "Radiative transition probabilities within the $4f^3$ ground configuration of Nd:YAG," *IEEE J. Quantum Electron.*, vol. QE-7, pp. 153-159, Apr. 1971.
[4] ——, "Assessment of a promethium YAG laser," *IEEE J. Quantum Electron.* (Corresp.), vol. QE-8, pp. 725-726, Aug. 1972.
[5] ——, "Induced-emission cross sections in neodymium laser glasses," *IEEE J. Quantum Electron.*, vol. QE-10, pp. 450-457, Apr. 1974.
[6] J. A. Caird, "Theoretical analysis of rare-earth laser materials," in the *Optical Society of America 1974 Spring Meeting Program* (Washington, D.C.), Apr. 21-25, p. 535.
[7] L. M. Hobrock *et al.*, "Four-level operation of Tm: Cr: $YAlO_3$ laser at 2.35 μm," in *Dig. Tech. Papers, VIII Int. Quantum Electronics Conf.* (Montreal, P. Q., Canada), May 8-11, 1972.
[8] W. F. Krupke, "Optical absorption and fluorescence intensities in several rare-earth doped Y_2O_3 and LaF_3 single crystals," *Phys. Rev.*, vol. 145, pp. 325-337, May 1966.
[9] M. J. Weber, B. H. Matsinger, V. L. Donlan, and G. T. Surratt, "Optical transition probabilities for trivalent holmium in LaF_3 and $YAlO_3$," *J. Chem. Phys.*, vol. 57, pp. 562-567, July 1972.
[10] B. G. Wybourne, *Spectroscopic Properties of Rare Earths*. New York: Interscience, 1965.
[11] Y. K. Voronko, A. A. Kaminsky, V. L. Osiko, and A. M. Prokhorov, "Stimulated emission of Ho^{3+} in CaF_2 at 5512A," *Sov. Phys.-JETP Lett.*, vol. 1, pp. 3-5, Apr. 1965.
[12] L. F. Johnson and H. J. Guggenheim, "Infrared-pumped visible laser," *Appl. Phys. Lett.*, vol. 19, pp. 44-47, July 1971.
[13] ——, "Electronic- and phonon-terminated laser emission from Ho^{3+} in BaY_2F_8," *IEEE J. Quantum Electron.*, vol. QE-10, pp. 442-449, Apr. 1974.
[14] G. H. Dieke, *Spectra and Energy Levels of Rare Earth Ions in Crystals*. New York: Interscience, 1968.
[15] K. W. Martin and L. G. DeShazer, "Indices of refraction of the biaxial crystal $YAlO_3$," *Appl. Opt.*, vol. 12, pp. 941-943, May 1973.
[16] J. A. Caird, J. Nella, and L. G. DeShazer, unpublished.
[17] L. F. Johnson, private communication.
[18] L. M. Hobrock, "Spectra of thulium in yttrium orthoaluminate crystals and its four-level laser operation in the middle infrared," Ph.D. dissertation, Univ. Southern California, Los Angeles, Jan. 1972.
[19] J. Nella, private communication.

Continuous-wave operation of Nd:YVO₄ at 1.06 and 1.34 μ

A. W. Tucker, M. Birnbaum, and C. L. Fincher

Electronics Research Laboratory, The Aerospace Corporation, El Segundo, California 90245

L. G. DeShazer

Center for Laser Studies, University of Southern California, Los Angeles, California 90007
(Received 7 August 1975)

Continuous-wave plane-polarized outputs of 1 W at 1.06 μ and 0.35 W at 1.34 μ were obtained by end pumping small samples of Nd : YVO₄ with an argon-ion laser. Slope efficiencies and material losses were determined. At 1.06 and 1.34 μ, Nd:YVO₄ lasers can substantially outperform Nd:YAG lasers. Self-Q-switched operation of Nd:YVO₄ at both wavelengths was obtained by resonator misalignment.

Lasers of high efficiency and low thresholds are required in diverse applications such as communications, ranging, and metrology. The Nd : YAG laser has represented the state-of-the-art in most applications requiring low-threshold and efficient lasers. O'Connor[1] had observed almost ten years ago that Nd : YVO₄ possessed a larger stimulated-emission cross section at 1.06 μ than Nd : YAG and obtained low-threshold laser operation at 90 °K. Recently, detailed spectroscopic measurements quantified O'Connor's observations by showing that the stimulated-emission cross section of A-axis Nd : YVO₄ at 1.0634 μ was 4.6 times greater than that of Nd : YAG at 1.0642 μ.[2]

The superiority of Nd : YVO₄ lasers at 1.06 and 1.34 μ over Nd : YAG is demonstrated here by a comparison of the laser characteristics of small spectroscopic samples of Nd : YVO₄ with a high-optical-quality Nd : YAG laser rod. The comparisons were effected by end pumping with cw and pulsed argon-ion lasers at 514.5 nm, with emphasis on cw performance. Development of Nd : YVO₄ lasers is hindered by the lack of large (3×30 mm) laser-grade crystals. However, difficulties in vanadate crystal growth have been identified and large laser-grade crystals may soon be available.[3]

The equations describing the laser performance can be derived from consideration of the laser-threshold condition

$$R_1' R_2' \exp 2L(n_u\sigma - \Delta) = 1 \tag{1}$$

where R_1' and R_2' are the corrected mirror reflectivities (see explanation which follows), L is the length of the laser sample, n_u is the density of Nd³⁺ ions in the upper state of the laser transition, σ is the peak stimulated-emission cross section, Δ is the total losses per cm (exclusive of transmission losses by the mirrors) which include, for example, diffraction losses, excited-state absorption, and scattering losses. The rod ends were plane parallel and carefully aligned with the plane dielectric-coated end mirrors. In laser operation, the Fabry-Perot condition for maximum reflectivity $R' = (r^{1/2} + R^{1/2})^2 [1 + (rR)^{1/2}]^{-2}$ should be a good approximation with r the Fresnel reflectivity of the crystal and R the mirror reflectivity.[4]

In cw operation the upper-level population is related to the pump power according to

$$n_u = \frac{\eta f_B P_a \tau}{h\nu_p V}, \tag{2}$$

where n_u is the population per cm³ of the upper laser level, η is the quantum efficiency, namely, the fractional number of Nd³⁺ in the ⁴F₃/₂ level per absorbed photon, f_B is the fractional population in the upper laser sublevel of the ⁴F₃/₂ state, P_a is the pump power absorbed by the laser crystal, τ is the fluorescence lifetime of the ⁴F₃/₂ level, $h\nu_p$ is the energy per pump photon, and V is the volume pumped. Substitution of Eq. (2) into Eq. (1) yields

$$\frac{\eta f_B P_a \tau}{h\nu_p V} 2L\sigma = 2L\Delta - \ln R_1' R_2'. \tag{3}$$

The advantages of our method, namely, the accessibility of the quantities in Eq. (3) to direct measurement have been described earlier.[5] A critical evaluation of the measurement techniques will be treated in a subsequent publication.

One of the more difficult quantities to measure in a four-level laser system such as Nd : YVO₄ is the loss factor Δ. This can be determined by measurement of
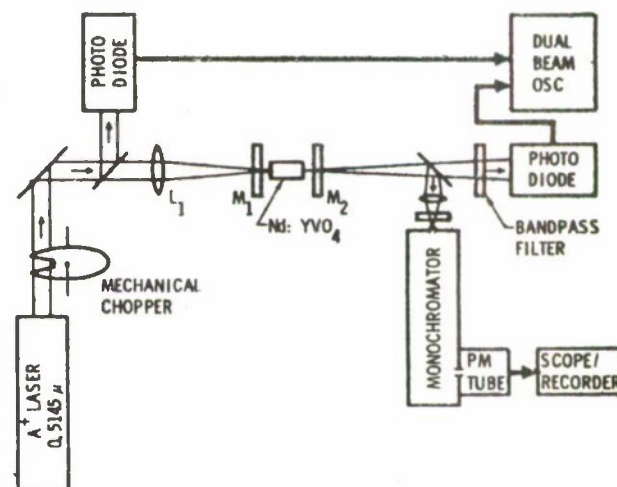

FIG. 1. Experimental arrangement.

TABLE I. Partial list of the parameters of Nd:YVO$_4$ (1%) and Nd:YAG (1%) crystals used in the paper. Entries above the broken line are taken from Ref. 2. The other values were obtained in this study.

	Nd:YVO$_4$ (A axis)	Nd:YAG
λ (μm)	1.0634	1.0643
τ (μs)	92	240
$\Delta\nu$ (cm^{-1})	7	6
σ (cm^{-2})	30×10^{-19}	6.5×10^{-19}
L (cm)	0.48	1.275
V (cm^3)	1.27×10^{-5}	3.86×10^{-5}
Δ (cm^{-1})	0.16	0.018

the laser threshold as a function of the reflectivity of the output mirrors.[5]

The experimental arrangement utilized for these measurements is shown in Fig. 1. By chopping the cw argon-ion laser beam, pump pulses of several millisecond duration were provided. Since this is long compared to the cavity and crystal response times, the results are directly applicable to cw performance of the lasers. Chopping reduces the heat load in the crystal and also prevents damage to the dielectric coatings on the mirrors. The Nd:YAG rod was antireflection coated at 1.06 μ, while the Nd:YVO$_4$ sample was uncoated. The resonator consisted of two plane-parallel mirrors; one a high (99%) reflector and the other a partial reflector of 99, 95.6, 84, 72.6, 67.6, and 53% reflectivity. A plot of the absorbed power vs $-\ln R_1' R_2'$ was accurately linear. The intercepts of the ordinate axis at $P_a = 0$ provided the loss coefficients, $\Delta = 0.16$ cm^{-1} for Nd:YVO$_4$ (1% concentration) and 0.018 cm^{-1} for Nd:YAG (1% concentration). The large losses for Nd:YVO$_4$ were attributed to scattering by the iridium platelets in the crystal which were introduced during the growth process.[3] A partial list of the parameters of Nd:YVO$_4$ (1%) and Nd:YAG (1%) crystals used in this paper is given in Table I.
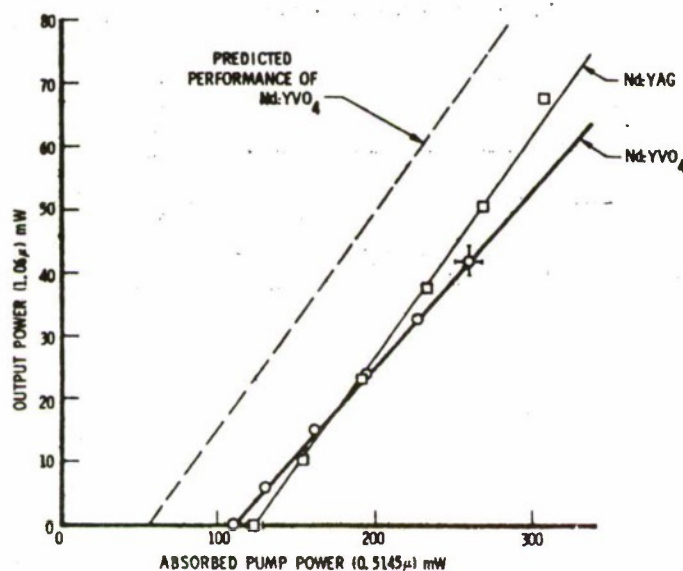
FIG. 2. Output power of Nd:YVO$_4$ (1%) and output power of Nd:YAG vs absorbed 0.5145-μ input power.
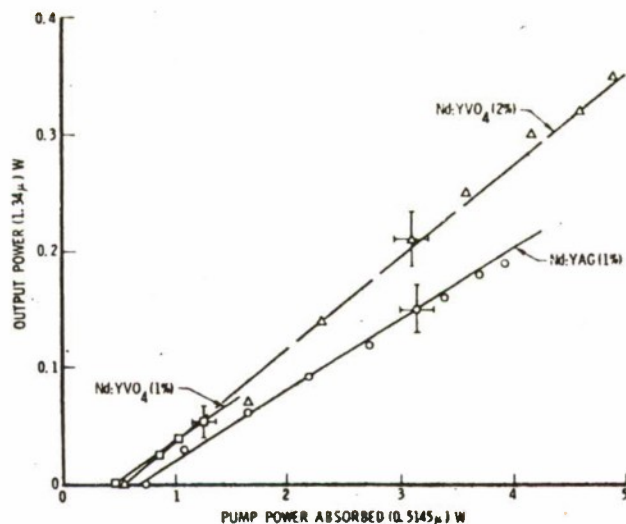
FIG. 3. Output power of Nd:YVO$_4$ (1%), Nd:YVO$_4$ (2%), and Nd:YAG (1%) vs absorbed 0.5145-μ input power.

Comparison of the laser performance of Nd:YVO$_4$ and Nd:YAG with optimum output mirrors of reflectivity of 67.6 and 84%, respectively, is shown in Fig. 2. The dashed line in Fig. 2 is obtained by assuming a loss coefficient for the Nd:YVO$_4$ sample (heavy solid line) equal to that of the Nd:YAG rod and is illustrative of the superior performance of Nd:YVO$_4$ to be expected with low-loss material. The slope efficiency of Nd:YVO$_4$ at 1.06 μ (Fig. 2) for optimum coupling was 20%. Some advantages of investigation of laser properties by laser end pumping are evident by the well-controlled performance and the exact linearity of the graphs of Figs. 2 and 3. When the laser is operated close to threshold, the output power of the laser is given by[6] $P = P_s[(W/W_{th}) - 1]$, where P is output power, P_s is a constant which depends upon the material parameters, W is the pump power absorbed, and W_{th} is the pump power absorbed at threshold. A difficulty was encountered in that optical feedback produced by reflection of pump light back into the argon-ion laser made optimum adjustment of the apparatus critical. A Faraday rotator is currently under construction which will isolate the argon-ion laser from the test laser and should circumvent this difficulty in future experiments.

There has been considerable interest in the development of eye-safe lasers, and this consideration prompted our investigation of the performance of Nd:YVO$_4$ at 1.34 μ. Continuous-wave operation of Nd:YVO$_4$ at 1.34 μ was readily achieved. A comparison of the cw operation of Nd:YVO$_4$ (1 and 2% samples) and Nd:YAG (1%) is shown in Fig. 3. The samples used in Fig. 3 were the same as in Fig. 1, except for the 2% Nd:YVO$_4$ sample.

The experimental arrangement was similar to that of Fig. 1, except that a 10 W argon-ion laser was used to provide pump power at 0.514 μ. The resonator consisted of a pair of plane-parallel mirrors both of 99% reflectivity at 1.34 μ which were specially designed for low reflectivity (less than 10%) at 1.06 μ, thereby suppressing oscillation at this wavelength. The superiority of the Nd:YVO$_4$ samples is evident despite their greater

losses. The slope efficiency of the 2% Nd : YVO$_4$ at 1.34 μ was 7%.

Work is in progress to determine the loss coefficient at 1.34 μ and to measure the stimulated-emission cross sections of Nd : YVO$_4$ and Nd : YAG at 1.34 μ. A preliminary estimate of the stimulated-emission cross section of Nd : YVO$_4$ (1%) at 1.34 μ (assuming a Δ of 0.16 cm^{-1}) and using the data of Fig. 3, shows that it is considerably larger than that of Nd:YAG.

In adjustment of the mirrors of the Nd : YVO$_4$ lasers, in the quasi-cw mode of operation at 1.06 μ, pulsed outputs, in several instances, were observed. The YVO$_4$ sample was misaligned with respect to the resonator axis by about 25 arc min and self-giant pulsing at 1.06 μ was readily obtained. Pulsewidths of 40 ns were observed with peak powers over 1000 times greater than the cw output of the laser. Self-giant pulsing was ob-

served at 1.34 μ, but only preliminary observations were obtained. Self-Q-switched operation of Nd : YAG could not be achieved under the same conditions, but had been observed earlier by cooling the Nd:YAG.[7] The ease of self-Q-switching the Nd:YVO$_4$ evidently stems from the higher stimulated-emission cross sections.

[1]J.R. O'Connor, Appl. Phys. Lett. 9, 407 (1966).
[2]M. Bass, L.G. DeShazer, and U. Ranon, Report No. ECOM-74-0104-1, 1974 (unpublished).
[3]A.M. Chase (private communication).
[4]D. Findlay and R.A. Clay, Phys. Lett. 20, 277 (1966).
[5]M. Birnbaum and J.A. Gelbwachs, J. Appl. Phys. 43, 2335 (1972).
[6]G. Birnbaum, Optical Masers (Academic, New York, 1964), p. 90.
[7]M. Birnbaum and C.L. Fincher, Proc. IEEE 57, 804 (1969).

101	Defense Documentation Center	
	ATTN: DDC-TCA	
	Cameron Station (Bldg 5)	
012	Alexandria, VA 22314	

101 Defense Documentation Center
ATTN: DDC-TCA
Cameron Station (Bldg 5)
012 Alexandria, VA 22314

107 Director
National Security Agency
ATTN: TDL
001 Fort George G. Meade, MD 20755

108 Director, Defense Nuclear Agency
ATTN: Technical Library
001 Washington, DC 20305

200 Office of Naval Research
Code 427
001 Arlington, VA 22217

201 Cdr, Naval Ship Systems Command
Technical Library, Rm 3 S-08
National Center No. 3
001 Washington, DC 20360

205 Director
Naval Research Laboratory
ATTN: Code 2627
001 Washington, DC 20375

206 Commander
Naval Electronics Lab Center
ATTN: Library
001 San Diego, CA 92152

207 Commander
US Naval Ordnance Laboratory
ATTN: Technical Library
White Oak, Silver Spring
001 MD 20910

210 Commandant, Marine Corps
HQ, US Marine Corps
ATTN: Code LMC
001 Washington, DC 20380

211 HQ, US Marine Crops
ATTN: Code INTS
001 Washington, DC 20380

212 Cmd, Control & Communications
Div Development Center
Marine Corps Dev & Educ Cmd
001 Quantico, VA 22134

215 Naval Telecommunications Command
Tech Library, Code 422
4401 Massachusetts Avenue, NW
001 Washington, DC 20390

220 Naval Research Laboratory
Code 6503, LTPO
001 Washington, DC 20390

301 Rome Air Development Center
ATTN: Documents Library (TILD)
001 Griffiss AFB, NY 13441

307 HQ ESD(XRRI)
L. G. Hanscom Field
001 Bedford, MA 01730

312 AFSPCOMMCEN/SUR
001 San Antonio, TX 78243

313 Armament Development & Test Ctr.
ATTN: DLOSL, Tech Library
001 Eglin Air Force Base, FL 32542

314 HQ, Air Force Systems Command
ATTN: DLCA
Andrews Air Force Base
001 Washington, DC 20331

320 Air Force Systems Command
Advanced Systems Div (ASD/ENAD)
001 Wright-Patterson AFB, OH 45433

401 Commander
HQ, TRADOC
ATTN: ATTNG-XO
001 Ft Monroe, VA 23651

403 HQDA (DACE-CMS)
001 Washington, DC 20310

405 OSASS -RD
001 Washington, DC 20310

406 Commander
US Army Training & Doctrine Cmd
ATTN: ATCD-SI
001 Fort Monroe, VA 23651

407 001	Commander US Army Training & Doctrine Cmd ATTN: ATCD-CI Fort Monroe, VA 23651
408 001	HQDA(DARD-ARS-P/ Dr. R.B. Watson) Washington, DC 20310
409 001	Cdr, US Army Materiel Command ATTN: AMCMA-EE 5001 Eisenhower Ave Alexandria, VA 22333
410 001	Cdr, US Army Materiel Command ATTN: AMCRD-TP (Dr. B. Zarwyn) 5001 Eisenhower Ave Alexandria, VA 22333
411 001	Cdr, US Army Materiel Command ATTN: AMCRD-W 5001 Eisenhower Ave Alexandria, VA 22333
413 001	Cdr, US Army Materiel Command ATTN: AMCRD-FW 5001 Eisenhower Ave Alexandria, VA 22333
416 004	Commander US Army R&D Group (Far East) APO, San Francisco 96343
419 001	Commander US Army Missile Command ATTN: AMSMI-RRA, Bldg 7770 Redstone Arsenal, AL 35809
420 001	Commander US Army Missile Command ATTN: AMSMI-RR (Mr. W.B. Jennings) Redstone Arsenal, AL 35809
421 002	Cdr, US Army Missile Command Redstone Scientific Info Center ATTN: Chief, Document Section Redstone Arsenal, AL 35809
423 001	Commander US Army Armament Command ATTN: AMSAR-RDP (Library) Rock Island, IL 61201

422 	Commander US Army Aeromedical Research Lab ATTN: Library Fort Rucker, AL 36362
424 001	Commander Rock Island Arsenal ATTN: SARRI-LP-L-Tech Library Rock Island, IL 61201
425 001	Commander, Rock Island Arsenal US Army Armament Command ATTN: SWERI-RET-E (Dr. L. Gardner) Rock Island Arsenal, IL 61201
427 003	Cdr, US Army Combined Arms Combat Developments Activity ATTN: ATCAIC-IE Fort Leavenworth, KS 66027
429 001	Commander US Army Logistics Center ATTN: ATCL-MA Fort Lee, VA 23801
431 001	Commander US Army Intelligence School ATTN: ATSIT-CTD Fort Huachuca, AZ 85613
433 001	Cdr, US Army Aviation Systems Cmd ATTN: AMSAV-G PO Box 209 St. Louis, MO 63166
434 001	Commander US Army Test & Evaluation Command ATTN: AMSTE-D5-E (Mr. J. Bialo) Aberdeen Proving Ground, MD 21005
436 001	Commandant US Army Engineer School ATTN: ATSE-CDT-DT-TL Fort Belvoir, VA 22060
441 001	Commander Harry Diamond Laboratories ATTN: AMXDO-RCB, Mr. F. Harris Washington, DC 20438

442 Commander Harry Diamond Laboratories ATTN: Library 2800 Powder Mill Road 001 Adelphi, MD 20783	484 Cdr, US Army Research Ofc ATTN: AMXRO-PH (Dr. R.J. Lontz) PO Box 12211 001 Research Triangle Park, NC 27709
447 Cdr, US Army Picatinny Arsenal ATTN: SMUPA-VC5 Bldg 350 001 Dover, NJ 07801	485 Cdr, HQ MASSTER Technical Information Center ATTN: Mrs. Ruth Reynolds 001 Fort Hood, TX 76544
449 Commander Picatinny Arsenal ATTN: SARPA-TS-S #59 002 Dover, NJ 07801	486 Commander US Army Mobility Eqpt R&D Cen ATTN: SMEFB-R 001 Fort Belvoir, VA 22060
451 Commander Frankford Arsenal ATTN: Dr. Wm McNeill, PDS 64-4 001 Philadelphia, PA 19137	488 US Army Security Agency ATTN: IARD Arlington Hall Station 001 Arlington, VA 22212
454 Cdr, US Army Training Device Agcy ATTN: AMXPG Naval Training Equipment Center 001 Orlando, FL 32813	489 Commander US Army Tank-Automotive Command ATTN: AMSTA-RW-L 001 Warren, MI 48090
456 Commander White Sands Missile Range ATTN: STEWS-RE-IO 001 White Sands Missile Range, NM 88002	492 Commandant US Army Air Defense School ATTN: C&S Dept, Msl Sci Div 001 Fort Bliss, TX 79916
458 Dir/Dev & Engr Defense Systems Div ATTN: SAREA-DE-DDR, H. Tannenbaum 002 Edgewood Arsenal, APG, MD 21010	496 Cdr, US Army Combined Arms Combat Developments Activity ATTN: ATCACC 001 Fort Leavenworth, KS 66027
465 Commander Aberdeen Proving Ground ATTN: STEAP-TL (Bldg 305) 002 Aberdeen Proving Ground, MD 21005	500 Commander US Army Yuma Proving Ground ATTN: STEYP-MTD (Tech Library) 002 Yuma, AZ 85364
480 Commander USASA Test & Evaluation Center 001 Fort Huachuca, AZ 85613	501 Commander US Army Arctic Test Center ATTN: STEAC-PL 002 APO, Seattle 98733
483 Cdr, US Army Research Ofc ATTN: AMXRO-IP PO Box 12211 001 Research Triangle Park, NC 27709	502 CO, US Army Tropic Test Center ATTN: STETC-MO-A (Tech Library) Drawer 942 001 Fort Clayton, Canal Zone 09827

511   Commander
        US Army Nuclear Agency
001   Fort Bliss, TX 79916

512   Directorate of Combat Dev
        US Army Armor School
        ATTN: ATSB-CD-AA
001   Fort Knox, KY 40121

514   Commandant
        US Army Inst for Military
        Assistance
        ATTN: ATSU-CTD-OMS
001   Fort Bragg, NC 28307

517   Commander
        US Army Missile Command
        ATTN: AMSMI-RE (Mr. Pittman)
001   Redstone Arsenal, AL 35809

518   Commander
        Harry Diamond Laboratories
        ATTN: AMXDO-RCB
              (Dr. J. Nemarich)
001   Washington, DC 20438

519   Commander
        US Army Systems Analysis Agency
        ATTN: AMXSY-T (Mr. A. Reid)
001   Aberdeen Proving Ground, MD
        21005

520   Cdr, Frankford Arsenal
        ATTN: SMUFA-N-4100
        Bldg 201
001   Philadelphia, PA 19137

596   Commandant
        US Army Signal School
        ATTN: ATSN-CTD-MS
002   Fort Gordon, GA 30905

603   ECOM Liaison Office
        US Army Electronic Proving Ground
001   Fort Huachuca, AZ 85613

610   Director, Night Vision Laboratory
        US Army Electronics Command
        ATTN: AMSEL-NV-D
001   Fort Belvoir, VA 22060

607   Commander
        US Army Tank-Automotive Cmd
        ATTN: AMSTA-RHP, Dr. J. Parks
001   Warren, MI 48090

608   Director
        Night Vision Laboratory (ECOM)
        ATTN: AMSEL-NV-VIS
              (Mr. L. Gillespie)
001   Fort Belvoir, VA 22060

609   Director
        Night Vision Laboratory (ECOM)
        ATTN: AMSEL-NV-SD (Mr. Gibson)
001   Fort Belvoir, VA 22060

614   Chief
        Ofc of Missile Electronic Warfare
        Electronic Warfare Lab, ECOM
001   White Sands Missile Range
        NM 88002

617   Chief
        Intel Materiel Dev & Support Ofc
        Electronic Warfare Lab, ECOM
001   Fort Meade, MD 20755

680   Commander
        US Army Electronics Command
000   Fort Monmouth, NJ 07703

        1 AMSEL-PP-I-PI
        1 AMSEL-PL-ST
        1 AMSEL-NL-D
        1 AMSEL-WL-D
        1 AMSEL-VL-D
        1 AMSEL-BL-D
        1 AMSEL-CT-L (Dr. R. Buser)
        1 AMSEL-CT-LC (Dr. E. Tebo)
        1 AMSEL-CT-L (Mr. B. Louis)
        1 AMSEL-CT-LD (Dr. E. Schiel)
        1 AMSEL-CT-LE
           (Dr. H. Hieslmair)
        4 AMSEL-CT-LD (Mr. J. Strozyk)
        1 AMSEL-TL-D
        1 AMSEL-TL-I (Dr. H. Jacobs)
        1 AMSEL-TL-B (Mr. M. Zinn)
        1 AMSEL-TL-TG
           (Mr. S. Schneider)
        1 AMSEL-NL-R-5
           (Dr. E. Dworkin)

(4)

```
  1 AMSEL-VL-E                        718  TACTEC
  1 AMSEL-WL-N                             Battelle Memorial Institute
  1 AMSEL-CT-L-D (Ofc of Record)           505 King Avenue
  1 AMSEL-MA-MP                       001  Columbus, OH  43201
  2 AMSEL-MS-TI
  1 AMSEL-GG-TD                       720  Thermophysical Properties
  2 AMSEL-PA                                  Res Center
  1 AMCPM-TDS-SE                           Purdue University,
  1 USMC-LNO                               Research Park
  1 AMSEL-RD                               2595 Yeager Road
  1 TRADOC-LNO                        001  Lafayette, IN  47906
  1 AMSEL-CG (Mr. Doxey)
 25 Originating Office               001  Airtron Division,
                                           Litton Industries
701  MIT-Lincoln Laboratory                Dr. R. Belt
     ATTN: Library - Rm A-082              200 East Hanover Ave.
     PO Box 73                             Morris Plains, NJ  07950
001  Lexington, MA  02173

703  NASA Scientific & Technical
        Information Facility
     ATTN: Acquisitions Br (S-AK/DL)
     PO Box 33
     College Park, MD  20740

705  Advisory Group on Electronic Devices
     201 Varick Street, 9th Floor
002  New York, NY  10014

706  Advisory Group on Electronic Devices
     ATTN: Secy, Working Group D
        (Lasers)
     201 Varick Street
002  New York, NY  10014

707  Target Signature Analysis Center
     Env. Research Inst of Michigan
     PO Box 618
001  Ann Arbor, MI 48107

708  Ballistic Missile Radiation Anal Cen
     Env. Research Inst of Michigan
     Box 618
001  Ann Arbor, MI 48107

711  Metals and Ceramics Inf Center
     Battelle
     505 King Avenue
001  Columbus, OH  43201
```